Physics and current understanding of X-ray storage phosphors

DER UNIVERSITÄT-GESAMTHOCHSCHULE PADERBORN
ZUR ERLANGUNG DER LEHRBERECHTIGUNG
(VENIA LEGENDI)
FÜR DAS FACH
EXPERIMENTALPHYSIK
vorgelegte Habilitationsschrift

von

STEFAN SCHWEIZER

MAI 2000 (Eröffnung des Habilitationsverfahrens)
NOVEMBER 2000 (Habilitationsvortrag)
DEZEMBER 2000 (Abschluss des Habilitationsverfahrens)

Table of Contents

Introduction

In the beginning of radiation diagnostics, conventional photographic films were used for X-ray imaging. Due to their poor sensitivity to X-rays, high doses had to be used for the imaging process in medical radiography. Significant progress was achieved by the use of a combination of intensifying screens coated with a scintillator layer and a photographic film. The scintillator screen plays the role of an X-ray to optics converter (X-ray luminescence), and the film is as before the image storing part of the system. The latent X-ray image becomes visible after appropriate chemical processing of the film.

In contrast to the X-ray scintillators, where the X-ray energy is directly converted into visible light, X-ray storage phosphors store the radiation image in proportion to its intensity distribution in a storage phosphor screen. The screen is coated with X-ray storage phosphor crystallites which are imbedded in an organic binder. Upon X-irradiation, complementary defects (electron and hole trap centres) are generated in these crystallites. The electron of the electron trap centre can be stimulated afterwards and it recombines with the complementary hole trap centre. The recombination energy is often transferred to a doped activator which emits light of a characteristic photon energy. This process is called photostimulated luminescence (PSL).

Since the sensitivity of the X-ray storage phosphors exceeds that of the scintillator-film-system by at least one order of magnitude, the applied X-ray dose can be reduced significantly. For the best X-ray storage phosphors the dose dependence shows linearity for more than five orders of magnitude. Under- and over-exposures caused by the S-shaped sensitivity characteristics of all the photographic films including the scintillator-film-system can thus be avoided. The image is digitised directly and can be archived easily. Due to the scattering effects of the stimulation light during the read-out process, the spatial resolution of X-ray storage phosphor screens is still inferior compared to that of scintillator-film-systems.

For practical use in commercial X-ray imaging systems the requirements for X-ray storage phosphors are somewhat different from those for scintillator-film based systems. Besides a high X-ray absorption, which can be achieved by the incorporation of elements with high mass number, the generated complementary defects should be thermally stable at room temperature, to make sure that the image information is stored until it is read out, possibly several hours later. The wavelength of the stimulation light should be in a spectral range which is clearly separated from the spectral range of the emitted light of the activator. Moreover, it would be advantageous if the stimulation light was in a spectral range where low-cost lasers are available as light sources. The emission of the activator should be in a spectral range where it can be detected easily and sensitively. The radiative life time of the activator as well as the bleaching time of the defects determine the time necessary for the read-out process. The re-usability of such X-ray storage phosphor screens is an important advantage. It should thus be possible to erase all defects in the crystallites after the read-out process has been accomplished.

The so far best-known X-ray storage phosphor is BaFBr doped with Eu^{2+} as activator [1]. In spite of many efforts to understand the information storage and read-out processes, no complete understanding has yet been achieved (see e.g., [2, 3, 4, 5]). The lower spatial resolution of commercially-used X-ray imaging systems based on BaFBr is partially due to the matlockite structure of the crystallites in the storage phosphor layer. During the read-out process the stimulation light is not only scattered due to the different refractive indices of the organic binder and the phosphor crystallites, but also due to the statistical distribution of the birefringent crystallites in the screen. Optically isotropic crystals such as e.g. cubic alkali halides would possibly minimise the scattering effects in the storage phosphor layer. It is thus a challenge to find optically isotropic storage phosphor materials which have the same performance as BaFBr:Eu^{2+}.

One of the suitable cubic alkali halides is KBr:In^{+}, which was shown to have storage and PSL properties [6]. From the practical point of view it will not be a very important system due to its low X-ray stopping power. RbI:Tl^{+} has, in principle, very good storage and PSL properties [7]. However, the stored image fades away at room temperature within minutes, so that a very fast read-out process has to be initiated immediately after taking the image. It has been shown that the alkali halides RbBr:Ga^{+} and CsBr:Ga^{+} have excellent figures of merit as X-ray storage phosphors [8]. They are optically isotropic and therefore very promising. The elpasolite Cs_2NaYF_6:Ce^{3+} is also comparable to BaFBr:Eu^{2+} with respect to X-ray conversion and necessary stimulation energy [9].

The observation that upon X-irradiation the electron and hole trap centres are always created with a spatial correlation to the activator is of particular interest for the functioning of the storage phosphors. It is statistically not very probable that for low medical doses the photostimulated electron of the electron trap centre and a hole of the hole trap centre recombine near an activator. A phosphor does not function, unless electron and hole trap centres are generated near the activator. The reason for this spatial correlation of the radiation damage centres with the activator is so far not understood and represents a very interesting, fundamental open question.

In chapter 1 the experimental fundamentals of the measurement techniques used are described. Chapter 2 deals with the characterisation of X-ray storage phosphors such as performance and spatial resolution, as well as the experimental setup for the read-out process.

In chapter 3 one finds a detailed description of the information storage and read-out process in the X-ray storage phosphor BaFBr:Eu^{2+} emphasising the generation mechanism and structure of electron and hole trap centres, whilst alternative systems such as alkali halides and elpasolites, and glasses or glass ceramics are described in chapter 4 and 5, respectively.

Chapter 1

Experimental fundamentals

The main experimental method used to analyse the nature of the generated electron and hole trap centres, which are the basis of the information storage and read-out processes, is electron paramagnetic resonance (EPR), because electron and hole trap centres are paramagnetic before they recombine in the photostimulated luminescence process. For detailed defect investigations, electron nuclear double resonance (ENDOR) is also needed. However, because of low defect concentration conventional EPR and ENDOR are often not sensitive enough. Therefore, optically detected EPR and ENDOR techniques have to be applied. Their basis is the detection of changes of the magnetic circular dichroism of the optical absorption (MCDA) induced by EPR/ENDOR transitions. In the following only a brief description can be given of the most important methods. For further details the reader is referred to e.g. [10].

1.1 Magneto-optical measurement techniques

1.1.1 Magnetic circular dichroism of the optical absorption

The magnetic circular dichroism of the optical absorption (MCDA) is the difference between the absorption of right and left circularly polarised light. The light is propagated parallel to an external magnetic field **B** in which the sample is situated. The MCDA is defined by

$$\varepsilon = \frac{\omega d}{2c}(k_{\mathrm{r}} - k_{\mathrm{l}}) \tag{1.1}$$

where k_r and k_l are the absorption indices for right and left circularly polarised light, d the thickness of the crystal, ω the angular frequency of the light and c the speed of light. The measured quantities are the energy dependent absorption coefficients $\alpha(E)$. With

$$k(E) = \frac{\hbar c}{2E}\alpha(E) \tag{1.2}$$

and $E = \hbar\omega$ equation (1.1) becomes

$$\varepsilon = \frac{d}{4}(\alpha_r - \alpha_l). \tag{1.3}$$

Assuming an exponential decay of the light intensity within the crystal, according to Lambert-Beer's law the measured light intensity is

$$I_{r,l} = I_o \exp(-\alpha_{r,l}\, d), \tag{1.4}$$

where I_o is the intensity of the incident light and thus the sum of the incident right and left circularly polarised light. Transformation of equation (1.4) leads to

$$\alpha_{r,l} = \frac{1}{d}\ln\frac{I_o}{I_{r,l}}. \tag{1.5}$$

Insertion of this result into equation (1.3) one obtains

$$\varepsilon = \frac{1}{4}\ln\frac{I_r}{I_l}. \tag{1.6}$$

With the average intensity $I_a = (I_r + I_l)/2$ and the intensity difference $\Delta I = I_r - I_l$ equation (1.6) becomes

$$\varepsilon = \frac{1}{4}\ln\frac{1+\frac{\Delta I}{2I_a}}{1-\frac{\Delta I}{2I_a}}. \tag{1.7}$$

Assuming $\Delta I << I_a$, i.e. $d(\alpha_r - \alpha_l) << 1$, equation (1.7) simplifies to

$$\varepsilon \approx \frac{\Delta I}{4I_a} = \frac{I_r - I_l}{2(I_r + I_l)}. \tag{1.8}$$

The MCDA consists of a paramagnetic and a diamagnetic part.

$$\varepsilon(B,T) = \varepsilon_{dia}(B) + \varepsilon_{para}(B,T) \tag{1.9}$$

The paramagnetic part is both temperature and magnetic field dependent. The diamagnetic part, which is caused by non-resolved Zeeman splittings of the excited states [11], is temperature independent, but also proportional to the external magnetic field value B.

For $S = 1/2$ systems the paramagnetic MCDA is proportional to the polarisation P of the ground state. The polarisation P can be calculated using the Langevin function

$$\varepsilon_{\text{para}} \propto P = \frac{n_- - n_+}{n_- + n_+} = \tanh \frac{g\mu_B B}{2kT}. \tag{1.10}$$

n_+ and n_- are the occupation numbers of the $m_S = \pm 1/2$ states, g is the Landé g-factor, μ_B the Bohr magneton, B the magnetic field value and T the temperature. For $S > 1/2$ systems the polarisation P is given by the Brillouin function (see e.g., [10]).

Figure 1.1 schematically represents the circularly polarised transitions for an alkali atom model, which is often used to describe the MCDA of an F centre (electron trapped in an anion vacancy) in alkali halides [12]. The excited state is split by the spin-orbit interaction into a $J = 1/2$ and a $J = 3/2$ state. The degeneracy is lifted by the applied magnetic field **B**. Neglecting the Zeeman splittings of the excited states one absorption band is observed for right and one for left circularly polarised light. The intensity is equal for both bands. Both absorption bands, the separation of which is determined by the spin-orbit interaction, are identical in their respective shapes which are taken to be Gaussians in this model. Phonon-broadening of the transitions is taken into account via the "rigid shift" approximation [13]. For the selection rule $m_J = \pm 1$ and a small spin-orbit interaction compared to the half-width of the right and left circular absorption bands this leads to a derivative-like structure of the resulting MCDA (see e.g., [10]).

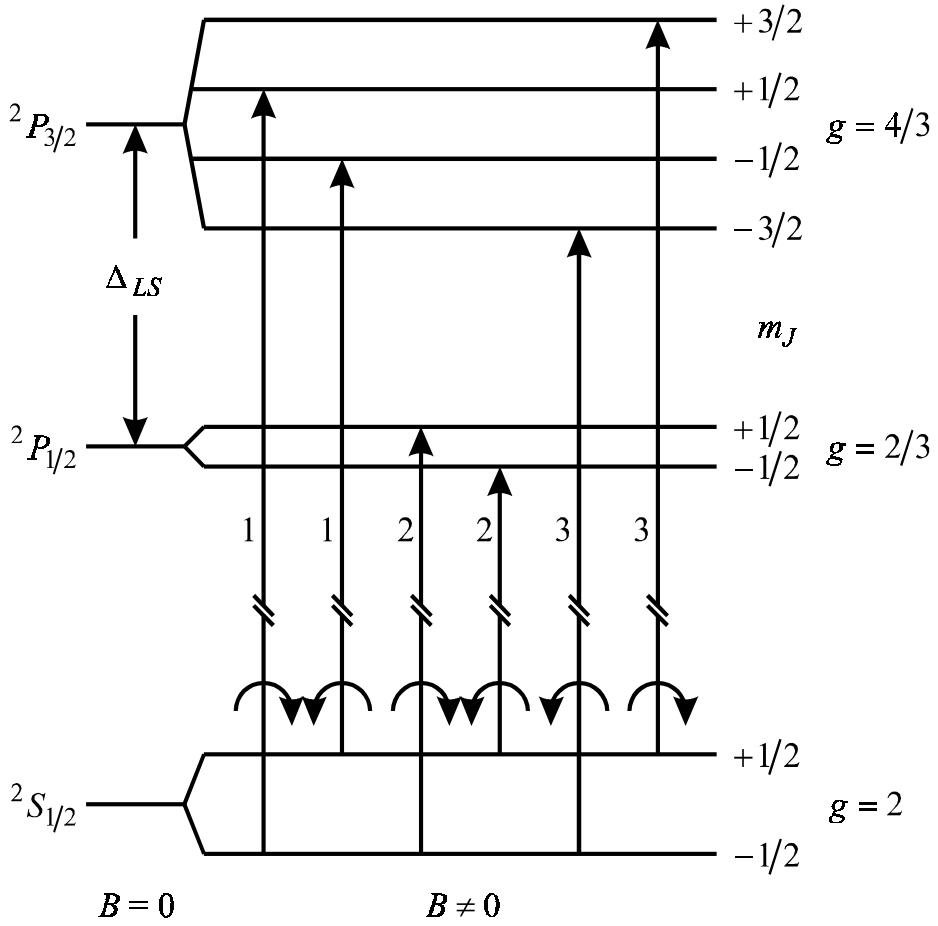

Figure 1.1 Schematic diagram of the energy levels in the alkali atom model to explain the MCDA of an F centre [12]. The $\Delta m_J = +1$ transitions absorb right, and the $\Delta m_J = -1$ transitions, left circularly polarised light. The energy difference between the *S* and the *P* states amounts to several eV, the spin-orbit splitting Δ_{LS} to several meV up to 1 eV depending on the nature of the anions. The numbers on the transition arrows indicate the relative transition probabilities.

1.1.2 Optical detection of electron paramagnetic resonance (EPR) and electron nuclear double resonance (ENDOR)

As described above the paramagnetic part of the MCDA is proportional to the spin polarisation of the ground state. Perturbing the thermal equilibrium occupation of the Zeeman levels at a fixed optical wavelength by applying a resonant and partly saturating electron paramagnetic resonance (EPR) transition, the spin polarisation is changed and,

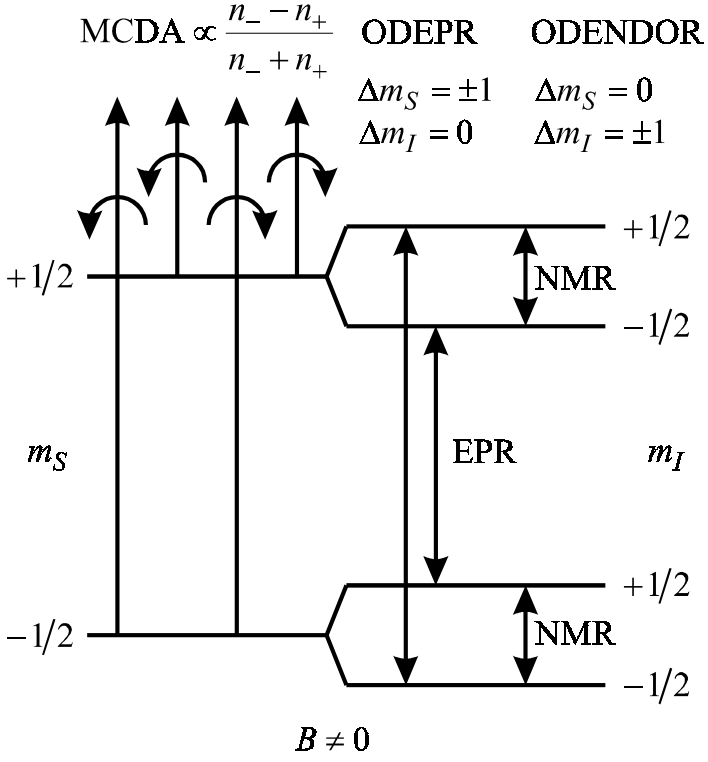

Figure 1.2 Schematic diagram of the energy levels of a paramagnetic centre having $S = 1/2$ and $I = 1/2$ to explain optically detected EPR and ENDOR.

according to equation (1.10), the paramagnetic MCDA decreases (figure 1.2). In an optically detected EPR experiment the changes of the detected MCDA are measured. A fixed optical wavelength and a fixed saturating microwave field are used and the external magnetic field is swept through the resonance conditions. EPR lines due to defects are then observed as changes in the magnetic field dependent MCDA signal (MCDA-detected EPR) at this optical wavelength. This technique, the optical detection of EPR, can increase the sensitivity considerably depending though on the optical transition probability (oscillator strength) and the spin-orbit splitting of the excited states. Moreover, the coupling of MCDA and EPR allows the assignment of optical transitions to paramagnetic defects. In particular, it is possible to separate superimposed MCDA bands, which are due to different defects, by their distinct MCDA-detected EPR spectra. When recording the wavelength-dependent ODEPR effect under resonant conditions, the MCDA "excitation" spectrum of a defect is obtained. This procedure is known as "tagged" MCDA (see e.g., [10]).

In addition to the EPR transitions the ground state spin polarisation can be affected by applying simultaneously a resonant radio frequency (rf) field to induce NMR transitions. The NMR transitions between hyperfine (hf) or superhyperfine (shf) Zeeman levels also change the spin polarisation. Therefore also electron nuclear double resonance (ENDOR) can be detected optically via the change of the MCDA. Information about the defect structure can be obtained from the measured hf and shf interaction (see e.g., [10]).

1.1.3 Cross-relaxation spectroscopy

For the functioning of the storage phosphors it is necessary that the X-ray induced electron and hole trap centres are generated not too far from another and they are also spatially correlated to the activators. To investigate this experimentally one can use cross-relaxation spectroscopy. The cross-relaxation probability between two spin systems assuming a dipole-dipole interaction is given by [14]

$$R_{ij} = \hbar^{-2} \left| \mathcal{H}_{ij} \right|^2 g_{\alpha\beta}$$

with $$\left| \mathcal{H}_{ij} \right|^2 = g_i^2 g_j^2 \beta^4 (3 - \cos^2 \vartheta_{ij})^2 \Big/ r_{ij}^6 \tag{1.11}$$

and $$g_{\alpha\beta} = \int g_\alpha(\nu') g_\beta(\nu'') \delta(\nu' - \nu'') \, \mathrm{d}\nu' \mathrm{d}\nu'' ,$$

where $g_{\alpha\beta}$ is the overlap integral of the shape function of the EPR lines of both defects types, α and β, which can be determined experimentally from the EPR spectra. The indices i and j characterise the individual defect of each type taking part in the cross-relaxation (CR), with a separation r_{ij} between defects i and j and an angle ϑ_{ij} between the ij connecting line and the magnetic field. β is the gyromagnetic ratio in the CGS system and g_i and g_j are the electronic g factors.

According to equation (1.11) the cross-relaxation probability depends significantly on the separation between the two interacting spin-systems. Thus, it is possible to determine the distribution of the separations between different paramagnetic defects, however, only in case of diluted spin-systems. The dynamical behaviour of the spin polarisation of a paramagnetic defect can then be calculated by a set of rate equations describing the occupations of the Zeeman levels. The occupations are influenced by EPR transitions and spin-lattice relaxations. If two spin systems are coupled by CR, addi-

tional terms due to CR enter the rate equations, which become non-linear. For a high concentration of paramagnetic defects the cross-relaxation effects are mainly determined by the average distance between the interacting spin-systems. In this case one does not obtain any further information about the distribution of separations of the different spin-systems. For details see e.g., [15].

1.2 Conventional EPR and ENDOR

In contrast to optically detected EPR, the EPR transitions in conventional experiments are detected via microwave absorption. In ENDOR the detection of NMR transitions is achieved via the change of the partly saturated EPR effect. To observe an ENDOR effect, the EPR transition has to be saturated partly by applying sufficiently high microwave power. The rf-induced NMR transition leads to a partial desaturation of the EPR, which is compensated by an increased microwave absorption (figure 1.3). The latter is detected (see e.g., [10]). In stationary ENDOR experiments [16] one can make use of a cross-relaxation probability T_{x}^{-1}, which allows the stationary observation of the rf-induced desaturation of the EPR transition.

1.3 Analysis of EPR and ENDOR spectra

1.3.1 The spin Hamiltonian

For the analysis of EPR and ENDOR spectra an appropriate spin Hamiltonian is used (see e.g., [10]), which allows the calculation of the energy levels of the spin system. The spin Hamiltonian operator $\mathcal{H}$ is the sum of several operators: The electron Zeeman operator $\mathcal{H}_{\mathrm{EZ}}$, the fine-structure operator $\mathcal{H}_{\mathrm{FS}}$, the hyperfine structure operator $\mathcal{H}_{\mathrm{HF}}$, the superhyperfine structure operator $\mathcal{H}_{\mathrm{SHF}}$, the nuclear Zeeman operator $\mathcal{H}_{\mathrm{NZ}}$, and the nuclear quadrupole operator $\mathcal{H}_{\mathrm{Q}}$.

$$\mathcal{H} = \underbrace{\mu_{\mathrm{B}}\,\mathbf{S}\cdot\mathbf{g}\cdot\mathbf{B}}_{\mathcal{H}_{\mathrm{EZ}}} + \underbrace{\sum_{k=2}^{2S}\sum_{q=-k}^{k} b_k^q O_k^q(\mathbf{S})}_{\mathcal{H}_{\mathrm{FS}}} + \underbrace{\sum_i \left\{\mathbf{I}_i\cdot\mathbf{A}_i\cdot\mathbf{S}_i}_{\mathcal{H}_{\mathrm{HF/SHF}}} \underbrace{- \mu_{\mathrm{n}}\,\mathbf{I}_i\cdot\mathbf{g}_{\mathrm{n},i}\cdot\mathbf{B}}_{\mathcal{H}_{\mathrm{NZ}}} + \underbrace{\mathbf{I}_i\cdot\mathbf{Q}_i\cdot\mathbf{I}_i}_{\mathcal{H}_{\mathrm{Q}}}\right\} \tag{1.12}$$

with $\mathbf{B}$ magnetic field vector,

μ_{B} Bohr magneton,

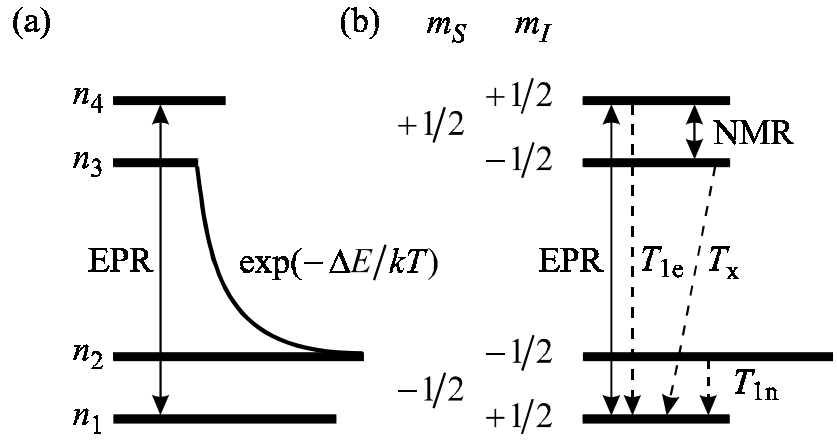

Figure 1.3 Schematic diagram explaining the EPR and ENDOR effect of a simple system having $S = 1/2$ and $I = 1/2$. The relative occupation of levels 1-4 is marked by their lengths considering a non-saturated EPR transition (figure 1.3a) and the stationary occupation for saturated EPR and NMR transitions, including possible relaxation mechanisms (figure 1.3b).

μ_n nuclear magneton,

$\mathbf{S}$ electron spin operator,

$\mathbf{I}_i$ nuclear spin operator of nucleus i,

$\mathbf{g}$ electron g tensor,

$\mathbf{g}_{n,i}$ nuclear g tensor of nucleus i,

b_k^q Stevens parameter,

O_k^q Stevens operator,

$\mathbf{A}_i$ hyperfine or superhyperfine structure tensor of nucleus i,

$\mathbf{Q}_i$ quadrupole tensor of nucleus i.

The electron Zeeman term $\mathcal{H}_{EZ}$ describes the magnetic interaction between the electron spin $\mathbf{S}$ and the external magnetic field $\mathbf{B}$, the nuclear Zeeman term $\mathcal{H}_{NZ}$ the interaction between the nuclear spin $\mathbf{I}$ and the magnetic field $\mathbf{B}$. The fine-structure term $\mathcal{H}_{FS}$ is a sum of Stevens operators [17] and describes the spin-spin interaction within a spin system having $S > 1/2$. Due to time reversal symmetry the sum indices q are even numbers. The use of Stevens operators in the fine-structure term has the advantage that they obey certain symmetry restrictions, i.e. some of the Stevens parameters vanish for certain point group symmetries. For $S \leq 3/2$ the fine-structure expression can be reduced to $\mathbf{S} \cdot \mathbf{D} \cdot \mathbf{S}$. The interaction between the electron spin $\mathbf{S}$ and the nuclear spin $\mathbf{I}$ of the

central nucleus or a neighbour nucleus is described by the hyperfine (hf) or superhyperfine (shf) structure term $\mathcal{H}_{\mathrm{HF/SHF}}$. The quadrupole term $\mathcal{H}_{\mathrm{Q}}$ contains the interaction between the nuclear quadrupole moment of a nucleus having $I > 1/2$ and the electric field gradient at its site.

The hf or shf tensor **A** can be split into an isotropic part a and a traceless anisotropic part **B**.

$$\mathbf{A} = a \cdot \mathbf{E} + \mathbf{B}, \tag{1.13}$$

where **E** is the 3×3 unit matrix. Since the trace of the anisotropic hf or shf tensor is zero, the tensor can be described in its principal axes system by the two independent interaction parameters

$$b = \frac{B_{zz}}{2} \tag{1.14}$$

and $$b' = \frac{B_{xx} - B_{yy}}{2}.$$

The scalar a, the so-called Fermi contact interaction constant, is proportional to the unpaired spin density at the site of a nucleus in a one-particle approximation for the centre wave function $\psi(\mathbf{r})$ [13].

$$a = \frac{2}{3}\mu_{\mathrm{o}} g_{\mathrm{e}} \mu_{\mathrm{B}} g_{\mathrm{n}} \mu_{\mathrm{n}} \cdot |\psi(0)|^2, \tag{1.15}$$

where μ_{o} is the permeability of a vacuum. The matrix elements of the anisotropic part **B** are given by [13]

$$B_{ik} = \frac{1}{4\pi}\mu_{\mathrm{o}} g_{\mathrm{e}} \mu_{\mathrm{B}} g_{\mathrm{n}} \mu_{\mathrm{n}} \cdot \int \left\{ \frac{3x_i x_k}{r^5} - \frac{\delta_{ik}}{r^3} \right\} |\psi(\mathbf{r})|^2 \mathrm{d}\mathbf{r}. \tag{1.16}$$

The quadrupole tensor **Q**, which does not vanish for nuclei with spin $I > 1/2$, is defined by

$$Q_{ik} = \frac{eQ}{2I(2I-1)} \cdot \left. \frac{\partial^2 V}{\partial x_i \partial x_k} \right|_{r=0} \tag{1.17}$$

with e elementary charge,
Q quadrupole moment of a nucleus,
V electric potential at the site of a nucleus.

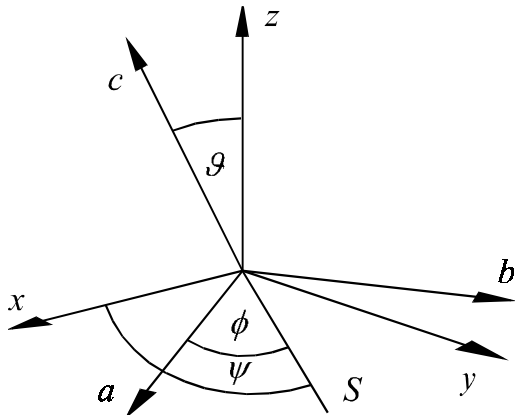

Figure 1.4 Definition of the Euler angles describing the tensor orientations. *a*, *b*, and *c* are the crystal axes, whereas *x*, *y*, and *z* are the principal axes of the tensor. The *ab* plane cuts the *xy* plane along line *S*.

The quadrupole tensor **Q** is also traceless and can be described analogously to the anisotropic hf or shf tensor in its principal axes system by the two parameters

$$q = \frac{Q_{z'z'}}{2} \tag{1.18}$$

and $$q' = \frac{Q_{x'x'} - Q_{y'y'}}{2}.$$

The z axis of the hf, shf or quadrupole tensor's principal axes system is to be aligned along the direction of the largest interaction by definition. Consequently, b and q yield the axially symmetric parts of each tensor, whereas b' and q' describe the deviation from axial symmetry.

Since the principal axes system of the interaction tensors (x, y, z) does often not coincide with the crystalline axes system or the laboratory system (a, b, c), the relative position of the tensor principal axes system can be described by Euler angles (figure 1.4).

The exact determination of the energy levels of a spin system requires a full diagonalisation of the appropriate spin Hamiltonian. For a rough estimation perturbation theory of first or second order is often helpful, provided that one term of the Hamiltonian dominates. For example if $\mathcal{H}_{EZ} >> \mathcal{H}_{SHF}$ the interaction for a simple $S = 1/2$ system with isotropic electronic and nuclear g-factors and one neighbour nucleus is given in first order perturbation theory by

$$E = m_S g\mu_B B + m_S m_I W_{SHF} - m_I g_n \mu_n B + \frac{1}{2} W_Q \left\{ m_I^2 - \frac{I(I+1)}{3} \right\} \tag{1.19}$$

with $W_{SHF} = a + b \cdot \left(3\cos^2 \vartheta - 1\right) + b' \cdot \sin^2 \vartheta \cdot \cos(2\phi)$

and $W_Q = 3q \cdot \left(3\cos^2 \vartheta' - 1\right) + 3q' \cdot \sin^2 \vartheta' \cdot \cos(2\phi')$.

ϑ and ϑ' are the angles between the z axis of the respective principal axes system and the magnetic field vector, ϕ and ϕ' the angles between the x axis and the projection of the magnetic field vector into the xy plane of the respective principal axes system (see e.g., [10]).

1.3.2 Analysis of EPR spectra

EPR spectra are analysed by determining the energy differences between the levels for which transitions obeying the selection rules $\Delta m_S = \pm 1$ and $\Delta m_I = 0$ occur. For a $S = 1/2$ system equation (1.19) yields the energy positions of the allowed EPR transitions according to first order perturbation theory.

$$h\nu_{EPR} = g\mu_B B + m_I W_{SHF} \tag{1.20}$$

In an EPR experiment the microwave frequency is fixed while the magnetic field is swept. Thus equation (1.20) has to be solved for the corresponding resonant magnetic fields. The interaction matrices can be obtained by rotating the magnetic field vector in two perpendicular planes (or rotating the crystal relative to the fixed magnetic field). The angular dependencies usually yield much more resonances than needed for the determination of the spin Hamiltonian parameters. Therefore, the interaction tensors are adjusted to the observed resonances in an iterative procedure where the weighted sum of the deviation squares of the measured and the calculated resonances is minimised.

1.3.3 Analysis of ENDOR spectra

ENDOR transitions obey the selection rules $\Delta m_S = 0$ and $\Delta m_I = \pm 1$. According to equation (1.19) first order theory yields

$$h\nu_{ENDOR} = \left| m_S W_{SHF} - g_n \mu_n B + m_Q W_Q \right| \tag{1.21}$$

with $m_Q = (m_I + m_I')/2$.

m_I and m_I' represent the nuclear spin states between which the ENDOR transition occurs. By analogy to the EPR analysis also here the corresponding interaction matrices are obtained by recording ENDOR angular dependencies for a rotation of the magnetic field vector in two perpendicular planes and fitting the interaction parameters to the experimental data afterwards.

According to their separation from the defect centre, neighbouring nuclei are classified in different shells. The symmetry of a shell is determined by symmetry elements which transform the shell's nuclei into each other. The origin of each symmetry operation is the point group symmetry of defect centre and a centre of inversion, i.e., is determined by the Laue class of the centre (site). Each nucleus of a shell leads to a certain ENDOR line and thus to an ENDOR branch in the angular dependence.

1.3.4 Calculation of powder EPR and ENDOR spectra

With the data known from a single crystal, the corresponding powder EPR spectrum can be calculated. For the individual EPR lines and inhomogeneous broadening, one can assume a Gaussian line shape Ω_{EPR} according to

$$\Omega_{\mathrm{EPR}}(B) = \frac{1}{\sigma_{\mathrm{EPR}}\sqrt{2\pi}} \exp\left\{-\frac{1}{2}\frac{(B_{\mathrm{o}}(\vartheta,\phi) - B)^2}{\sigma_{\mathrm{EPR}}^2}\right\} \tag{1.22}$$

with $\sigma_{\mathrm{EPR}} = \dfrac{\Delta B}{2\sqrt{2\ln 2}}$

whereby ΔB is the full width at half maximum of the EPR line. Since the EPR line positions B_{o} are angular dependent, one has to integrate over all possible orientations of the magnetic field.

For the calculation of powder ENDOR spectra, one has to consider that the intensity of an ENDOR line at a certain magnetic field is proportional to the intensity of an EPR line at that field. Therefore, the intensity of the ENDOR signals at the applied magnetic field B_{ENDOR} has to be weighted with the intensity of the EPR line at this field. An ENDOR frequency depends on the orientation of the magnetic field with respect to the principal axes of the interaction tensors. Therefore, in order to calculate the intensity of

an ENDOR line for a certain frequency ν at a magnetic field B_{ENDOR} and assuming a Gaussian line shape, one obtains

$$\Omega_{\mathrm{ENDOR}}(\nu) = \frac{1}{\sigma_{\mathrm{EPR}}\sqrt{2\pi}} \exp\left\{-\frac{1}{2}\frac{(B_{\mathrm{o}}(\vartheta,\phi) - B_{\mathrm{ENDOR}})^2}{\sigma_{\mathrm{EPR}}^2}\right\} \times$$

$$\frac{1}{\sigma_{\mathrm{ENDOR}}\sqrt{2\pi}} \exp\left\{-\frac{1}{2}\frac{(\nu_{\mathrm{ENDOR}}(\vartheta,\phi,B_{\mathrm{ENDOR}}) - \nu)^2}{\sigma_{\mathrm{ENDOR}}^2}\right\} \qquad (1.23)$$

where the polar angle ϑ and the azimuthal angle ϕ describe the orientation of the static magnetic field B_{o} with respect to the crystal axes. In order to obtain the powder ENDOR spectrum as a function of the rf frequency ν, one has to integrate equation (1.23) over all angles of ϑ and ϕ (see e.g., [18]).

Chapter 2

X-ray storage phosphors

2.1 Performance

To determine the performance of an X-ray storage phosphor a read-out experiment must be performed (figure 2.1). After X-irradiation at RT the sample is excited continuously with the appropriate stimulation light. A photomultiplier detects the resulting photostimulated luminescence (PSL) versus time. For detailed information see e.g. [19].

Continuous photostimulation leads to a decrease of the number of the PSL-active centres. Consequently, the PSL intensity decays under continuing stimulation. The area below the PSL curve is proportional to the absorbed X-ray dose. In a commercial system a laser beam is used to read out the information stored in the phosphor screen point by point and line by line. The information should be read-out in the shortest time possible. To describe the characteristics of an X-ray storage phosphor the quantities "conversion efficiency" (CE) and "stimulation energy" (SE) determining these requirements are introduced.

CE is defined as the released photon energy (E_{tot}) per absorbed X-ray dose

$$\mathrm{CE} = \frac{E_{\mathrm{tot}}}{\text{absorbed X - ray dose}}, \tag{2.1}$$

where E_{tot} is the area below the PSL curve.

In the simplest case the time dependence of the PSL can be described by a monoexponential decay, i.e.

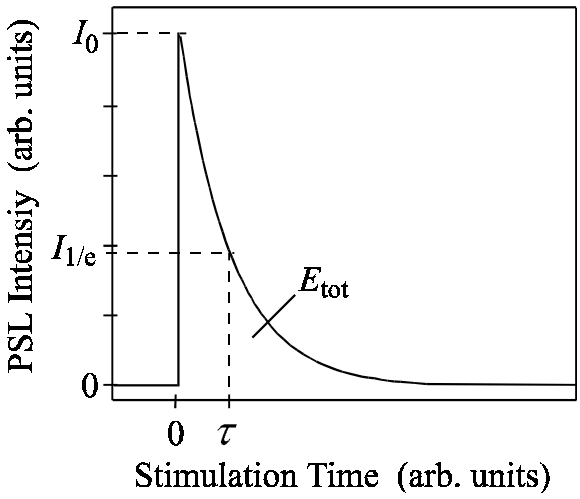

Figure 2.1 Typical PSL decay curve of an X-ray storage phosphor under continued stimulation.

$$I(t) = I_0 \cdot \exp(-t/\tau)\,. \tag{2.2}$$

I_o is the amplitude of the PSL at the beginning of the stimulation experiment, t the stimulation time and τ a time constant depending on the power P of the stimulation light (see definition of stimulation energy) and limited by the characteristic decay time of the activator luminescence.

Thus, E_{tot} is obtained by integrating $I(t)$ from $t = 0$ to $t = \infty$,

$$\begin{aligned} E_{tot} &= I_0 \cdot \int_0^{\infty} \exp(-t/\tau)\ \mathrm{d}t \\ &= I_0 \cdot \tau \cdot \left\{ \exp(-t/\tau)\big|_0 - \exp(-t/\tau)\big|_{\infty} \right\} \\ &= I_0 \cdot \tau\,. \end{aligned} \tag{2.3}$$

Finally, CE is determined by

$$\mathrm{CE} = \frac{I_0 \cdot \tau}{\text{absorbed X-ray dose}}\,. \tag{2.4}$$

In the experiment the time constant τ, after which the PSL intensity is decreased to 1/e of its initial value, as well as the initial PSL intensity I_0 are measured.

The stimulation energy (SE), i.e. the energy required to reduce the PSL intensity to $1/e$ of its initial value, is defined as

$$\mathrm{SE} = \tau \cdot P, \tag{2.5}$$

where P is the power of the applied stimulation light beam.

The sensitivity of an X-ray storage phosphor is proportional to the stored energy and proportional to the inverse of energy required for the read-out. Therefore, the sensitivity is given by the ratio CE/SE.

2.2 Spatial resolution of X-ray storage phosphor image plates

2.2.1 Image sharpness

The image of an infinitely sharp edge obtained by an X-ray imaging system based on storage phosphor screens should have a sharp step in the detected luminescence intensity from zero to a certain luminescence intensity level proportional to the absorbed X-ray dose (figure 2.2a (left)). Unfortunately, this is only valid in an ideal case whereas in reality, the image does not yield such a sharp step, but a region of unsharpness in which the luminescence signal changes steadily from zero to the corresponding luminescence intensity (figure 2.2b (left)). The sharpness of such an imaging system can either be described by imaging of an infinitely sharp edge or by imaging of an infinitely narrow slit. An ideal image of such a slit would be an infinitely small square function for the luminescence intensity (figure 2.2a (right)). In reality one gets a bell-shaped curve the half width of which determines the sharpness of the system (figure 2.2b (right)).

2.2.2 Modulation transfer function

One way to assess the image quality is to express it in terms of the resolving power of the imaging system, i.e. the smallest separation of a pair of linear objects at which the images do not merge. A very useful tool to describe the image sharpness of an X-ray imaging system is the concept of the modulation transfer function (MTF). This is based on the ideas of a Fourier analysis, for detailed information see e.g. [20].

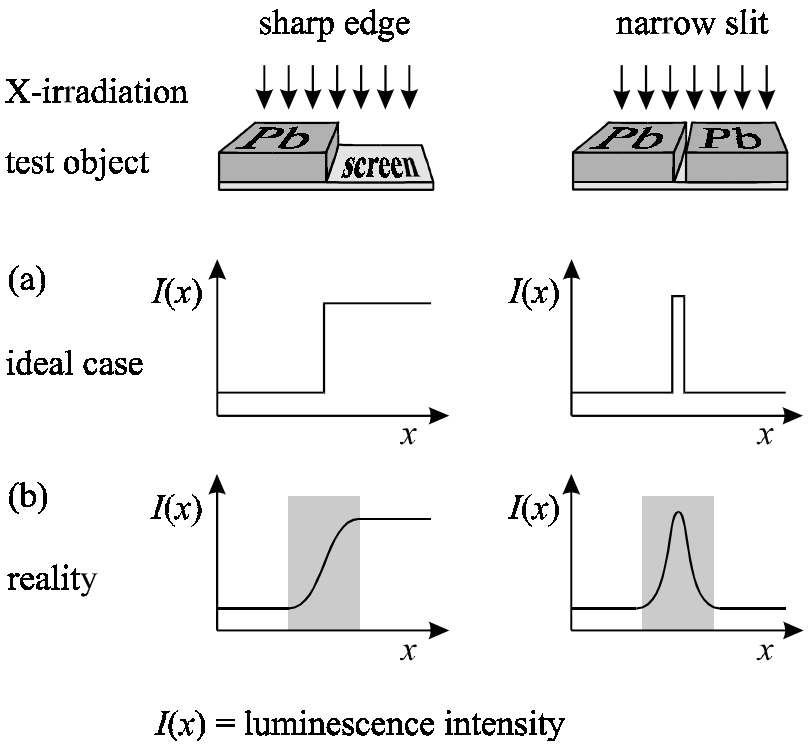

Figure 2.2 Imaging of a sharp edge (left) and a narrow slit (right) by an X-ray imaging system based on X-ray storage phosphors.

Starting at the object, at any stage in the imaging process all the available information can be expressed in terms of spatial frequencies. The idea of spatial frequency can be understood by considering two ways of describing a simple object consisting of a set of equally spaced parallel lines. The usual convention would be to say the lines were equally spaced 0.2 mm apart. Alternatively, one could say that the lines occur with a frequency in space (spatial frequency) of five per mm. In general, the finer the detail the greater the intensity of high spatial frequencies in the spatial frequency spectrum. Thus, fine detail, or high resolution, is associated with high spatial frequencies [21].

The imaging process converts the two-dimensional radiation image $g(x,y)$ into a two-dimensional visible image $b(x,y)$. For the sake of simplicity the radiation image is taken here to change only in one dimension. The imaging process can then be described by

$$g(x) \rightarrow b(x)\,. \tag{2.6}$$

A linear imaging system is characterised by the fact that a sinusoidal radiation image

$$g(x) = A_{\text{in}}(k)\cdot\sin(kx) \tag{2.7}$$

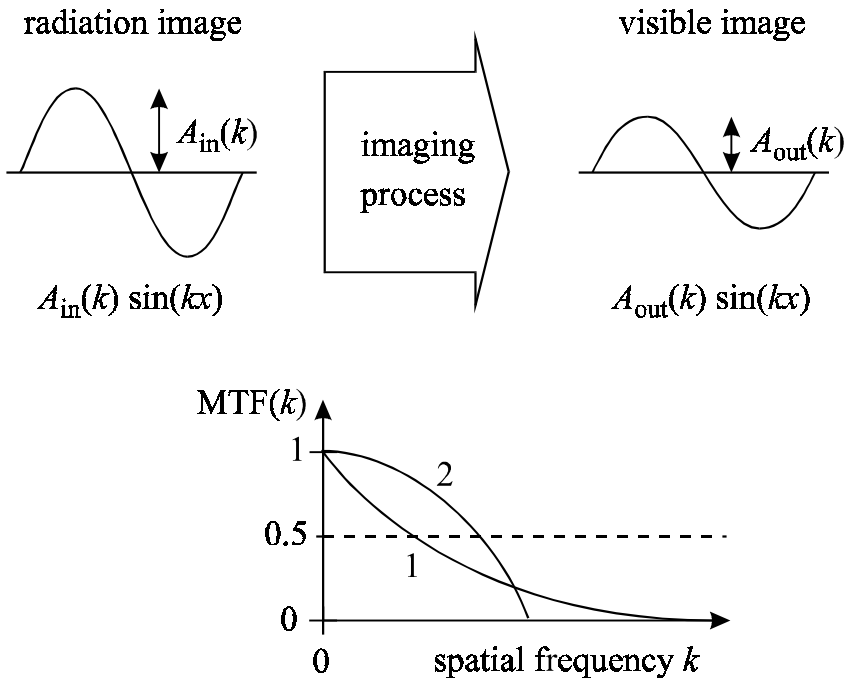

Figure 2.3 Imaging of a sinusoidal radiation image and two arbitrary modulation transfer functions (MTF).

is converted into a sinusoidal visible image

$$b(x) = A_{\text{out}}(k) \cdot \sin(kx) \,. \tag{2.8}$$

Hereby, the parameter k, which has the dimension of a reciprocal length, denotes the spatial frequency. The modulation transfer function (MTF) is defined as

$$\text{MTF}(k) = A_{\text{out}}(k) / A_{\text{in}}(k) \,. \tag{2.9}$$

The modulation transfer function describes the transfer conditions of an imaging system. It defines how the image contrast decreases with higher spatial frequencies. The highest spatial resolution is determined by the point of intersection between the MTF and a line which represents a smallest detectable contrast. Another characteristic value often used is the spatial frequency, where the MTF(k) is decreased to 50% (figure 2.3). The two MTF curves of figure 2.3 show that the spatial resolution characterises the performance of an imaging system insufficiently. The imaging system represented by curve 1 has a significantly higher spatial resolution as system 2, but for average spatial frequencies the modulation transfer and thus the image contrast for objects having these spatial frequencies is much worse than that of curve 2.

2.2.3 Description of imaging processes via Fourier transformation

The mathematical derivation of the modulation transfer function (MTF) assumes a sinusoidally varying object which is very difficult to realise practically. Thus, the relation between the MTF and the imaging of other objects has to be clarified. The imaging process of an arbitrary object function $g(x)$ via a system having a modulation transfer function MTF(k) can be described by the following:

The object function $g(x)$ can be Fourier transformed into its corresponding frequency spectrum $G(k)$ by

$$G(k) = \int_{-\infty}^{+\infty} g(x) \cdot \mathrm{e}^{-\mathbf{i}2\pi kx} \mathrm{d}x \tag{2.10}$$

According to equation (2.9) the spatial frequency spectrum of the image can be obtained by a multiplication with the modulation transfer function MTF(k).

$$B(k) = \mathrm{MTF}(k) \cdot G(k) \tag{2.11}$$

Inverse Fourier transformation leads to the image function

$$b(x) = \int_{-\infty}^{+\infty} B(k) \cdot \mathrm{e}^{\mathbf{i}2\pi kx} \mathrm{d}k = \int_{-\infty}^{+\infty} \mathrm{MTF}(k) \cdot G(k) \cdot \mathrm{e}^{\mathbf{i}2\pi kx} \mathrm{d}k \,. \tag{2.12}$$

For the Dirac delta function $\delta(x)$ as object function, that means an infinitely fine detail, one obtains with equation (2.10) a spatial frequency spectrum of $G(k) = 1$. Equation (2.12) simplifies to

$$b(x) = \int_{-\infty}^{+\infty} \mathrm{MTF}(k) \cdot \mathrm{e}^{\mathbf{i}2\pi kx} \mathrm{d}k = \mathrm{LSF}(x) \,. \tag{2.13}$$

The image function $b(x)$ of the Dirac delta function $\delta(x)$ is called the line spread function LSF(x). The integral over the line spread function LSF(x) yields the edge spread function ESF(x). The relations between LSF(x), ESF(x) and MTF(k) are given by

$$\mathrm{LSF}(x) = \frac{\mathrm{d}}{\mathrm{d}x} \mathrm{ESF}(x) \tag{2.14}$$

$$\mathrm{MTF}(k) = \int_{-\infty}^{+\infty} \mathrm{LSF}(x) \cdot \mathrm{e}^{-\mathbf{i}2\pi kx} \mathrm{d}x \tag{2.15}$$

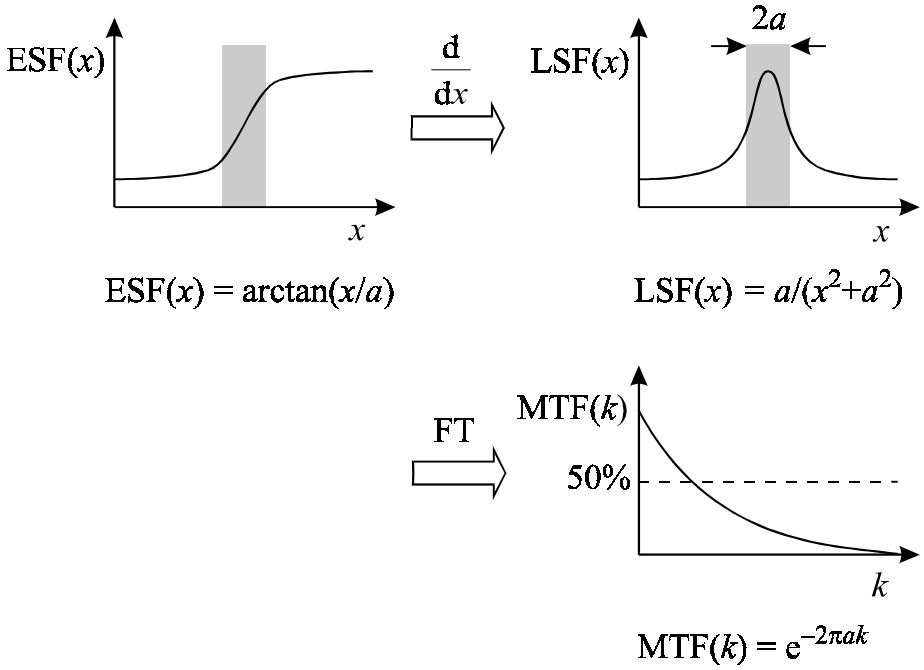

Figure 2.4 Theoretical example for the determination of the MTF(k) of a given ESF(x).

Figure 2.4 shows a theoretical example for the transformations described above. In practice one measures the ESF(x) of an infinitely sharp edge and determines the MTF(k) via numerical differentiation and subsequent fast Fourier transformation.

2.2.4 Measurement of the spatial resolution and the modulation transfer function

The assessment of image quality is obtained practically by means of special test objects. The spatial resolution is usually determined with a lead grid, where the spatial frequency (line pairs per mm) changes stepwise from one line pair to the next (figure 2.5a). Here, a spatial frequency of one (two, four, five) line pair(s) per mm corresponds to a set of 500 µm (250 µm, 125 µm, 100 µm) fine lines which are spaced 500 µm (250 µm, 125 µm, 100 µm) apart. The highest spatial frequency which is detectable upon imaging of such a lead grid yields the spatial resolution of the investigated imaging system.

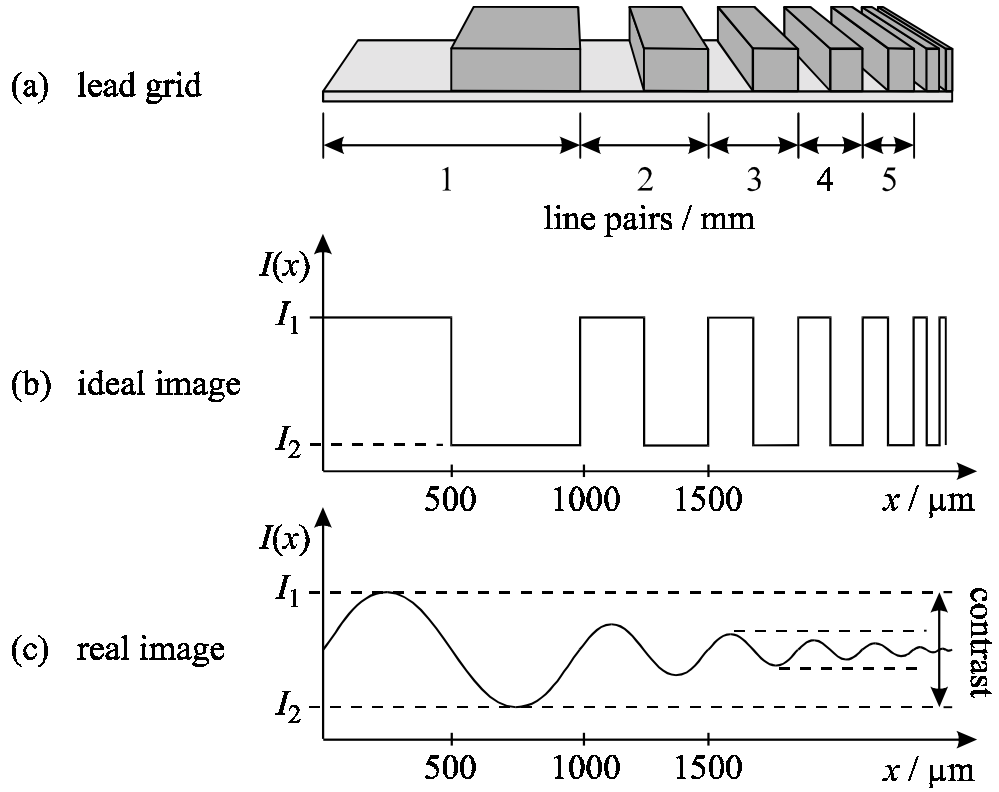

Figure 2.5 Determination of the contrast modulation and thus the contrast transfer function by imaging of a lead grid.

The spatial resolution does not characterise an imaging system sufficiently. It is often useful to determine the modulation transfer function. This requires, however, much more experimental effort. There are, in principle, two ways to determine the MTF:

One method is based on a quantitative analysis of the image of the lead grid (figure 2.5). Figure 2.5c shows that the measured contrast modulation depends on the spatial frequency k. The contrast can be described with the luminescence intensities I_1 and I_2 by

$$C = (I_1 - I_2)/(I_1 + I_2)\,. \tag{2.16}$$

For the ideal image of the lead grid (figure 2.5b), the intensities I_1 and I_2 do not change upon increasing the spatial frequency. Thus, the resulting contrast function $C_{\text{ideal}}(k)$ is constant. For the real image (figure 2.5c), I_1 and I_2 change upon increasing the spatial frequency k and the value of the contrast function $C_{\text{real}}(k)$ decreases. The analysis of this dependence yields the contrast transfer function (CTF) which is defined as

$$\text{CTF}(k) = C_{\text{real}}(k)/C_{\text{ideal}}(k) = C_{\text{real}}(k)/\text{const}\,. \tag{2.17}$$

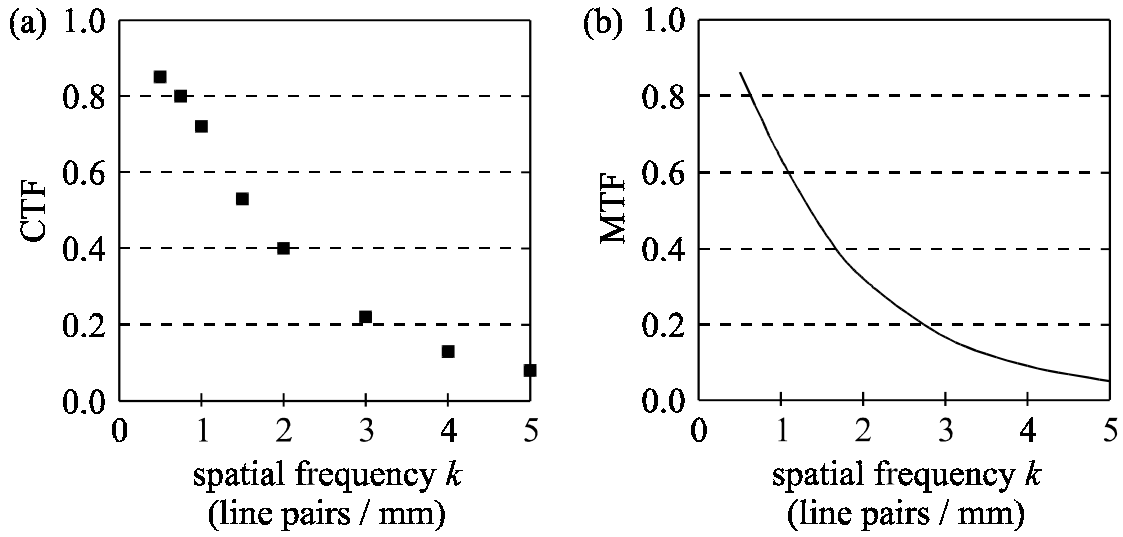

Figure 2.6 (a) Measured data of the contrast transfer function (CTF) and (b) modulation transfer function (MTF), derived from the data of (a), for a commercially-used image plate (AGFA MD 10) [22].

The CTF (figure 2.6a) can afterwards be transformed into the modulation transfer function (MTF) (figure 2.6b). Since the MTF assumes a sinusoidal varying object, the square wave function of the grid (figure 2.5b) is approximated by a series of sinusoidal functions.

The other technique is the exact analysis of a line spread function LSF(x) and subsequent Fourier transformation. Due to experimental reasons one measures often the edge spread function ESF(x) and gets the LSF(x) via differentiation.

2.3 Read-out process of X-ray storage phosphor image plates

During the read-out process the X-ray storage phosphor image plate is optically stimulated pixel by pixel and line by line by means of a laser beam, e.g. a HeNe laser (632.8 nm) for the commercially used BaFBr:Eu^{2+} phosphor screen. The photostimulated luminescence light is collected globally with a waveguide and detected by a photomultiplier. The stimulation light is cut off by means of an appropriate optical filter combination which is placed between the waveguide and the photomultiplier (not indicated in figure 2.7). The detected luminescence intensity during stimulation of a pixel is

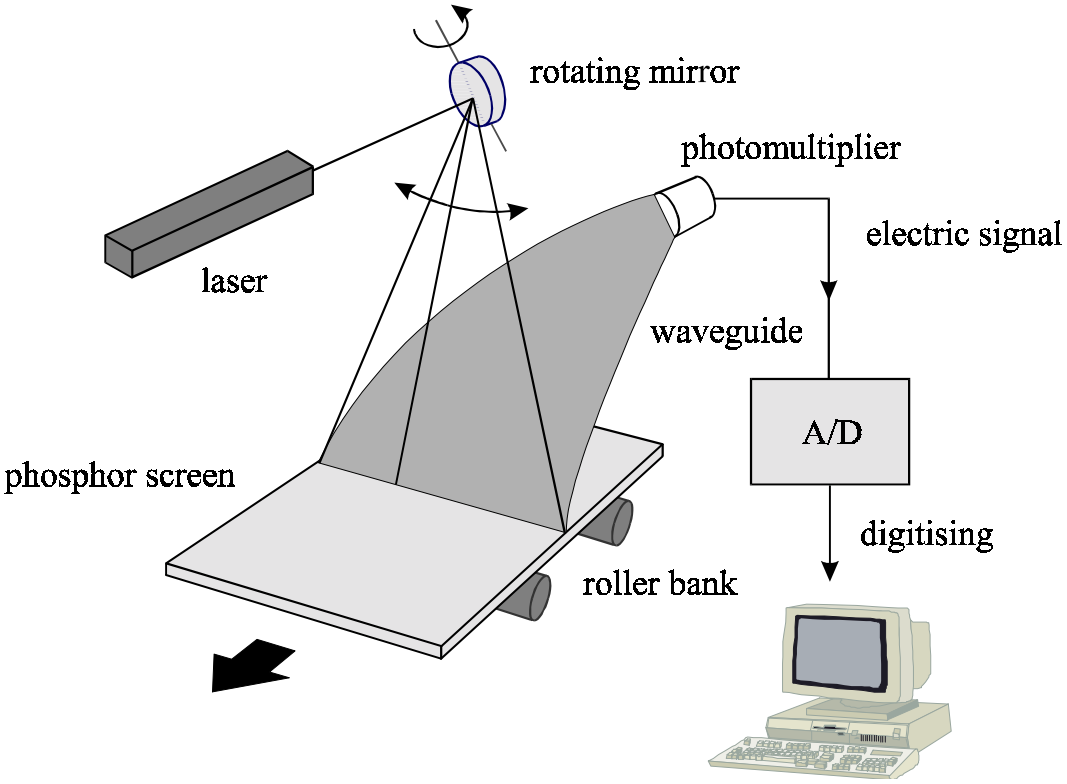

Figure 2.7 Setup for the read-out procedure of X-ray storage phosphor image plates [22].

a measure for the absorbed X-ray dose in that pixel. The analogue signal of the photomultiplier is converted by an analogue/digital (A/D) converter to a digital signal. The scanning procedure is carried out by moving the laser with a rotating mirror and/or the image plate with the roller plate (figure 2.7).

The spatial resolution of X-ray storage phosphor screens is still inferior to that of conventional X-ray films. One of the reasons for this is certainly the light scattering of the scanning laser beam which is used for the read-out. The structural reasons for this are explained in figure 2.8: The image plate consists of fine phosphor grains imbedded in an organic binder. The phosphor/binder layer is deposited on an organic substrate and protected by a thin foil. During the read-out the stimulating light of the scanning laser beam is scattered within the phosphor/binder layer due to the different refractive indices of the two components. The scattered stimulating light can then excite the electron trap centres in the X-irradiated areas and cause photostimulated luminescence (PSL) although the scanning laser beam is not in the right position yet. The luminescence light is detected globally on the side of the stimulation. The sharp edges of the X-irradiated

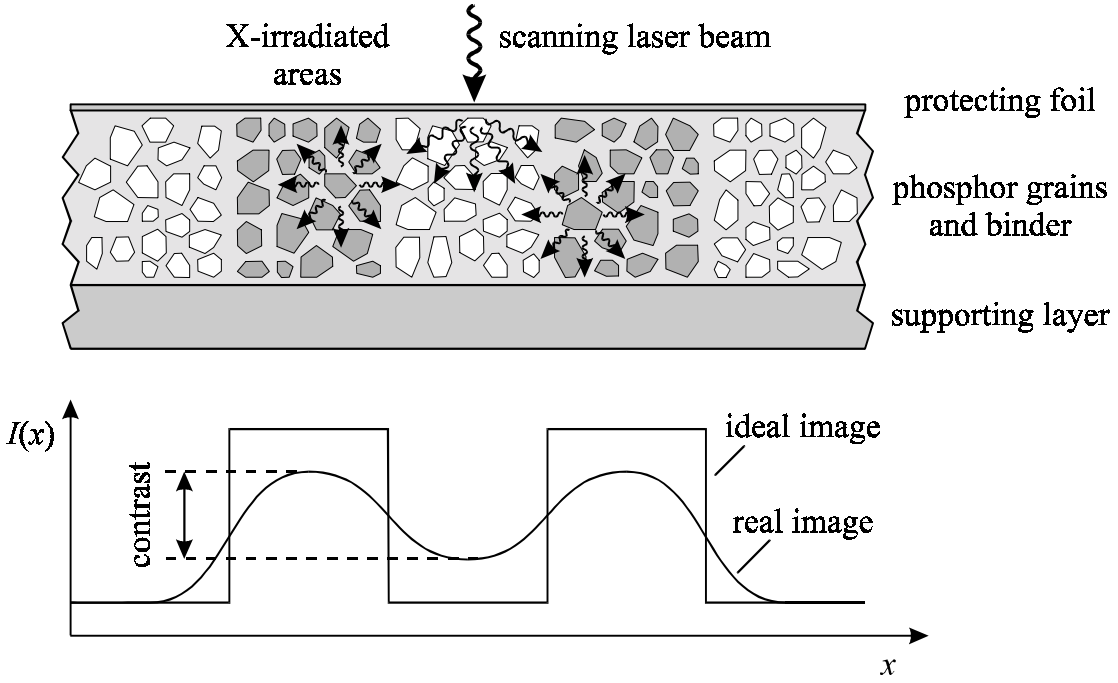

Figure 2.8 Scattering of the scanning laser beam during the read-out process of a storage phosphor image plate.

areas are spread and the contrast modulation is reduced. For a contrast modulation below the smallest detectable contrast the two X-irradiated areas in figure 2.8 cannot be resolved any more. Here, the detection of the luminescence light is done globally on the stimulation side of the phosphor screen and not focussed on the laser beam position in the layer. The spatial resolution is thus determined by the scattering region, i.e. the excitation volume of the stimulating light.

Chapter 3

The X-ray storage phosphor BaFBr:Eu^{2+}

The so far best and world-wide commercially used X-ray storage phosphor is BaFBr doped with Eu^{2+} as activator [1]. Upon X-irradiation, room temperature (RT) stable electron and hole trap centres are generated. The electron trap centres are photostimulable and the electron recombines upon photostimulation with the hole trap centre under light emission. Although the principle of information storage and read-out mechanism is simple, it is not clearly known how the recombination energy is transferred to the activator Eu^{2+} which emits at 3.18 eV (390 nm). The PSL decay time is 750 ns [1, 23]. In many years of thorough research and optimisation BaFBr:Eu^{2+} has already reached a very high level of performance. However, there is still space for some improvements such as e.g. a better conversion to PSL-active centres [24], a higher stability of the PSL active centres, and a better erasability of the generated defects after the read-out process. The spatial resolution can probably not be improved. For recent reviews see e.g. [2, 3, 4, 5, 25].

3.1 Stoichiometric BaFBr

3.1.1 Generation of electron trap centres

There is general agreement that X-irradiation generates F centres as electron trap centres. In BaFBr, which has the matlockite structure [26, 27], two F centres are possible, $F(Br^-)$ and $F(F^-)$ centres, where electrons are trapped at Br^- vacancies or F^- vacancies,

respectively. Their generation mechanism, however, is controversial. In order to form an F centre after creating electron-hole pairs by X-irradiation, one either needs to have a halide vacancy present in the crystal or one must generate it during the radiation damage process.

In [28] it was assumed that Br^- vacancies are already present in the material. However, no experimental evidence was given for this assumption. In [29] it was shown that photostimulable centres can be created by using vacuum UV light instead of X-rays and concluded that the decay of self-trapped excitons into F and H centres (Br_2^- centres on a halide lattice site, see e.g. [30]), provide the necessary mechanism to create F centres.

H centres were not detected, though, in spite of an intense search for them at 1.5 K by EPR and optically detected EPR using the magneto-optical method (MCDA-EPR). Had there been H centres, they would have been detectable using MCDA-EPR. It was shown in [31] that H centres created in KBr can be measured in this way.

When measuring the photostimulation as a function of photon energy, two peaks are usually observed: One at 2.15 eV and one around 2.65 eV. The two peaks are clearly resolved when using single crystals and polarised light (e.g. $\mathbf{E} \perp \mathbf{c}$) [32, 33]. The spectral shape of the excitation spectrum of the photostimulated luminescence (figure 3.1b) agrees very well with the optical absorption band of $F(Br^-)$ centres (peak at 2.15 eV for $\mathbf{E} \perp \mathbf{c}$) and $F(F^-)$ centres (peak at 2.65 eV for $\mathbf{E} \perp \mathbf{c}$) (figure 3.1a). The absorption band for $\mathbf{E} \perp \mathbf{c}$ was clearly identified for each F centre by magneto-optical techniques [34]. Although it was argued that only $F(Br^-)$ centres are photostimulable [24], it could be clearly shown that both F centres contribute to the PSL [32, 33]. Yet it was interesting to observe that $F(F^-)$ centres are only generated by X-irradiation above 200 K. Their formation apparently requires a thermally activated process. When observing the generation of both centres as a function of the X-ray dose, it turns out, however, that $F(F^-)$ centres are not generated as a secondary product of $F(Br^-)$ centres. $F(Br^-)$ centres are generated first and then saturate, whilst $F(F^-)$ centres continued to be generated, but not at the expense of the $F(Br^-)$ centres. The process has not yet been understood [15]. When no F-H centre mechanism is responsible for the generation of $F(Br^-)$ centres, which are found even at the lowest temperature (1.5 K) upon X-irradiation together with V_K centres (hole shared between two adjacent Br^- [32]) as "anti-centres" (see figure 3.2a), it must indeed be assumed that BaFBr does contain Br^- vacancies (V_{Br^-}).

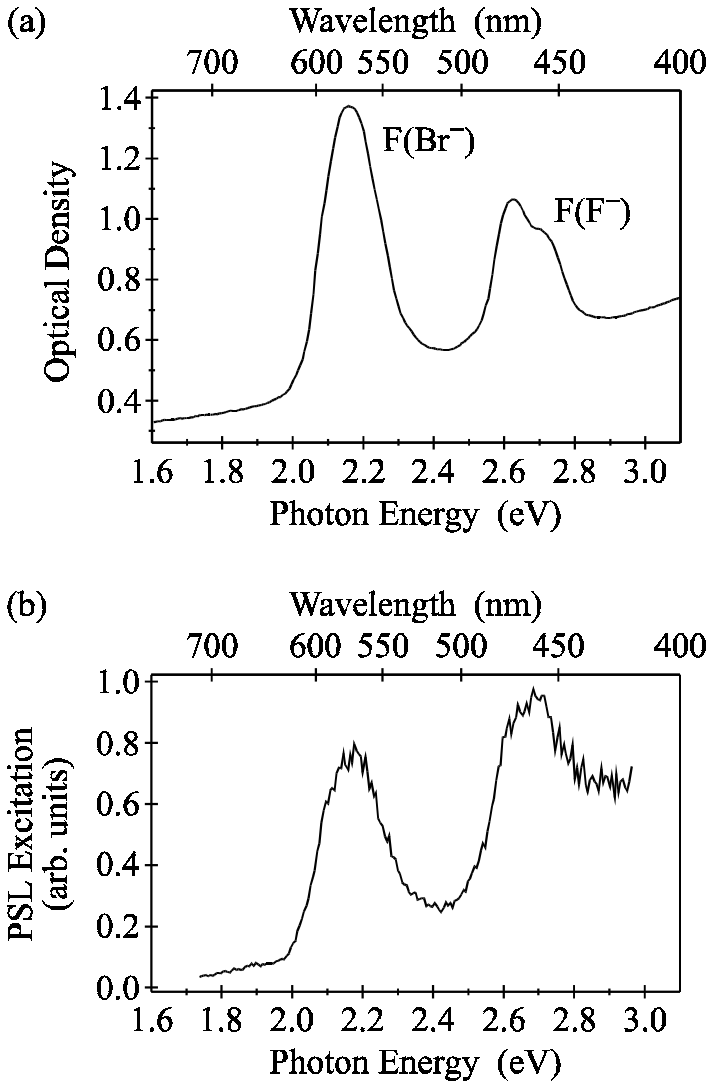

Figure 3.1 (a) Optical absorption spectrum of $F(Br^-)$ and $F(F^-)$ centres in BaFBr and (b) PSL excitation spectrum of Eu^{2+} in BaFBr. Both spectra were recorded at 10 K for $\mathbf{E} \perp \mathbf{c}$ after X-irradiation at RT [32].

3.1.2 Generation of hole trap centres

It was long overlooked that BaFBr produced by firing stoichiometric mixtures of BaF_2 and $BaBr_2$ or by growing single crystals from the melt of such mixtures with the Bridgman method are all contaminated with oxygen, irrespective of the manufacturer. All attempts to eliminate oxygen completely have failed. Very careful avoidance of oxygen could only reduce the oxygen contamination [35, 36]. Oxygen can be incorpo-

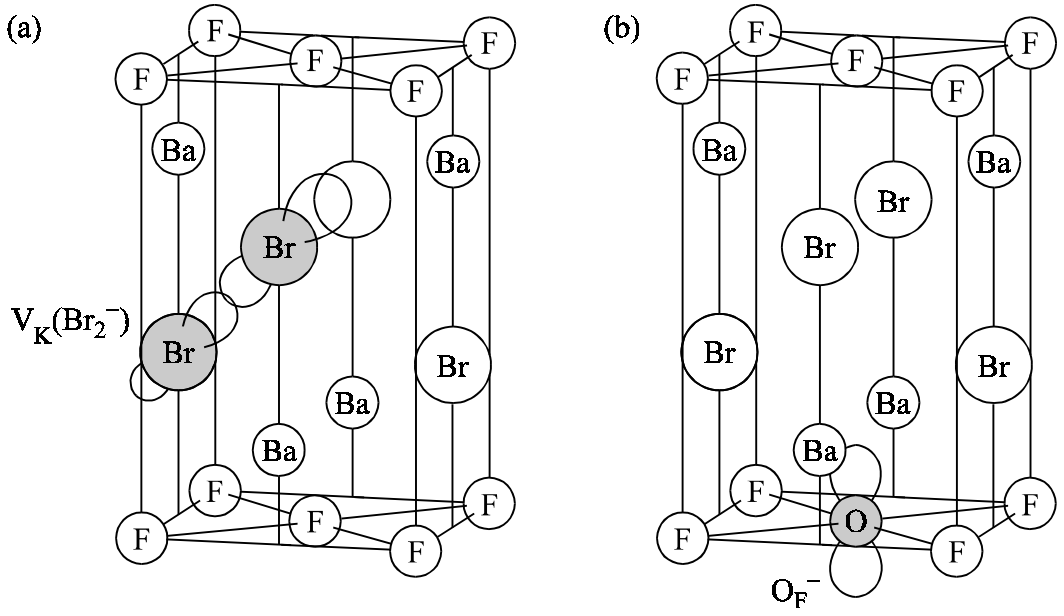

Figure 3.2 Model of (a) the $V_K(Br^-)$ and (b) the O^- centre in BaFBr.

rated in many ways: It was found as O^{2-} in the fluorine (O_F^{2-}) [37] as well as in the bromine sublattice (O_{Br}^{2-}) [38, 39]. There was also a molecular oxygen centre ((O_F-O_{Br})$^{3-}$) observed where one oxygen is placed on a fluorine site and the other one on a neighbouring bromine site [39].

For charge compensation an anion vacancy is needed. It was shown by the study of the generation of F centres, V_K centres and O^- centres at low temperature using magneto-optical (MCDA) and MCDA-EPR methods that these vacancies are indeed Br^- vacancies [15, 35, 36]. Upon X-irradiation at temperatures below 120 K $V_K(Br_2^-)$ centres and F(Br^-) centres are formed, the latter being near to the O_F^{2-} centres. Above 120 K the $V_K(Br_2^-)$ centres become mobile, react with the O_F^{2-} centres and form O_F^- hole trap centres. Above 200 K the F(Br^-) centres can diffuse away and become isolated [37, 40]. The microscopic structure of the O_F^- defect (figure 3.2b) was established by EPR and ENDOR. Figure 3.3 shows the EPR spectrum of $^{17}O_F^-$ centres in BaFBr. The magnetic oxygen isotope ^{17}O has a nuclear spin of $I = 5/2$ and hence shows a hyperfine splitting into 6 lines. The isotope substitution of ^{17}O for ^{16}O proved that the defect centre of figure 3.3, always produced upon X-irradiation of BaFBr, is due to an oxygen contamination [37].

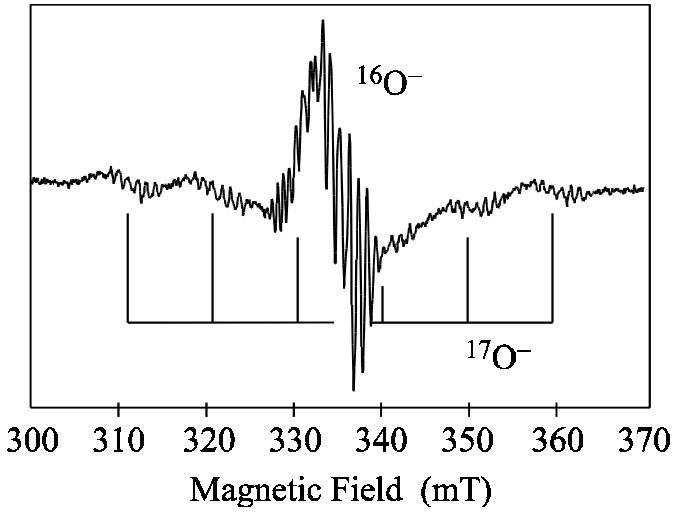

Figure 3.3 EPR spectra of the O_F^- centre in ^{17}O-doped BaFBr after X-irradiation at RT, recorded for $\mathbf{B} \| \mathbf{c}$ at $T = 5$ K applying a microwave frequency of 9.42 GHz. The bars indicate the ^{17}O hyperfine splittings [37].

It can be assumed that the BaFBr used by [29] also contained oxygen and thus the UV production of F(Br$^-$) centres becomes understandable by the process

$$V_{Br^-} + O_F^{2-} \xrightarrow{\text{UV, X-ray}} F(Br^-) + V_K(Br_2^-) + O_F^{2-} \tag{3.1}$$

$$\xrightarrow{> 120\ \text{K}} F(Br^-) + O_F^-\,.$$

Thus, the generation of F(Br$^-$) centres in oxygen-contaminated, stoichiometric BaFBr is understood, whereas the mechanism leading to F(F$^-$) centres remains still unclear. The microscopic structure of the two F centres was established by detailed ENDOR investigations [41].

3.1.3 PSL active hole trap centres

The nature of the hole trap centre taking part in the PSL process is still unclear and controversially discussed. In [28, 42] it was claimed that upon electron and hole creation by X-rays holes are trapped at Eu^{2+} and form Eu^{3+}. Upon photostimulation of F centres, the F electrons move through the conduction band and recombine with Eu^{3+}, exciting Eu^{2+} to its excited state, from which the 390 nm luminescence occurs. In this model the PSL process requires thermal activation, since the excited F centres have re-

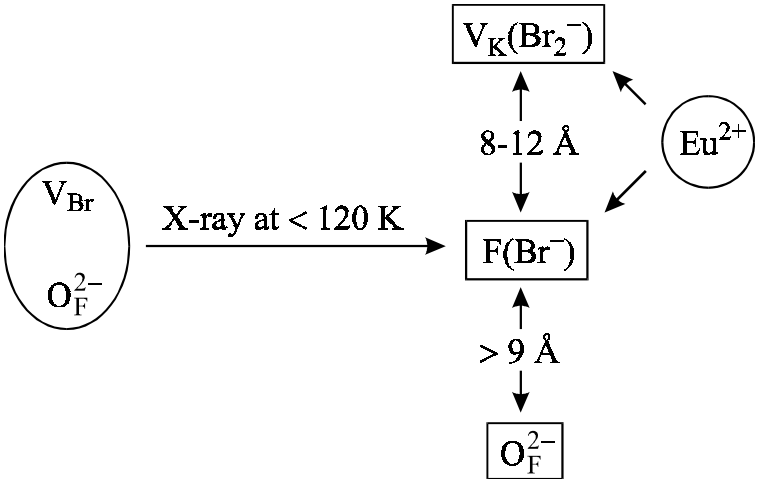

Figure 3.4 Schematic model for the spatial correlation between $F(Br^-)$, $V_K(Br_2^-)$, O^{2-} and Eu^{2+} after low temperature X-irradiation [15].

laxed excited states below the conduction band. The thermal activation energy was determined to be 37 meV for $F(Br^-)$ and 1.3 meV for $F(F^-)$ [43].

This simple pair model for the PSL mechanism was questioned by several authors. The EPR signal of Eu^{2+} did not change upon prolonged X-irradiation [32], nor could a change be observed in the Eu^{2+} luminescence [44]. Furthermore, the observation of an almost temperature independent PSL effect by stimulating $F(Br^-)$ centres from 4.2 K to RT [23] contradicts the model that electrons move through the conduction band upon photostimulation of F centres.

However, it has been proposed on the basis of several different experimental findings that the recombination between electrons and holes takes place via tunnelling and that a kind of "aggregate" between F centres, hole trap centres and the activator Eu^{2+} must be formed during X-irradiation (called triple aggregate centres [32]). It was found that the decay of the photostimulated luminescence under continued stimulation is temperature independent [45] and that the increase in the PSL intensity is proportional to the X-ray dose [23]. This latter result implies that retrapping of electrons after photostimulation does not occur, which makes electron-hole recombination via tunnelling more likely than via the conduction band. Tunnelling, however, requires a spatial correlation between the F centre and the activator. Direct evidence for a spatial correlation between F centres, O_F^- centres and Eu^{2+} was given with cross-relaxation spectroscopy using magneto-optical techniques (figure 3.4) [46].

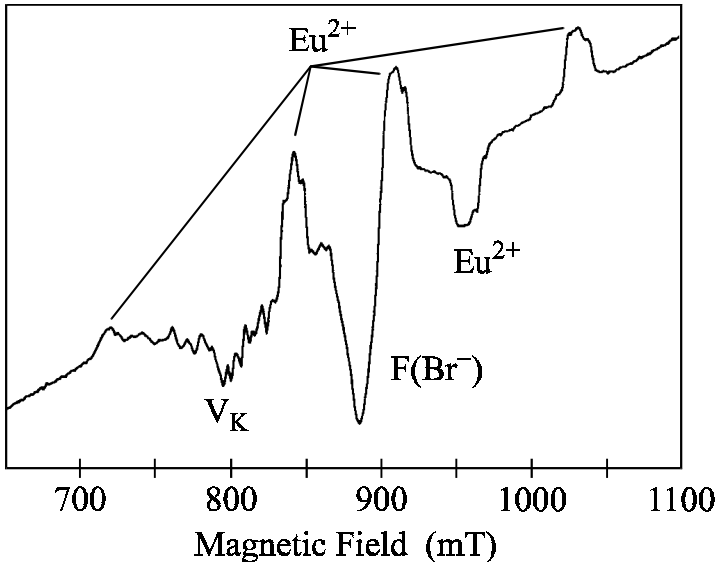

Figure 3.5 EPR spectrum detected in the MCDA band of the $V_K(Br_2^-)$ centre in BaFBr after X-irradiation at 4.2 K, recorded for **B** || **c** at T = 1.5 K applying a microwave frequency of 24 GHz. The spectrum shows cross-relaxations to the $F(Br^-)$ centre and to Eu^{2+} [46].

It could be shown by the cross-relaxation spectroscopy within the MCDA-detected EPR spectroscopy (see section 1.1.3) that there is a spatial correlation between F centres and Eu^{2+} as well as between O_F^- and Eu^{2+} after X-irradiation at RT. When X-irradiating at low temperature, V_K centres also show this correlation with the other centres [40, 46]. This leads to the speculation that an exciton decay occurs at the Eu^{2+} activator forming electron and hole trap centres and that there is a spatial correlation between the O_F^{2-}-anion vacancy pairs and the Eu^{2+} activators generated during the production of the material (figure 3.5).

Indirect evidence for the formation of "triple aggregate" centres was also found in the so-called replenishment effect. When the phosphor is stimulated at 4.2 K and the PSL exhausted, it can be replenished by annealing to temperatures above 200 K [32]. It seems that after exhaustion of the aggregates formed first, new aggregates can be formed by thermally activated motion of either hole trap or electron trap centres, or both. The size of the effect depends on the amount of oxygen contamination. The migration of $F(Br^-)$ centres was recently investigated at RT by [47]. An investigation of the crystal size dependence on the $F(Br^-)$ centre stability yielded that in small crystallites the $F(Br^-)$ centres seem to migrate to be stabilised near the surface of the crystal-

lites, whereas in larger crystals they only migrate to recombine with the hole trap centres.

The role of O_F^{2-} centres is certainly that it captures holes and forms O_F^- centres. The question is, though, whether it is also the hole trap centre active in the PSL process. When bleaching into the F centre band, the number of F centres can be drastically decreased to practically zero, while that of the O_F^- centres is hardly affected: The decrease is at most by 20%-30% [15]. Hence, it is not very likely that the O_F^- centres are those active hole trap centres in the triple aggregates described above. On the other hand, it was found that the variation of the oxygen content influences the PSL intensity. A low oxygen content results in a low PSL intensity. Also, the stimulation energy needed for the read-out process is higher for oxygen-poor BaFBr. Thus, it seems that oxygen is involved in two ways in the PSL mechanism: It provides vacancies for the F(Br^-) generation and it somehow seems to influence favourably the photostimulation of the triple aggregate centres in that less stimulation energy is needed for read-out and a high PSL intensity results after short stimulation.

3.2 Non-stoichiometric BaFBr

In the previous section it was shown that BaFBr powders which are normally formed by firing intimate mixtures of BaF_2 and $BaBr_2$ are always contaminated with oxygen. The role of the oxygen contamination is both beneficial and detrimental, and it is difficult to control its concentration such as to optimise the performance of these storage phosphors. There is a different method to produce BaFBr powders [22]. An intimate mixture of BaF_2 and NH_4Br in the ratio of 1:1 is fired instead of a mixture of BaF_2 and $BaBr_2$. When doped with Eu^{2+} the resulting material was found to be an excellent storage phosphor, although this material showed some properties significantly different from that produced by firing a mixture of BaF_2 and $BaBr_2$.

Chemical analysis of the material yielded that it is non-stoichiometric with a fluorine excess of about 10%±2% [48]. The non-stoichiometric $BaF_{1.1}Br_{0.9}$ still has the matlockite structure as does the stoichiometric BaFBr including that no change of the lattice parameters could be detected by detailed X-ray diffraction (XRD) studies [48]. It was also shown by XRD that $BaF_{1.1}Br_{0.9}$ is a single phase compound with at most 1% of other phases present. Attempts to vary the non-stoichiometry by firing different mixtures of BaF_2 and NH_4Br failed to generate a single phase material.

No oxygen luminescence [49, 50] could be excited in $BaF_{1.1}Br_{0.9}$ [51, 52]. Thus, this non-stoichiometric material is considered to be oxygen-free. X-irradiation at RT generates $F(Br^-)$ and $F(F^-)$ centres. The presence of $F(Br^-)$ centres could be measured by powder-EPR, while the concentration of $F(F^-)$ centres was not sufficient to be seen in the powder-EPR spectrum. The presence of F centres, however, can also be tested by exciting their infrared (IR) luminescence. Surprisingly, the IR luminescence peaking at 1.14 eV (1088 nm) of $F(F^-)$ could be detected, while that of $F(Br^-)$ centres at 0.92 eV (1348 nm) could not be detected [51]. This latter result points to a possible nearby presence of another defect which may cause the excited state of the $F(Br^-)$ centre to decay non-radiatively.

The question arises by what mechanism the $F(Br^-)$ centres are generated. Since there is no O_F^{2-} in this material, either Br^- vacancies must be present or a process such as the exciton decay resulting in F-H-centre pairs as is known from the alkali halides, may be operative [30]. It could be argued that the F^- excess in $BaF_{1.1}Br_{0.9}$ could cause the incorporation of Br^- vacancies. If 18% Br^- vacancies and 9% Ba^{2+} vacancies were present (the latter for charge compensation, the concentrations of Br^- and Ba^{2+} vacancies would explain the formula $BaF_{1.1}Br_{0.9}$), then there should be a significant change of more than 10% in the density which is caused by a decrease of the molecular mass while assuming no change of volume. This was, however, not measured within experimental error of ±2% [22].

Consequently, speculations arose that perhaps the F^- excess was incorporated as F^- on Br^- sites, i.e. as F^- antisites. The density change would then be as small as found within the experimental error of ±2%. The presence of F^- antisites could be established by NMR experiments. In order to obtain NMR lines narrow enough to resolve a possibly small chemical shift between ^{19}F on a regular lattice site and an F^- on a Br^- lattice site, magic angle spinning nuclear magnetic resonance (MAS-NMR) spectroscopy [13] was applied. It was shown (see section 3.2.2) that indeed F^- antisites are present in non-stoichiometric $BaF_{1.1}Br_{0.9}$ [52].

The question still remained whether the F^- antisites provide a mechanism whereby $F(Br^-)$ centres can be created or whether, in addition to the F^- antisites, Br^- vacancies are present in the material. This question is answered in the following section on EPR experiments after X-irradiation at low temperature and at RT. Both assumptions are correct: There are Br^- vacancies in the material, and there is a mechanism generating $F(Br^-)$ centres which originates in the F^- antisites.

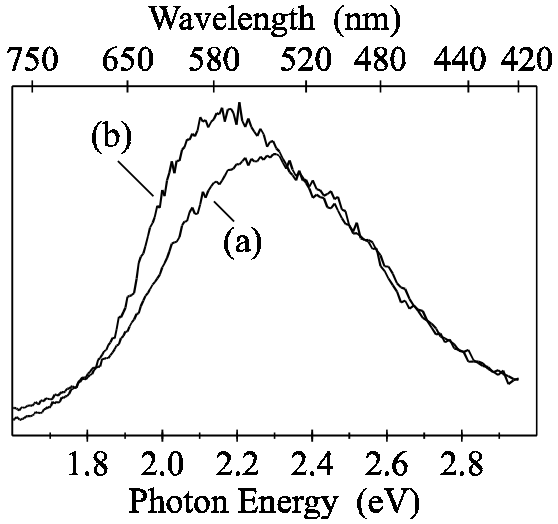

Figure 3.6 PSL excitation spectra measured at RT of (a) stoichiometric BaFBr:Eu^{2+} powder and (b) non-stoichiometric $BaF_{1.1}Br_{0.9}$:Eu^{2+} powder after X-irradiation at RT [52].

3.2.1 Photostimulated luminescence

The PSL excitation spectra of stoichiometric BaFBr:Eu and of non-stoichiometric $BaF_{1.1}Br_{0.9}$:Eu powder yielded that the peak of the stoichiometric sample is at 540 nm (figure 3.6a) while that of the non-stoichiometric one is at 580 nm, i.e. at lower photon energy, and there is an additional shoulder at 510 nm (figure 3.6b). The intensity ratio between the 580 nm peak and the high-energy shoulder at 510 nm is approximately 2:1. In both materials the luminescence is due to the stimulation of F(Br$^-$) and F(F$^-$) centres. The absorption peak of F(Br$^-$) centres is at 580 nm for the electrical light vector perpendicular to the crystal *c*-axis, while it is at 510 nm for $\mathbf{E} \| \mathbf{c}$. For F(F$^-$) centres the absorption peaks are at 470 nm for $\mathbf{E} \perp \mathbf{c}$ and at 520 nm for $\mathbf{E} \| \mathbf{c}$ [34]. It is seen qualitatively in figure 3.6, that fluorine excess leads to an enhanced concentration of F(Br$^-$) centres [51]. The absorption peaks of F(Br$^-$) centres agree well with the peak and shoulder of figure 3.6b. The intensity ratio of 2:1 is caused by the statistical distribution of the parallel and perpendicular crystallite orientations with respect to the electrical light vector. Apparently in the non-stoichiometric BaFBr very few F(F$^-$) centres are generated in comparison to F(Br$^-$) centres.

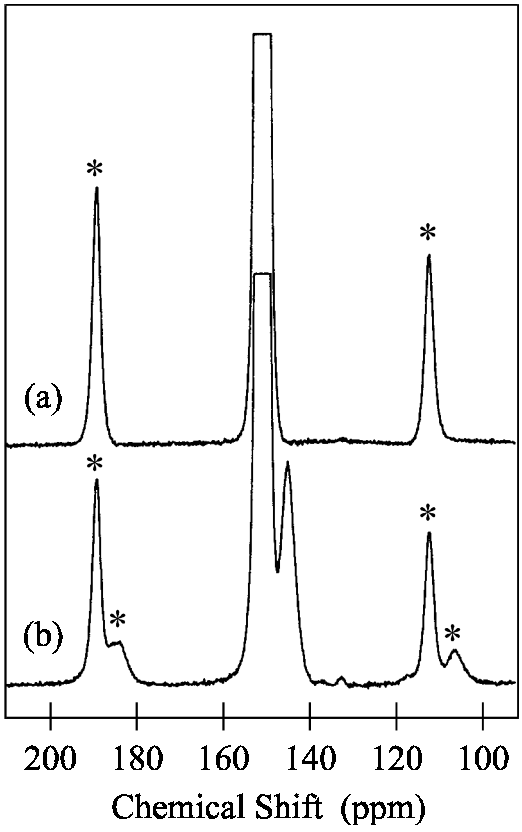

Figure 3.7 ^{19}F MAS-NMR spectra of (a) a crushed stoichiometric BaFBr single crystal and (b) non-stoichiometric $BaF_{1.1}Br_{0.9}$ powder. The spinning side bands are marked with asterisks [52].

3.2.2 Identification of fluorine antisites with MAS-NMR

Figure 3.7 shows the MAS-NMR spectra of ^{19}F of a pulverised stoichiometric single crystal of BaFBr and of non-stoichiometric $BaF_{1.1}Br_{0.9}$ powder. The peaks due to the lattice ^{19}F nuclei of both spectra coincide within experimental error at 150.9 ppm. A new line appears in $BaF_{1.1}Br_{0.9}$ powder at lower frequency, at 145.3 ppm, which also shows up in the spinning side bands (marked with asterisks in figure 3.7). The intensity of the new line as measured by the area in comparison to that of the lattice ^{19}F is 7.3%. The addition of the contributions of the spinning side bands yields in total 8.6% intensity. Thus, the new line shifted by almost 6 ppm to lower frequencies is due to approximately 9% of ^{19}F nuclei with a different site compared to the lattice nuclei. This is close to the 10% excess of F in the lattice determined by chemical analysis [48]. Since for

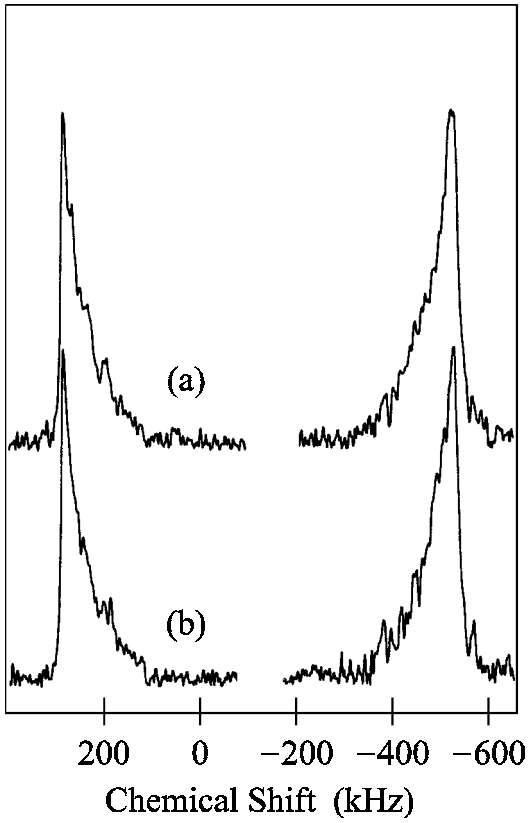

Figure 3.8 Edge singularities for ^{137}Ba of (a) a crushed stoichiometric BaFBr single crystal and (b) non-stoichiometric BaF Br powder [52].

electrostatic reasons it is very unlikely that the new site is an interstitial site, the new line was assigned to F^- on Br^- vacant sites, i.e. to F^- antisites [52].

Figure 3.8 shows the high and low frequency edge singularities of the ^{137}Ba static powder spectrum having second order quadrupole interaction [53]. The edge singularities of Ba as well as those of Br (which are not shown here) are identical for both the stoichiometric and the non-stoichiometric BaFBr. Thus, the F^- excess does not change the crystal structure, i.e. the geometry must be practically identical for both crystals.

The MAS-NMR spectra confirm an earlier suggestion that the F^- to Br^- ratio of about 1.1 to 0.9 is achieved by 10% enhanced fluorine incorporation and a simultaneous 10% bromine reduction [51]. In this case a charge compensation on the cationic sublattice is not necessary. The change in density is approximately 2% which could not be observed experimentally within experimental error of ±2% [22].

The two chemical shifts found for ^{19}F for the regular F lattice site and the antisite ^{19}F are not very different: 150.9 ppm for the regular sites, 145.3 ppm for the antisites. The difference of 5.6 ppm is smaller than that found for ^{19}F in the divalent fluorides CaF_2, SrF_2 and BaF_2 (see e.g. [54, 55]) which vary between 58 ppm and 152 ppm, respectively. It is interesting to note that the Ba^{2+}-F^- distance in BaF_2 (2.68 Å) is almost identical to that in BaFBr (2.66 Å). In [54] it was argued that the chemical shift is determined by the metal-F^- distance. The 150.9 ppm found for the regular ^{19}F lattice nuclei tie in well with this rule. Not so the ^{19}F antisites having a distance of 3.36 Å to the nearest Ba^{2+} neighbour (along the *c*-axis) and 3.42 Å to the four next nearest Ba^{2+} neighbours, respectively. Perhaps the larger screening is the result of a larger site for F^- and the more expanded electron core.

3.2.3 Identification of electron and hole trap centres with EPR

After X-irradiation at RT the EPR spectrum of non-stoichiometric $BaF_{1.1}Br_{0.9}$ powder shows the lines of $F(Br^-)$ centres and a powder-EPR line the *g* factor of which indicates that it is caused by a hole trap centre (figure 3.9b). The spectrum can be simulated well by assuming an axial centre with the *g* values of $g_\perp = 2.02$ and $g_\parallel = 2.002$ [52]. In figure 3.9a the powder-EPR spectrum of stoichiometric BaFBr is shown which contains oxygen and where the resonances of O_F^- centres as well as of $F(Br^-)$ centres are seen. The positive shift of the *g* values of the new centre indicates that it is indeed a hole trap centre.

Its nature as a hole trap centre is further supported by the observation that its intensity increases proportional to the X-ray dose as does that of the $F(Br^-)$ centres. The simultaneous growth of the hole trap centre and that of the $F(Br^-)$ centre suggests that the hole trap centre is the “anticentre” of the $F(Br^-)$ centre, i.e. electron-hole separation results in the $F(Br^-)$-hole trap centre pairs. When exciting the $F(Br^-)$ band with light, a simultaneous destruction of $F(Br^-)$ and the hole trap centres is observed. All F centres disappear, while 30% of the hole trap centres remain. These observations support the view that F centres and hole trap centres are generated as pairs. The fact that not all hole trap centres are recombined with the electrons of the F centres can be explained by the formation of RT-stable F aggregate centres which occurs simultaneously when exciting in the F band at RT.

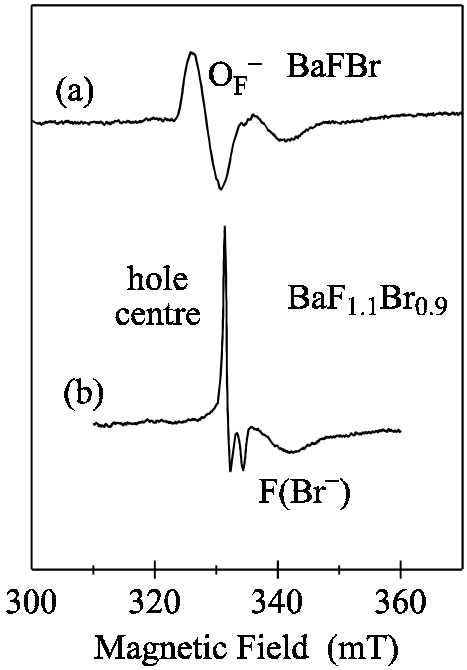

Figure 3.9 Powder EPR spectra of (a) stoichiometric and (b) non-stoichiometric BaFBr powder after X-irradiation at RT, recorded at 10 K applying a microwave frequency of 9.335 GHz [52].

After X-irradiation of stoichiometric BaFBr powder at temperatures below 77 K intense resonances lines of the $V_K(Br_2^-)$ centres and a weak EPR signal of the $F(Br^-)$ centres were observed [52]. After annealing up to 300 K, the $V_K(Br_2^-)$ centre lines disappear whereas the O_F^- centre line appears. The $V_K(Br_2^-)$ centre decays at about 120 K [32]. The moving hole is trapped by an O_F^{2-} impurity to form the O_F^- centre [56].

After X-irradiation at temperatures below 77 K the EPR spectrum of the non-stoichiometric BaFBr powder showed again intense resonance lines of the $V_K(Br_2^-)$ centres and a weak signal of the $F(Br^-)$ centres as well as the powder EPR line of the new hole trap centre described above. When using a low X-ray dose a rather strong signal of the V_K centres appears relative to that of the new hole trap centre. Upon increasing the X-ray dose the signal of the new hole trap centre increases rapidly while that of the V_K centre grows at a slower rate. The experiments were not carried as far as reaching a saturation of the V_K centre signal, but it appears that such a saturation can be reached while no sign of an incipient saturation was observed for the new hole trap centre [52].

After annealing up to 300 K the $V_K(Br_2^-)$ centre EPR lines have disappeared. This thermal decay of the $V_K(Br_2^-)$ centre did not cause a change in the EPR line intensity

of the new hole trap centre, but part of the F centre signal was destroyed. Unfortunately, the S/N ratio of the F centre was not good enough, in order to check whether as many F centres were destroyed as V_K centres have disappeared.

3.2.4 Generation of electron and hole trap centres

The generation of F centres in non-stoichiometric $BaF_{1.1}Br_{0.9}$ powders seems to occur via two mechanisms. At 77 K two kinds of hole trap centres were observed: $V_K(Br_2^-)$ centres and the new hole centres, which are considered to be H centres in the F^- sublattice (see below). The $V_K(Br_2^-)$ centre generation at 77 K seems to indicate that in spite of no oxygen contamination the non-stoichiometric BaFBr contains also Br^- vacancies. Upon annealing to RT the $V_K(Br_2^-)$ centres and part of the $F(Br^-)$ centres disappear: Mobile $V_K(Br_2^-)$ centres recombine with $F(Br^-)$ centres. However, some $F(Br^-)$ centres remain and so does the EPR signal of the new hole trap centre, which is not changed at all upon the availability of mobile $V_K(Br_2^-)$ centres.

Since $F(Br^-)$ centres and the new hole trap centre are electron and hole trap centres created simultaneously and proportional to each other, it is suggested that F^- antisites (F_{Br}^-) are the origin of the $F(Br^-)$ centres and the new hole trap centre according to the reaction

$$F_{Br}^- \xrightarrow{\text{X-ray}} F(Br^-) + F_{2,F}^- \tag{3.2}$$

i.e. an $F(Br^-)$ and an F_2^- molecular centre in the F^- sublattice ($F_{2,F}^-$) are created in an F-H-process where the electron trap centre (F centre) is formed in the Br^- sublattice and the H centre is formed in the F^- sublattice. To support this suggestion, the powder EPR spectra of the new H centre was analysed in more detail. It is known that F_2^- molecular centres on F^- sites can be produced in alkali earth fluorides by X-irradiation below 77 K [57]. There, the two fluorine nuclei of the H-type centre are not equivalent, i.e. one fluorine nucleus is placed on an interstitial site (“fluorine interstitial”) whereas the second one is on a regular lattice site (“fluorine substitutional”). The hyperfine (hf) interactions of the fluorine interstitial and the fluorine substitutional are different.

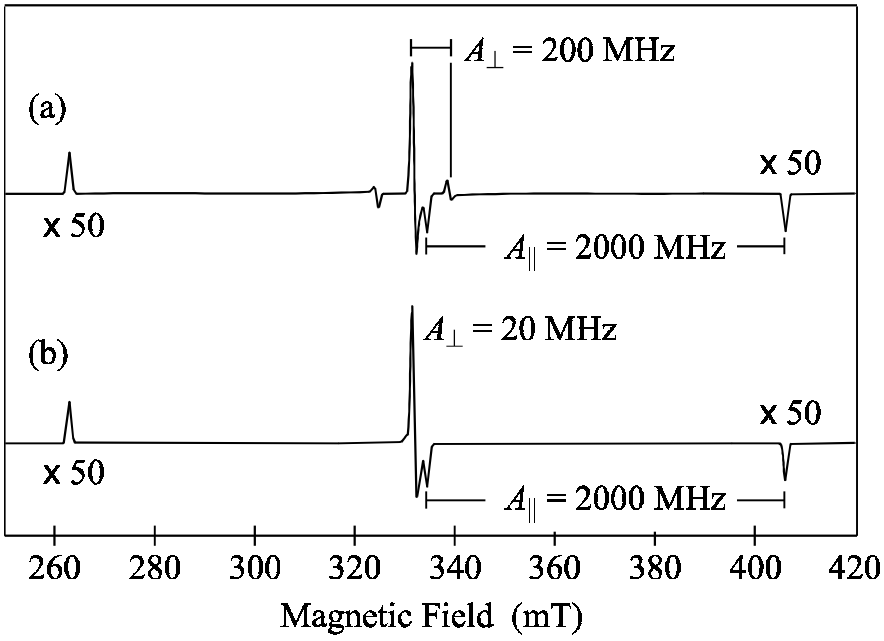

Figure 3.10 Calculated powder EPR spectra of a F_2^- centre with two equivalent fluorine nuclei. The *g* tensors with $g_\perp = 2.02$ and $g_\parallel = 2.002$ are axial as well as the ^{19}F hyperfine tensors. The bars indicate the corresponding hyperfine splittings. The microwave frequency is 9.335 GHz [52].

Figure 3.10 shows two calculated powder EPR spectra of an F_2^- centre with two equivalent fluorine nuclei. Hereby typical fluorine hf interaction values [57] of $A_\perp$ = 200 MHz and $A_\parallel$ = 2000 MHz or $A_\perp$ = 20 MHz and $A_\parallel$ = 2000 MHz, respectively, were assumed. In both cases the powder EPR lines indicating the hf interaction for an orientation parallel to the molecular axis are very weak. In figure 3.10 the lines are scaled up by a factor of 50. The powder EPR lines indicating the hf interaction perpendicular to the molecular axis are clearly visible in figure 3.10a. Assuming a small value for $A_\perp$ (= 20 MHz), the hf lines are superimposed by the central lines (figure 3.10b). Thus, by comparison with figure 3.9b, it was proposed that the hole trap centre has $A_\perp \leq 20$ MHz [52].

Figure 3.11 shows a model of the F_2^- centre in BaFBr with two equivalent fluorine nuclei. The molecular axis of the F_2^- centre with the two equivalent fluorine nuclei is parallel to the *a*-axis (*b*-axis) of the crystal as calculated in [58]. Since a powder EPR spectrum is a summation over all possible orientations of the magnetic field vector, the information about the orientation of the interaction tensors to the crystal axes is lost.

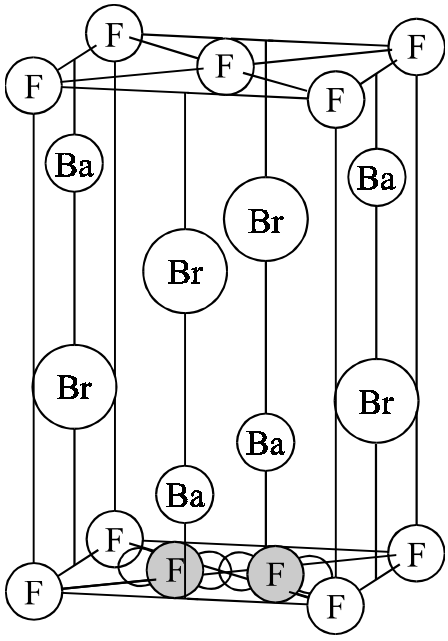

Figure 3.11 Model of an H-type F_2^- centre in BaFBr with two equivalent fluorine nuclei after [58].

Therefore, the measured powder EPR spectrum of the new hole trap centre does not allow to decide on the position of the molecular axis.

A qualitative view of the F-H process would be that the valence electron of the F^- antisite is excited upon an exciton decay at the F_{Br}^- antisite into a diffuse excited state and that the F^0 becomes mobile and moves to the F^- sublattice, where it associates itself with a lattice F^- to form the H (F_2^-) centre on a fluorine site (figure 3.12). It was calculated by Baetzold [58] that such an H centre is stable and also that the formation of F_{Br}^- antisites is exothermic in BaFBr [59]. It was not possible to say whether the F(Br^-) and H centres are nearest neighbours or further apart. Judging from the results obtained in the alkali halides, they will be further apart, otherwise they would probably recombine [60].

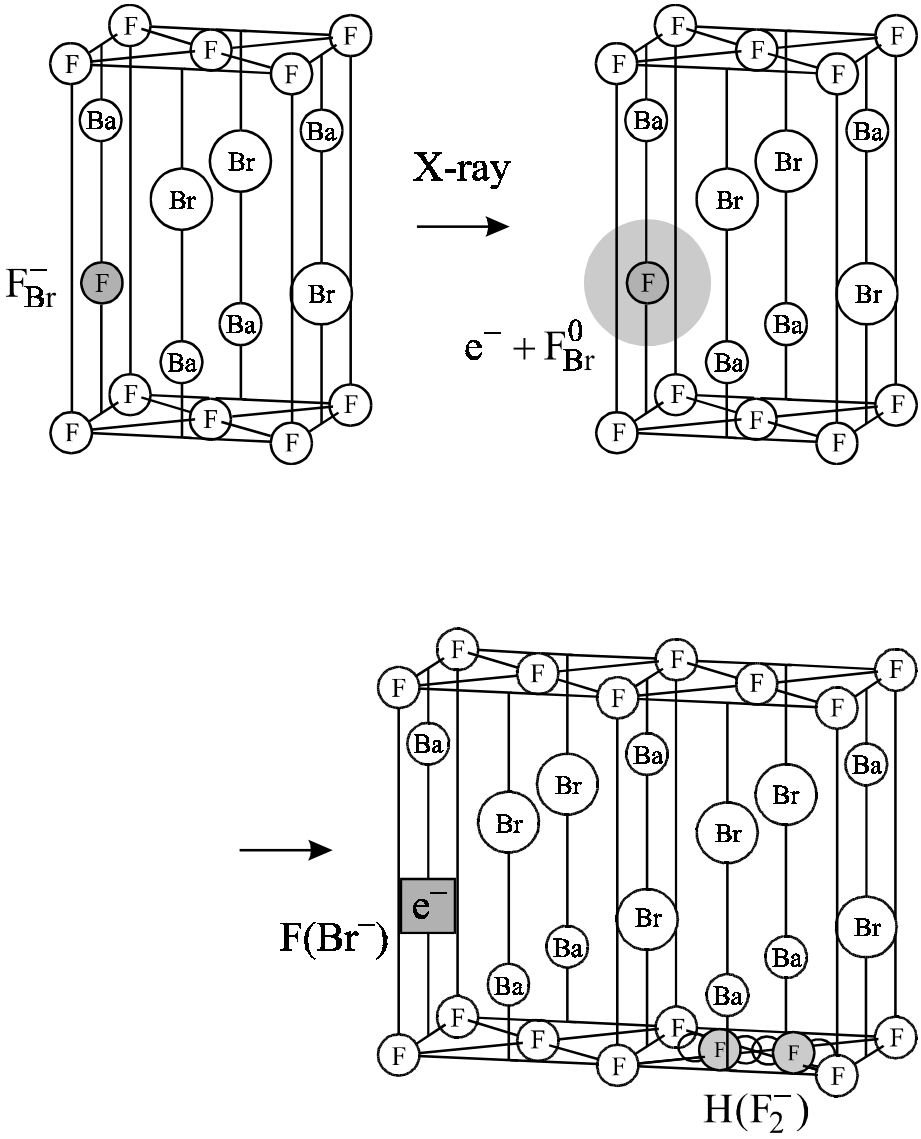

Figure 3.12 Schematic presentation for the F-H centre generation process in non-stoichiometric BaFBr [5].

To be stable at RT it is important for the hole trap centre to avoid recombination with the F centre. It seems reasonable to argue that the hole can move away more easily from the F centre in the F^{-} sublattice than in the Br^{-} sublattice. This is because the F^{-}-F^{-} distance is much shorter (3.18 Å) than the Br^{-}-Br^{-} distance, either in plane (4.50 Å) or out of plane (3.72 Å). Also there are linear [110] or [100] chains of equivalent F^{-} ions, whereas the hole motion within the Br^{-} double layer would need to proceed in a zigzag motion to separate from the F centre. The former pathway resembles more the situation

in the alkali halides, where the hole motion is known to proceed along the [110] halogen chain.

The experiments have shown that the V_K centre production seems to saturate upon increasing the X-ray dose, while that of the H centre production showed no sign of saturation [52]. The maximum number of V_K centres depends on the number of Br^- vacancies present, which cannot be excessively large, as otherwise a significant change of the density would have been observed. Although it was not possible to determine the number of V_K centres quantitatively from the powder spectra, it will be of the order of $10^{16}\,cm^{-3}$ and that should be the order of magnitude of the Br^- vacancies present. On the other hand, F^- antisite defects are "abundant" (10%) in comparison. Thus, no saturation in H centre production is expected in line with this model. The decay of the $V_K(Br_2^-)$ centres did not influence the EPR line intensity of the new hole trap centre. Had the moving holes of the decaying $V_K(Br_2^-)$ centres been trapped by F^- interstitials, the EPR signal of $H(F_2^-)$ hole trap centres would have been enhanced. This was not the case. Therefore, it was suggested that the $F(Br^-)$ centre production in non-stoichiometric BaFBr and the simultaneous generation of the F_2^- hole trap centre is caused by F^- antisites and not by F^- interstitials.

3.3 Red-shift of the PSL excitation upon Ca^{2+} or Sr^{2+} doping

For practical use, apart from a high sensitivity, i.e. a high conversion efficiency of X-rays into photostimulable defects, it is desirable that the phosphors can be stimulated with low laser light intensity, particularly in the infrared spectral region. It was shown that the PSL excitation of BaFBr doped with Eu^{2+} can be made sensitive to stimulation further into the infrared by additional Ca^{2+} or Sr^{2+} doping [51, 61].

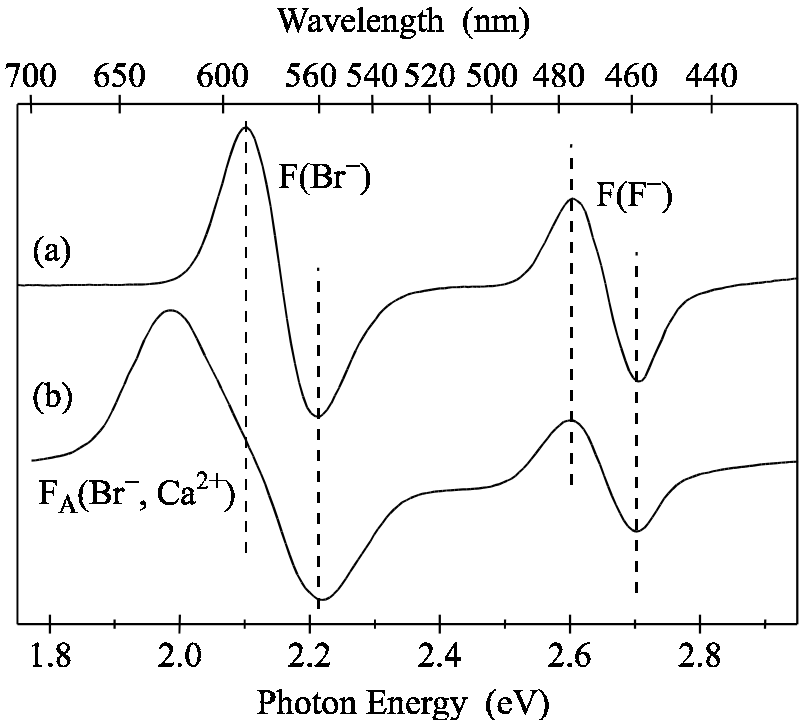

Figure 3.13 MCDA spectra of F(Br$^-$), F(F$^-$), and F_A(Br$^-$, Ca^{2+}) centres in (a) undoped BaFBr and (b) $Ba_{0.98}Ca_{0.02}FBr$ after X-irradiation at RT, recorded for **B** || **c** at 1.5 K [61].

After X-irradiation at RT the MCDA of BaFBr, recorded for **B** || **c**, shows two derivative-like structured bands due to the two possible F centres (F(Br$^-$) and F(F$^-$) centre) (figure 3.13a) [34]. The centres of these bands, where the MCDA changes sign, are at 2.15 eV and 2.65 eV, respectively. In Ca^{2+} doped BaFBr these two F centres are also observed after X-irradiation at RT (figure 3.13b). The shape and spectral position of the MCDA band of the F(F$^-$) centre remain the same as in undoped BaFBr, whereas in the case of the F(Br$^-$) centre the spectrum shows a superposition of at least two bands. The minimum of the perturbed F(Br$^-$) centre band keeps its position while the maximum shifts to lower energies. The perturbed F(Br$^-$) centre is supposed to be a F centre where a Ba^{2+} ion in a nearest-neighbour position is replaced by a Ca^{2+} ion, in analogy to what was observed for F centres in alkali halides [62]. The MCDA bands observed in Ca^{2+} doped BaFBr are thus a superposition of the MCDA band of the unperturbed F(Br$^-$) centre and of that of the perturbed F_A(Br$^-$, Ca^{2+}) centre.

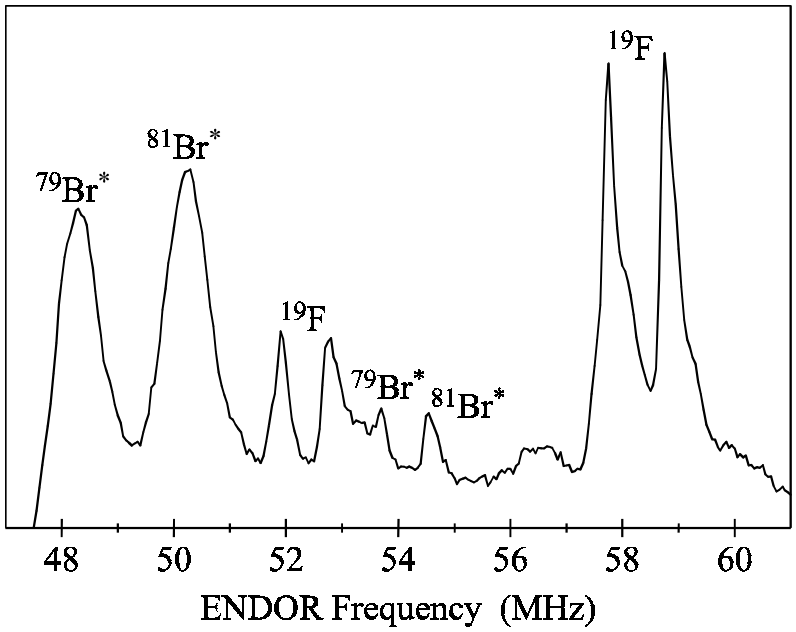

Figure 3.14 MCDA-detected ENDOR spectra of $F(Br^-)$ and $F_A(Br^-, Ca^{2+})$ centres in Ca^{2+} doped BaFBr after X-irradiation at RT, **B** || **c**, $B = 871$ mT, recorded at a photon energy of 1.984 eV and at 1.5 K applying a microwave frequency of 24 GHz. The lines marked by asterisks are from $F_A(Br^-, Ca^{2+})$ centres [61].

MCDA-detected ENDOR measurements performed on the perturbed $F(Br^-)$ centre band yielded that there are resonances due to the unperturbed $F(Br^-)$ centre as well as those of the $F_A(Br^-, Ca^{2+})$ centre (figure 3.14). The two ENDOR lines marked with ^{19}F at about 52 MHz are due to the nearest-neighbouring fluorine nuclei of the unperturbed $F(Br^-)$ centre in BaFBr [34]. The two peaks marked with $^{19}F^*$ at about 58 MHz cannot be explained with the shf interactions of neighbouring nuclei of the unperturbed $F(Br^-)$ centre. Thus, they must be due to the $F_A(Br^-, Ca^{2+})$ centre. A field shift experiment where the shift in the frequency of the ENDOR lines due to the nuclear Zeeman interaction was measured with respect to the variation of the external magnetic field, showed that the lines at 58 MHz originate from fluorine nuclei (for details of the field shift method see e.g. [10]). In analogy with the ENDOR lines of the unperturbed $F(Br^-)$ centre these signals were assigned to the nearest fluorine neighbours of the $F_A(Br^-, Ca^{2+})$ centre. This assignment was confirmed by the ENDOR analysis of the conventional ENDOR measurements. The splitting of the ^{19}F and the $^{19}F^*$ lines for the magnetic field parallel to the *c*-axis is caused by a slight misorientation of the crystal. The other four ENDOR lines are caused by the nearest-neighbouring bromine nuclei of the $F_A(Br^-,$

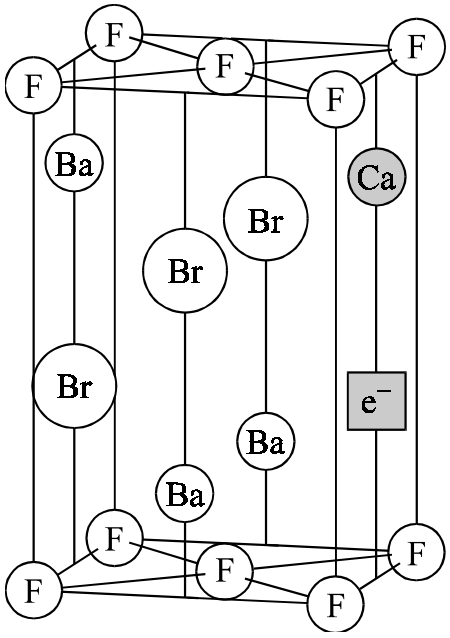

Figure 3.15 Defect model of the $F_A(Br^-, Ca^{2+})$ centre in Ca^{2+} doped BaFBr. One Ca^{2+} replaces either the upper or the lower Ba^{2+} along the *c*-axis [61].

Ca^{2+}) centre. For the magnetic field exactly parallel to the *c*-axis the ^{19}F ENDOR lines of the $F(Br^-)$ centre coincide, so do the $^{19}F^*$ lines for the $F_A(Br^-, Ca^{2+})$ centre which shows that the four ions of the first fluorine shell are magnetically equivalent. Therefore, the perturbing Ca^{2+} ion must be located on the fourfold axis of the $F_A(Br^-, Ca^{2+})$ centre (figure 3.15). A more detailed investigation of the symmetry of the Ca^{2+} perturbed $F(Br^-)$ centre was made with conventional ENDOR measurements [61].

A rough estimate of the relative concentrations of the $F_A(Br^-, Ca^{2+})$ and the $F(Br^-)$ centre created with X-irradiation at RT can be made, assuming that the ENDOR effect of the nearest fluorine lines is not much different for both defects. The ratio of the $F_A(Br^-, Ca^{2+})$ centre to $F(Br^-)$ centre is approximately 3:1, i.e. 75% of F centres are F_A centres. It seems that the exciton decay mechanism producing F centres upon X-irradiation occurs preferentially at the Ca^{2+} perturbed sites. Otherwise it would not have been possible to observe such a large ratio between F_A and F centres which deviates from pure statistical probability according to the doping by almost two orders of magnitude.

The observed red-shift of the F_A centre absorption band can be explained by a shallower Madelung potential well binding the electron of the F centre. The smaller Ca^{2+} ion (ionic radius 0.99 Å) replacing the larger Ba^{2+} ion (ionic radius 1.34 Å) along the *c*-axis

may be relaxed away from the Br^- vacancy leaving a larger space for the F centre electron. According to the Mollwo-Ivey relation the peak energy of the F centre absorption band is proportional to $1/d^2$ where d is the lattice constant [62]. The lattice constant will be increased along the c-axis resulting in a red-shift of the optical absorption band. However, it is not possible to decide which of the two Ba^{2+} ions along the c-axis is replaced by Ca^{2+}. It seems highly improbable that both are substituted by Ca^{2+}.

3.4 Surrounding of the activator Eu^{2+}

It is reasonable to assume that Eu^{2+} substitutes for Ba^{2+} in BaFBr. An EPR investigation [63] yielded an axial centre with the z-axes of the fine structure and hf tensors of Eu^{2+} along the c-axis as expected for such a site [63]. What could not be inferred from EPR was whether or not there are lattice relaxations about the Eu^{2+}. The ionic radius of the replaced Ba^{2+} is 0.134 nm, that of Eu^{2+} 0.109 nm, i.e. about 20% smaller. Therefore, a substantial lattice relaxation about Eu^{2+}, or a non-central position of Eu^{2+}, can be anticipated. This is of interest since a lattice relaxation could in principle be an explanation for the observation that upon X-irradiation, electron and hole trap centres are created with a spatial correlation to the activator Eu^{2+}, an important feature for the functioning of BaFBr:Eu^{2+} as a storage phosphor. Information about this question could be obtained from an ENDOR investigation, in which the shf interaction tensors with the lattice neighbours are determined [64].

3.4.1 EPR and ENDOR of crystalline BaFBr:Eu^{2+}

The EPR spectrum of Eu^{2+} in BaFBr consists of seven fine-structure groups each having a hf splitting of 12 lines. Eu^{2+} has an $S = 7/2$ ground state and two stable isotopes: ^{151}Eu with $I = 5/2$ and 47.82% abundance and ^{153}Eu with $I = 5/2$ and 52.18% abundance. Each Eu isotope thus has a hf structure of 6 lines; since the two nuclear g factors differ significantly so do the hf interactions ($g_n(^{151}\text{Eu}) = 1.389$, $g_n(^{153}\text{Eu}) = 0.6134$), and consequently the two sextets are clearly resolved [63].

Figure 3.16 shows a ENDOR spectrum of $^{151}Eu^{2+}$ measured in the m_S transition $-1/2 \leftrightarrow +1/2$ for a orientation of the magnetic field parallel to the crystal c-axis. Besides the two lines of ^{151}Eu at 4.1 and 20.3 MHz there are several intense lines due to ^{19}F. Around the Larmor frequency of ^{19}F at 13.2 MHz there are lines at 11.8 MHz and

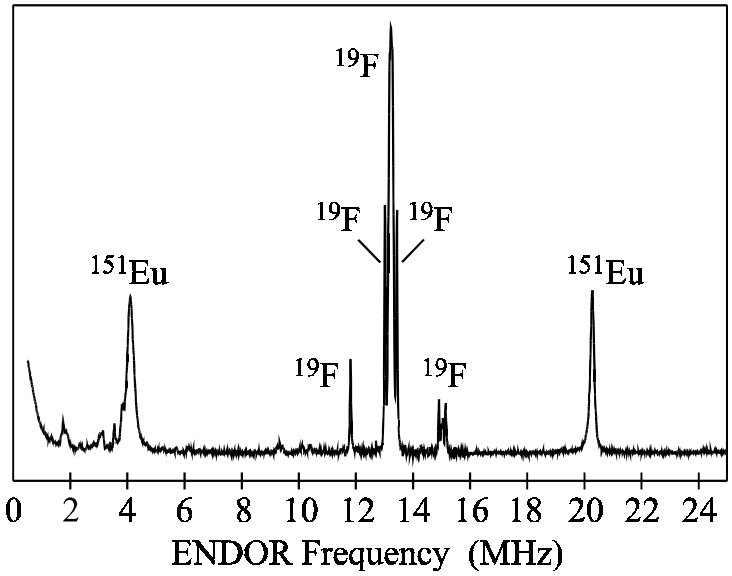

Figure 3.16 ENDOR spectrum of Eu^{2+} in crystalline BaFBr for **B** || **c**, $B = 331.1$ mT (m_S transition $-1/2 \leftrightarrow +1/2$), $T = 20$ K and a microwave frequency of 9.345 GHz [64].

15.0 MHz from the nearest and at 13.0 MHz and 13.4 MHz from the next-nearest fluorine nuclei as was determined from their angular dependence. The low intensity lines at low frequency are probably due to ^{79}Br and ^{81}Br. They were not analysed. Ba lines were not seen, most likely due to their low abundance of magnetic isotopes ^{135}Ba (6.6%) and ^{137}Ba (11.3%) [64].

In figure 3.17 the fluorine nuclei the shf interaction of which with the Eu^{2+} activator were determined are shaded grey. The analysis of these fluorine shf interactions yielded that no significant shift of Eu^{2+} away from the regular Ba^{2+} position occurs [64].

3.4.2 EPR and ENDOR of powdered BaFBr:Eu^{2+}

EPR on powdered BaFBr doped with Eu^{2+} yielded resonances in a magnetic field range from 200-500 mT in X-band (9.235 GHz) [64]. The strongest lines are seen between 300 and 370 mT in agreement with the EPR angular dependence of a single crystal, where the intense line groups of the m_S transitions $-3/2 \leftrightarrow -1/2$, $-1/2 \leftrightarrow +1/2$ and $+1/2 \leftrightarrow +3/2$ occur. The spectrum is asymmetric with respect to its transition through zero at 340 mT. This is a consequence of the rather high fine structure interaction.

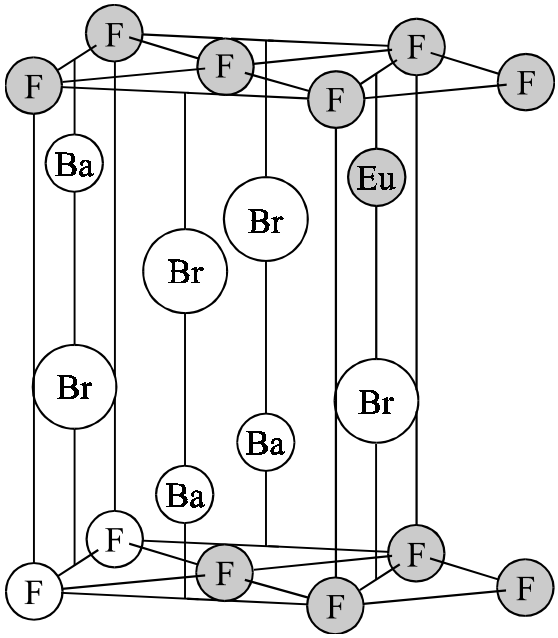

Figure 3.17 Centre model of the Eu^{2+} centre in BaFBr. The defect and its nearest fluorine neighbours the shf interactions of which were determined are shaded grey.

The powder-ENDOR spectrum measured at 331 mT is shown in figure 3.18. In order to identify the lines, magnetic field shift measurements were performed (see e.g., [10]). The powder spectrum is a superposition of many single spectra due to the different orientations of the crystalline axes with respect to the magnetic field. If the magnitude of the magnetic field is changed, the ENDOR lines are measured in single crystal EPR lines which belong to different magnetic field orientations, i.e. upon shifting the magnetic field the field orientation is changed indirectly. Here, because of the possibility of comparison with the single crystal spectra and their angular dependencies, the assignment of other lines can be made.

The broad intense line between 12.5 and 14 MHz is centred around the Larmor frequency of ^{19}F. The assignment of the ENDOR lines at 10.4 and 16.5 MHz, which belong to the nearest fluorine neighbours, was achieved by magnetic field shift measurements in the field range between 320 and 350 mT. Between 325 and 345 mT the lines are intense. Choosing magnetic field values outside this range, e.g. 320 or 350 mT, the lines decrease to about a third of the former intensity. The angular dependence of the single crystal EPR lines yielded that the EPR m_S transition $-1/2 \leftrightarrow +1/2$ is within the range of 325 to 345 mT for all orientations of the magnetic field. The angular depend-

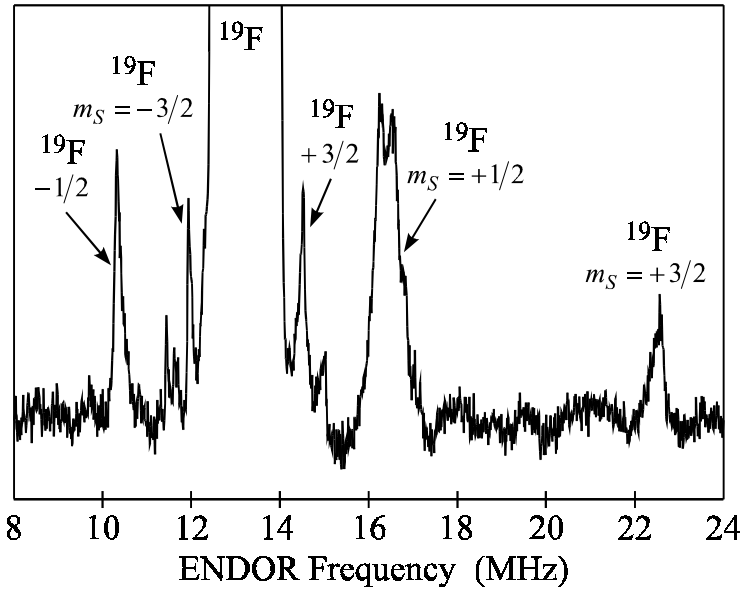

Figure 3.18 Powder ENDOR spectrum of Eu^{2+} in BaFBr for B = 331 mT, T = 20 K and a microwave frequency of 9.233 GHz. The ^{19}F lines of the nearest and the next-nearest fluorine neighbours as well as their m_S quantum numbers are identified. The frequency dependent background is subtracted [64].

ence of the ENDOR lines of the nearest fluorine neighbours belonging to this EPR transition have many lines per angle in the range of 10.4-16.5 MHz. Therefore, choosing the magnetic field within the range of 325 to 345 mT one induces the EPR m_S transition $-1/2 \leftrightarrow +1/2$ and thus the corresponding fluorine ENDOR lines. If the magnetic field is 320 mT or 350 mT, this EPR transition is not saturated, the corresponding fluorine lines do not contribute to the ENDOR spectrum. One can only see ENDOR lines belonging to the weaker contributions of the neighbouring fine-structure groups $-3/2 \leftrightarrow -1/2$ and $+1/2 \leftrightarrow +3/2$. In this way the assignment of the ENDOR lines presented in figure 3.18 was made. Even a small change in the local structure of Eu^{2+}, i.e. a change in the shf interaction parameters by only 10%, would have been seen in the corresponding powder ENDOR spectra by a significant shift of the powder ENDOR lines [64].

3.4.3 Influence of the production process

Another question is whether the local environment of Eu^{2+} is changed, depending on how the phosphor is produced. Stoichiometric or non-stoichiometric BaFBr powders

could, in principle, differ from the single crystal environment around Eu^{2+} due to the different production processes [52]. Since, in particular, it was interesting to study details about the local structure of Eu^{2+} in non-stoichiometric BaFBr, which can only be made as a powder, the above described investigations were performed: First, EPR and ENDOR of Eu^{2+} in crystalline BaFBr were measured and analysed. The single crystal was afterwards crushed to a powder, and the powder EPR as well as the powder-ENDOR spectrum were recorded and analysed using the single crystal data. Then, the powder-ENDOR spectra of Eu^{2+} in stoichiometric and in non-stoichiometric BaFBr powders, generated by means of a solid state reaction firing appropriate mixtures of fluorides and bromides [52], were measured. It turned out that no significant shift of Eu^{2+} away from the regular Ba^{2+} position occurs, and that the local properties of Eu^{2+} are identical within experimental error in all investigated samples.

Chapter 4

Alkali halides and elpasolites

One of the disadvantages of present X-ray storage phosphors is still the unsatisfactory spatial resolution of the X-ray images. The light scattering of the scanning laser beam during the read-out process is certainly one of the reasons for that. The BaFBr crystallites in the X-ray storage phosphor image plates are birefringent, a consequence of the matlockite structure. With respect to the light scattering it would be advantageous to replace the optically anisotropic BaFBr crystallites by optically isotropic crystals, e.g. cubic crystals. It is, therefore, a challenge to find cubic X-ray storage phosphors systems which have a similarly high performance as a standard BaFBr:Eu^{2+} phosphor

Storage phosphor	stimulation (nm)	CE ($pJ/mm^2/mR$)	SE ($\mu J/mm^2$)	CE/SE (arb. units)
BaFBr:Eu^{2+}	633[1)]	20.4	15.7	1300
	680[2)]	14.4	28	510
RbBr:In^+	680[2)]	1.9	25.0	77
RbBr:Ga^+	680[2)]	5.6	3.9	1470
CsBr:In^+	680[2)]	3.0	23.0	140
CsBr:Ga^+	680[2)]	5.4	4.3	1370

Table 4.1 Performance of some In^+ and Ga^+ doped alkali halide X-ray storage phosphors in comparison with a standard BaFBr:Eu^{2+} X-ray storage phosphor screen after [8]. [1)] HeNe-laser, [2)] laser diode.

screen. For special applications, in particular for non-destructive testing, systems can also be used where e.g. a longer radiative life time of the activator luminescence is not a hindrance, because the read-out time can be longer or the screen is smaller, i.e. less pixels have to be read out.

There are two cubic systems which have proved to have storage properties and which have been investigated very intensely (mostly by luminescence spectroscopy): Alkali halides doped with Ga^+, In^+ or Tl^+ (e.g. [65, 66]) and Ce^{3+} or Pr^{3+} doped elpasolites (e.g. [9]). In table 4.1 some of the best alternative systems to $BaFBr:Eu^{2+}$ are listed for which the conversion efficiency (CE) and the stimulation energy (SE) as well as the quantity CE/SE are given in comparison to a standard $BaFBr:Eu^{2+}$ screen. It is seen that the two alkali halides $RbBr:Ga^+$ and $CsBr:Ga^+$ have excellent figures of merit. In the following a short characterisation is presented for the X-ray storage phosphors $KBr:In^+$ and $RbI:Tl^+$, whereas $RbBr:Ga^+$ and $CsBr:Ga^+$ are described in more detail because of their importance. After that first results on Eu^{2+}-doped RbBr and CsBr are presented. Finally, the elpasolites $Cs_2NaYF_6:Ce^{3+}$ and $Cs_2NaYF_6:Pr^{3+}$ are briefly characterised.

4.1 $KBr:In^+$

$KBr:In^+$ has been shown to have storage and PSL properties [6]. Although from the practical point of view it will not be a very important system, since K is not heavy enough to guarantee a sufficient stopping power. It was, however, interesting to study

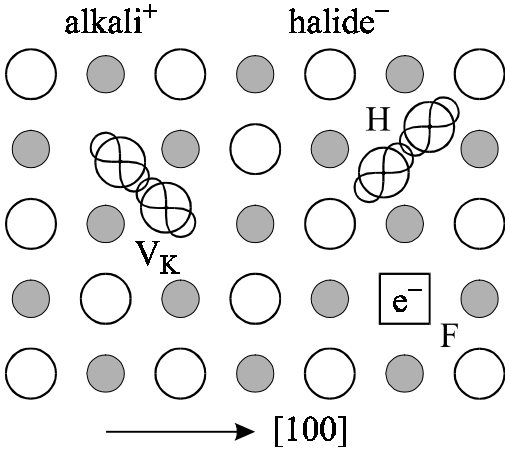

Figure 4.1 Models of F, V and H centres in cubic alkali halides.

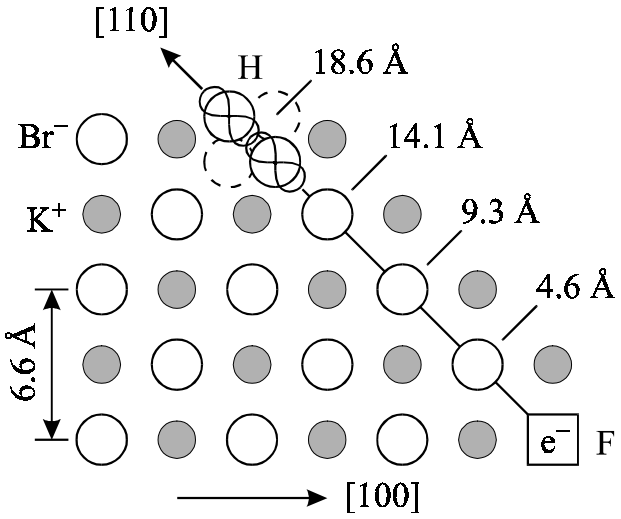

Figure 4.2 Schematic representation of the spatial correlation between F and H centre pairs in KBr as estimated from cross relaxation spectroscopy. The orientation of the H centre cannot be inferred from the experiments [60].

the mechanism in order to see whether in this case the activator plays the role of the hole trap centre.

It was shown with MCDA and MCDA-EPR that the radiation damage centres formed after X-irradiation at RT are In^{2+}, $In^0(1)$ (In^0 next to an anion vacancy [67]) and F centres [68]. Upon photostimulation into the F band at 2.06 eV (602 nm), two luminescence bands of In^+ are observed around 2.9 eV (428 nm) and 2.4 eV (517 nm) [6, 69, 70, 71]. In [68] it was shown, that there is, as in BaFBr:Eu^{2+}, a replenishment effect, but only for a low (100 ppm) In^+ doping level. For a high (1000 ppm) In^+ doping level, no replenishment effect was observed [8]. The PSL active centres in KBr:In^+ are F centres and In^{2+} hole trap centres. The role of $In^0(1)$ centres is not clear.

The PSL efficiency of KBr:In^+ depends clearly on the activator concentration. It was largest for an In^+ concentration between $8{\cdot}10^{16}$ and $2{\cdot}10^{17}\,cm^{-3}$ [72]. Investigations of the stability of the PSL active centres showed that after X-irradiation at RT 20%-30% of the initially generated F centres decay within 20-30 min [68].

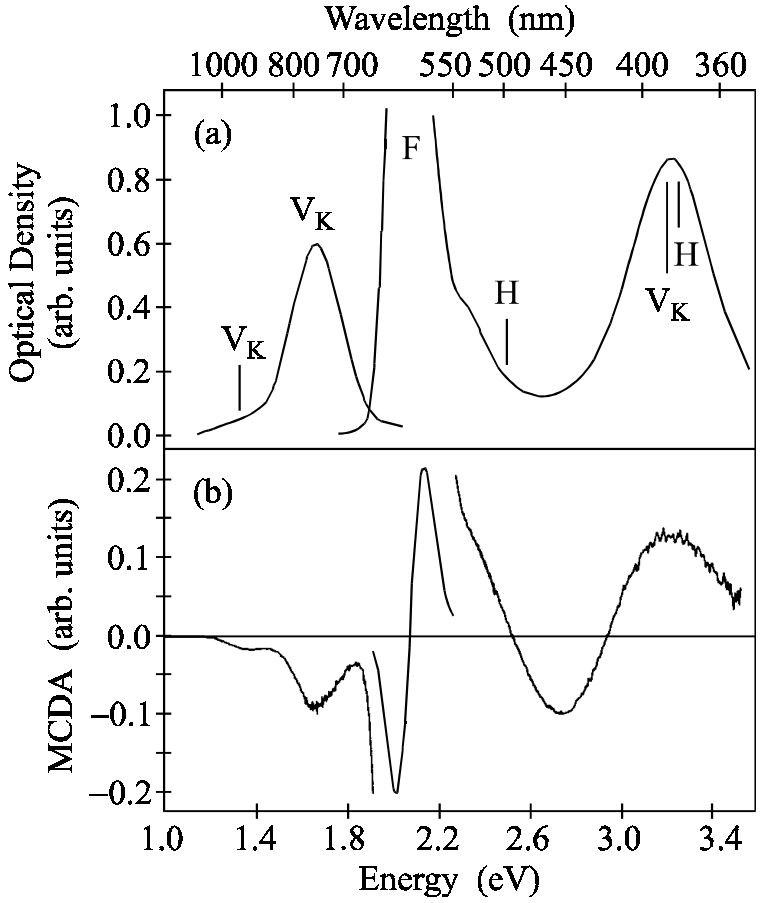

Figure 4.3 (a) Absorption of F, V_K and H centres in KBr after X-irradiation below 20 K. (b) MCDA spectrum of KBr after X-irradiation at 4.2 K, recorded at 1.5 K [60].

4.1.1 Generation of electron and hole trap centres

After X-irradiation of KBr:In^+ at 4.2 K the MCDA spectra of F, V_K and H centres have been detected [68]. For a high (1000 ppm) In^+ doping level also In^{2+} hole trap centres were found [8]. H centres are found as result of the decay of self-trapped excitons, whereby F centres are formed simultaneously [30]. For the creation of V_K centres electron traps have to be present in the crystal. However, V_K centres could also be generated in particularly pure KBr [60], i.e. there are most probably Br^- vacancies present which capture the electrons. A schematic representation of these centres in cubic alkali halides is shown in figure 4.1. No $In^0(1)$ centres could be observed when X-irradiating at 4.2 K in contrast to what was found after X-irradiation at RT. It was shown by cross-

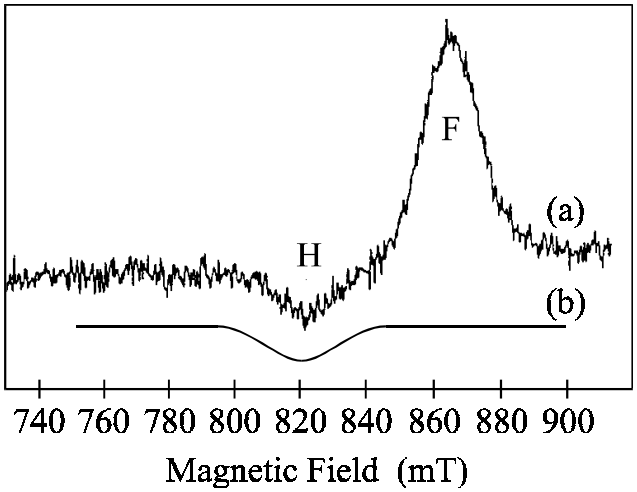

Figure 4.4 (a) MCDA-EPR spectrum of KBr X-irradiated at 4.2 K, recorded at 1.5 K for **B** || [100]. (b) EPR simulation of H centres in KBr with their axes perpendicular to **B** using $g_\perp = 2.074$, $A_\perp = 5$ mT and a halfwidth of 5 mT for the hyperfine lines [60].

relaxation (CR) spectroscopy in undoped KBr that after X-irradiation at 4.2 K all F and H centres are spatially correlated. A quantitative analysis of the CR effects yielded a F-H pair separation of four lattice spacings along the [110] directions as shown in figure 4.2 [60].

The dominant band in the optical absorption spectrum (figure 4.3a) as well as in the corresponding MCDA spectrum (figure 4.3b) is that of the F centre at 2.06 eV (602 nm) [60, 62, 68]. The three extrema in the MCDA at 3.2 eV, 1.65 eV and 1.4 eV correlate with the peaks of the V_K absorption bands [73]. The extremum at 2.8 eV cannot be correlated with any known absorption band. It is caused by forbidden transitions of the V_K centre, which become dipole allowed due to the loss of the inversion symmetry by slow oscillations [74]. Since the known H centre bands at 3.26 eV and 2.50 eV [75] are superimposed by the intense bands of the F and V_K centre, respectively, no MCDA band can be clearly assigned to the H centre. Due to the strong overlap of the H centre bands with those of the F and the V_K centre, respectively, the identification of H centres by MCDA-EPR turned out to be difficult. This superposition is clearly seen in the MCDA-EPR spectrum of figure 4.4a which shows not only the EPR line of H centres with their axes perpendicular to the magnetic field, but also that of the F centre. The fact that only those H centres can be observed was explained in [31]. Figure 4.4b shows a calculated

EPR spectrum of H centres with their axes perpendicular to the magnetic field. Upon annealing to 70 K, the H centres decay thermally.

The failure to detect In^{2+} centres after X-irradiation at 4.2 K demonstrates that F-In^{2+} pairs are not produced as primary radiation defects. The doped In^{+} impurities do not act as primary hole traps. However, the fact that In^{2+} are observable at RT shows that the formation of In^{2+} centres is thermally activated. From mobile hole trap centres the In^{+} must capture the hole to form In^{2+}. The analysis of the MCDA-EPR measurements of In^{2+} yielded that there is no other defect such as a nearest-neighbour vacancy associated with the In^{2+} centre. It was proposed that V_K centres decay at an In^{+} site to form In^{2+} [68].

4.2 RbI:Tl^{+}

The X-ray induced defects in RbI:X (X = Tl^{+}, In^{+}, Eu^{2+}, Pb^{2+}) and their role in the PSL process were investigated in detail in [7]. The following section is focussed on RbI:Tl^{+} which has, in principle, very good storage and PSL properties. However, the stored image fades away within minutes at RT. Therefore, unless a very fast read-out process is initiated immediately after taking the image, the system is less adequate for practical use. As to the mechanism, RbI:Tl^{+} is well understood. After X-irradiation the generated electron trap centre (F centre) can be photostimulated. The F centre electron recombines with the complementarily generated Tl^{2+} hole trap centre leading to the Tl^{+} emission at 2.86 eV (433 nm). The maximum of the PSL excitation spectrum is at 1.69 eV (735 nm).

4.2.1 Generation of electron and hole trap centres

X-irradiation of RbI:Tl^{+} at liquid nitrogen temperature (LNT) generates mainly F and V_K centres, only very few Tl^{2+} centres are directly formed (figure 4.5a). This was shown by MCDA and MCDA-EPR experiments [76]. Additionally Tl^{0} centres can be detected by their optical absorption bands at 0.87 eV, 1.32 eV and 2.27 eV [7]. Upon annealing to 150 K the V_K centre decays and the MCDA bands of the Tl^{2+} centre increase (figure 4.5b). Note, that the V_K centres become mobile at 125 K [77]. This is in agreement with the thermoluminescence glow curve of RbI:Tl^{+} after X-irradiation at 4.2 K which shows two characteristic peaks, at 125 K and at 175 K [7]. No Tl^{+} dis-

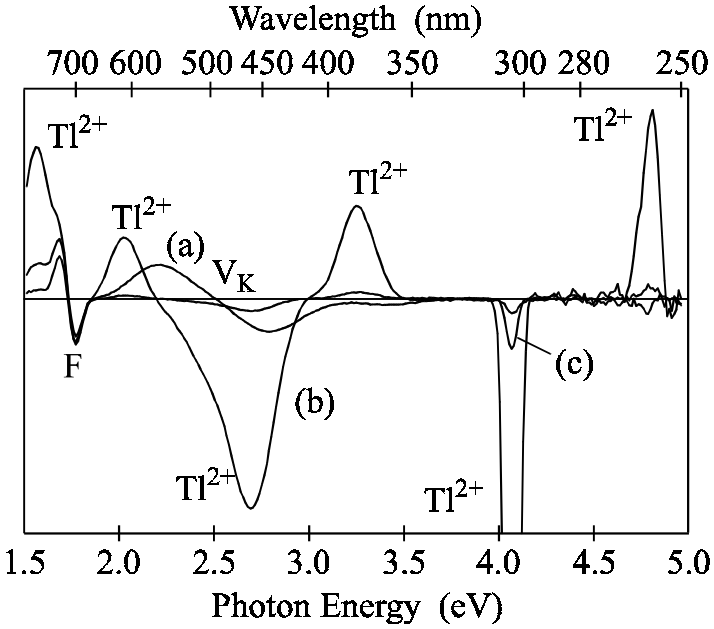

Figure 4.5 MCDA spectra of RbI:Tl^+, recorded at 4.2 K (a) immediately after X-irradiation at 80 K, (b) after subsequent annealing to 150 K and (c) after subsequent annealing to 220 K [76].

turbed V_K centres [76] could be detected. At 180 K the Tl^0 centres become mobile and recombine with Tl^{2+} centres. Consequently, after an additional annealing step to 220 K almost 95% of the Tl^{2+} have disappeared (figure 4.5c).

Tl^{2+} is paramagnetic and has seven absorption bands which could be identified by "tagged" MCDA experiments [78]. Theoretical calculations [79] showed that the unpaired 6*s*-electron of Tl^{2+} is mainly located at the I^- ligands of a $[TlI_6]^{4-}$ complex. The two UV absorption bands (4.07 eV and 4.82 eV) belong to the spin-orbit split $^2P_{1/2}$ and $^2P_{3/2}$ components of the $a^*_{1g} \rightarrow t^*_{1u}$ transition, whereas the five additional transitions (1.57 eV, 2.03 eV, 2.35 eV, 2.7 eV and 3.25 eV) can be explained by the components of the $t_{1u}(\pi) \rightarrow a^*_{1g}$, $t_{1u}(\sigma) \rightarrow a^*_{1g}$, and $t_{2u}(\pi) \rightarrow a^*_{1g}$ charge transfer transitions. Bleaching into any of the seven identified Tl^{2+} absorption bands at LNT destroys the Tl^{2+} centres and leads to the Tl^+ emission as well as to the formation of V_K centres (figure 4.6, from left to right). Upon annealing above the stability temperature of the V_K centres, 95% of the Tl^{2+} centres are restored (figure 4.6, from right to left). Thus, the V_K centres generated in this way are spatially correlated to Tl^+.

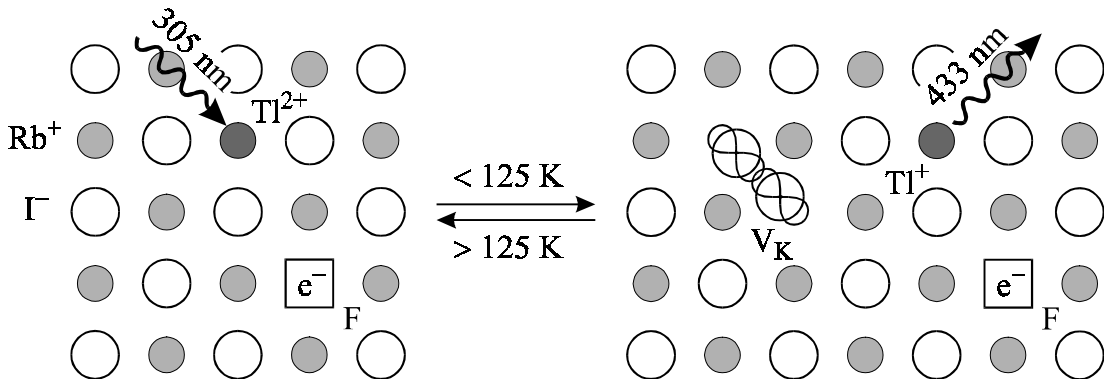

Figure 4.6 Model for the charge transfer character of Tl^{2+} in RbI:Tl^{+}.

Photostimulation into the F centre absorption band at temperatures above 150 K leads to a recombination between Tl^{2+} and F centres giving rise to the Tl^{+} luminescence, i.e. the PSL effect.

4.3 RbBr:Ga^{+} and CsBr:Ga^{+}

Before X-irradiation the excitation of RbBr:Ga^{+} or CsBr:Ga^{+} with UV light leads to a single luminescence band peaking at 2.25 eV (550 nm) and at 2.41 eV (515 nm), respectively [80, 81]. The corresponding excitation spectra revealed a broad band peaking at 4.8 eV (260 nm, RbBr:Ga^{+}) and at 5.0 eV (250 nm, CsBr:Ga^{+}), respectively. No luminescence can be detected by exciting RbBr:Ga^{+} or CsBr:Ga^{+} with light in the range between 600 nm and 800 nm. After X-irradiation at RT the Ga^{+} luminescence can be excited in the F centre absorption band at 1.85 eV (670 nm, RbBr:Ga^{+}) and at 1.94 eV (640 nm, CsBr:Ga^{+}), respectively. The PSL decay time is 26.4 µs for RbBr:Ga^{+} and 18.6 µs for CsBr:Ga^{+}, respectively [82].

4.3.1 Sample preparation

RbBr and CsBr were doped with 200-10 000 ppm Ga^{+} in the melt and single crystals were grown by the Bridgman method under inert gas. By using appropriate amounts of $GaBr_3$ and elementary gallium it was attempted to avoid the incorporation of trivalent gallium [80, 81]. Due to the crystal growth method the single crystal part grown first contains only a small Ga^{+} concentration. The Ga^{+} concentration in the melt increases with the crystal growth. Therefore, the crystal's end part is doped with a much larger

amount of Ga^+. In addition, the end part of the single crystal also contains more other unavoidable impurities than the first part. Samples from the first part and from the end part have been investigated. Henceforth, the samples are referred to as "L" (low Ga^+ concentration) and "H" (high Ga^+ concentration). The absolute Ga^+ concentration incorporated into the crystal could not be determined. The maximum concentration is probably one order of magnitude less than the doping level. From optical absorption measurements the Ga^+ concentration ratio between the L and H samples was found to be about 5:1.

4.3.2 Generation of electron and hole trap centres

After X-irradiation of RbBr:Ga^+ at 4.2 K F, V_K, H and I (interstitial halide) centres are formed. The latter two are not stable above 40 K [80, 83]. The F centre remains stable up to RT, whereas the V_K centre becomes mobile at temperatures above 180 K [80]. Note, that the V_K centre in undoped RbBr is stable only to about 170 K [77]. In undoped CsBr the V_K centres has two critical temperatures for migration, namely 106 K for 0° jumps and 130 K for 90° jumps, respectively [84]. The maxima at 110 K and 145 K in the thermoluminescence glow curve of CsBr:Ga^+ were thus assigned to the V_K decay [81].

After X-irradiation at RT the MCDA spectra of RbBr:Ga^+ and CsBr:Ga^+, respectively, show a derivative-like structured band at 1.85 eV (670 nm, RbBr:Ga^+) and at 1.94 eV (640 nm, CsBr:Ga^+), respectively, which belong to the corresponding F centres. Besides the F centre bands, several MCDA bands were detected in the UV spectral range.

MCDA-EPR experiments showed that the UV bands belong to two different Ga^{2+} hole trap centres which are henceforth labelled with $(Ga^{2+})^I$ and $(Ga^{2+})^{II}$ (figure 4.7). The EPR lines of each Ga^{2+} centre are split by a hyperfine (hf) interaction between the unpaired 4*s*-electron and the two magnetic isotopes ^{69}Ga (60.4% natural abundance) and ^{71}Ga (39.6% natural abundance), both having a nuclear spin of $I = 3/2$. The hf interaction leads to four "allowed" $\Delta m_I = 0$ transitions marked by bars in figure 4.7. The transitions labelled with asterisks are due to "forbidden" $\Delta m_I = \pm 1, \pm 2$ transitions. The forbidden transitions are nearly as intense as the allowed ones. This can occur in the MCDA detection scheme when the allowed transitions are strongly saturated due to long spin-lattice relaxation times [85]. The allowed quartet lines have the same intensity, but since they are superimposed to forbidden transitions, the intensity pattern is

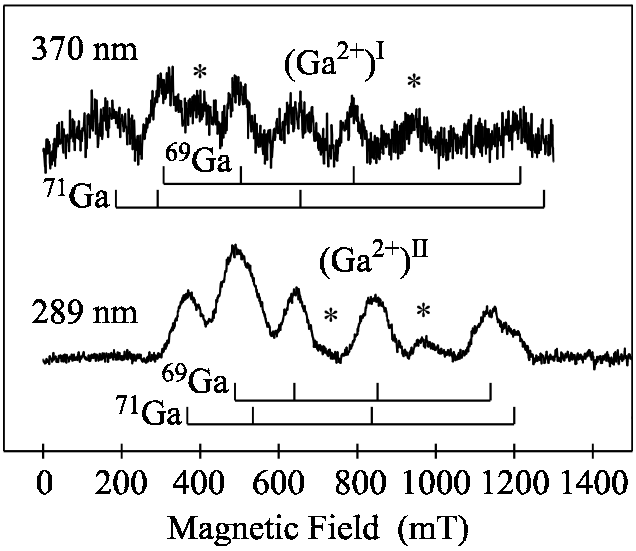

Figure 4.7 MCDA-detected EPR of $(Ga^{2+})^{I}$ and $(Ga^{2+})^{II}$ centres in RbBr:Ga^{+} (200 ppm, sample L) after X-irradiation at RT, recorded at 1.5 K applying a microwave frequency of 23.9 GHz. The detection wavelength was 3.35 eV (370 nm) and 4.28 eV (289 nm), respectively [80].

different from that expected for allowed transitions only. Unfortunately, it was not possible to resolve structural differences between these two centres by EPR.

The assignment of the UV bands to their corresponding Ga^{2+} hole trap centre was done by "tagged" MCDA measurements (figure 4.8), where an energy of 3.35 eV (370 nm) is very suitable for measuring the MCDA-detected EPR of the $(Ga^{2+})^{I}$ centres and 4.29 eV (289 nm) for the $(Ga^{2+})^{II}$ centres [80, 81].

4.3.3 Generation of $(Ga^{2+})^{I}$ and $(Ga^{2+})^{II}$ centres in RbBr:Ga^{+}

When X-irradiating at 4.2 K only F and V_K centres are observed in MCDA experiments. No Ga^{2+} centres could be found. After annealing to about 180 K, where the V_K centres have begun to disappear, Ga^{2+} centres start to appear. For RbBr:Ga^{+} (200 ppm, sample L), the MCDA band of $(Ga^{2+})^{I}$ centres appears at 180 K and reaches its maximum value at 220 K. A weak MCDA band of the $(Ga^{2+})^{II}$ centres also appears at 180 K, reaches its maximum value when annealing further to 250 K and then remains unchanged to RT (figure 4.9). Corresponding to the increase of the MCDA band of the $(Ga^{2+})^{II}$ centres the MCDA band of the $(Ga^{2+})^{I}$ centres decreases between 220 K and 250 K. At 250 K about half of $(Ga^{2+})^{I}$ centres are destroyed. For sample H, the MCDA band of $(Ga^{2+})^{I}$

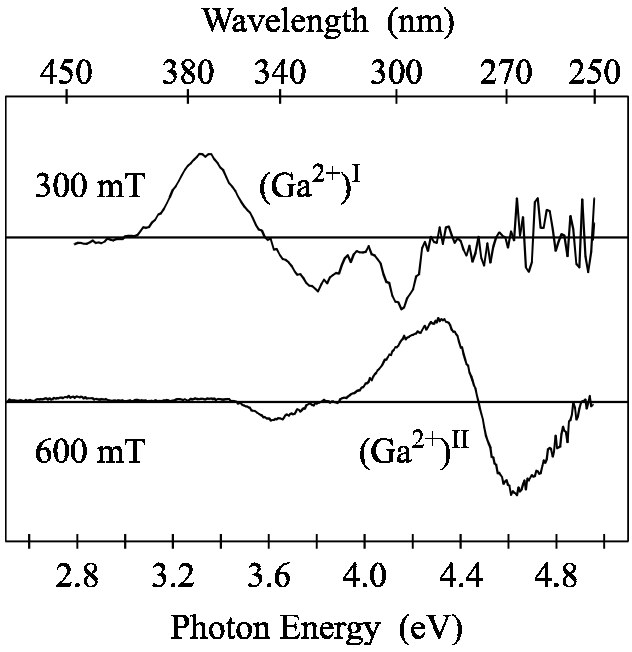

Figure 4.8 "Tagged" MCDA of $(Ga^{2+})^I$ (200 ppm, sample H) and $(Ga^{2+})^{II}$ centres (200 ppm, sample L) in RbBr:Ga$^+$, after X-irradiation at RT, recorded at 1.5 K [80].

centres appears at 180 K with a further increase to its maximum value at about 220 K. No MCDA of $(Ga^{2+})^{II}$ centres is observed, even after annealing up to RT (figure 4.9). In general, the MCDA of $(Ga^{2+})^I$ centres reaches its maximum value at about 220 K, i.e. by an annealing step above the decay temperature of the V_K centres, while the MCDA of $(Ga^{2+})^{II}$ centres reaches its maximum at 250 K.

It is obvious that the $(Ga^{2+})^I$ centres are formed from a mobile V_K centre upon hole capture by Ga$^+$, while the formation of $(Ga^{2+})^{II}$ centres needs as well the mobility of another species, thought to be cation vacancies (v_c). The $(Ga^{2+})^I$ centre is probably an isolated Ga^{2+}, whereas the $(Ga^{2+})^{II}$ centre is proposed to be a Ga^{2+}-cation vacancy complex (figure 4.10), similarly to what was proposed in [86] to occur upon X-irradiation in KCl and NaCl doped with Ga$^+$. The observation that the V_K centre does not recombine with the F centre electron, but that it is captured by Ga$^+$ could be explained by the fact that the ionic radius of the Ga$^+$ activator (0.81 Å) is almost twice smaller than that of Rb$^+$ (1.47 Å). Thus, a relaxation of the bromine neighbours towards the Ga$^+$ could occur which causes an attractive potential for the V_K centres.

The formation process of the $(Ga^{2+})^{II}$ centres is more complex than that proposed for $(Ga^{2+})^I$ centres. In KCl and RbCl cation vacancies become mobile at about 220 K [87,

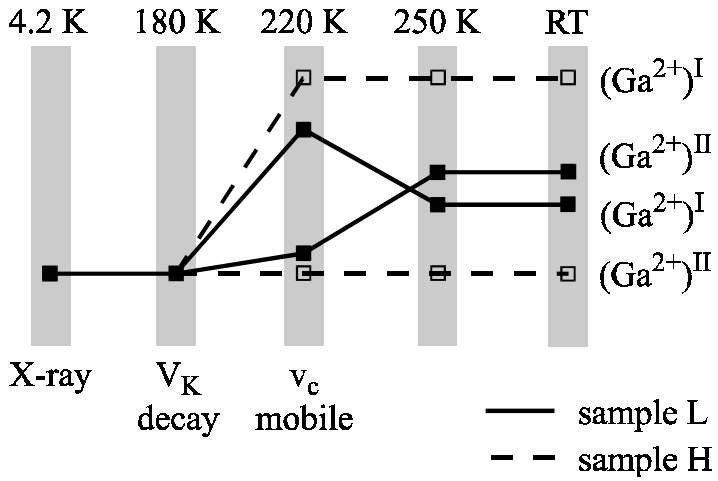

Figure 4.9 Generation of $(Ga^{2+})^{I}$ and $(Ga^{2+})^{II}$ centres in RbBr:Ga^{+} (200 ppm, sample L and sample H) after X-irradiation at 4.2 K and subsequent annealing steps to RT [92].

88, 89]. A similar mobility temperature is also expected for RbBr since the migration energy of cation vacancies in RbBr (0.81 eV) is very close to that of KCl (0.84 eV) and RbCl (0.80 eV) [90]. The mobile cation vacancies can be captured by a Ga^{2+}, which attracts the negative cation vacancies due to its positive charge. The resulting complex is electrically neutral and stable. Apparently, the investigated RbBr samples with low Ga^{+} concentration contain cation vacancies in a considerable concentration, i.e. in the same order of magnitude as the concentration of Ga^{+} in those samples which is probably due to the doping method [80]. When following the formation of Ga^{2+} centres above 220 K, the initial concentration of $(Ga^{2+})^{I}$ centres is found to decrease from 220 K to 250 K at the expense of the formation of more $(Ga^{2+})^{II}$ centres. Thus, cation vacancies are attracted by the positive $(Ga^{2+})^{I}$ centres and form $(Ga^{2+})^{II}$ centres.

After X-irradiation at RT in RbBr with low Ga^{+} concentration the MCDA shows a significant band of $(Ga^{2+})^{II}$ centres, but only a small band of $(Ga^{2+})^{I}$ centres. This is in agreement with the X-irradiation at 4.2 K and subsequent annealing procedure (figure 4.9). In RbBr with high Ga^{+} concentration the intensities of both MCDA bands are of the same order of magnitude with a smaller MCDA band of $(Ga^{2+})^{II}$ centres. This is contrary to the fact that after X-irradiation at 4.2 K and subsequent annealing to RT very few $(Ga^{2+})^{II}$ centres were found (figure 4.9). A very high mobility of the cation vacancies during the RT X-irradiation seems to favour the creation of the $(Ga^{2+})^{II}$ centres, while after low temperature X-irradiation and annealing to 220 K the V_K centres

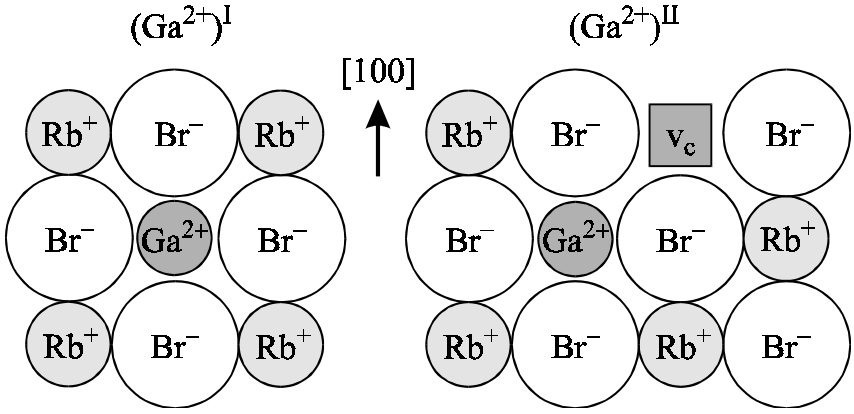

Figure 4.10 Models for the $(Ga^{2+})^{I}$ and the $(Ga^{2+})^{II}$ centre in RbBr:Ga^{+}.

are preferentially trapped at Ga^{+} to form $(Ga^{2+})^{I}$ centres and are not converted to $(Ga^{2+})^{II}$ centres. It is assumed that RbBr with high Ga^{+} concentration contains less cation vacancies than RbBr with low Ga^{+} concentration. This together with an enhanced vacancy mobility under RT X-irradiation may be the reason for the different ratio between $(Ga^{2+})^{I}$ and $(Ga^{2+})^{II}$ centres when produced by low temperature X-irradiation and annealing or by RT X-irradiation.

4.3.4 PSL experiments with RbBr:Ga^{+} and CsBr:Ga^{+}

Stimulation of the F centre absorption band of X-irradiated RbBr:Ga^{+} to excite the Ga^{+} luminescence could not destroy the $(Ga^{2+})^{II}$ MCDA signal, neither at RT nor at 4.2 K, but it decreases the $(Ga^{2+})^{I}$ MCDA band. Thus, only the $(Ga^{2+})^{I}$ centres are participating in the read-out process upon photostimulation of the F centre electron. From the proposed centre models for the two Ga^{2+} centres this is understandable, since $(Ga^{2+})^{I}$ centres are positively charged and attract mobile electrons, while the neutral $(Ga^{2+})^{II}$ centres do not. For the use of RbBr:Ga^{+} as a storage phosphor, the generation of $(Ga^{2+})^{II}$ centres must be avoided, since they may compete for primary holes.

After stimulation at 4.2 K it was possible to restore part of the $(Ga^{2+})^{I}$ centres by subsequent annealing to RT in RbBr with low Ga^{+} concentration, but not in RbBr with high Ga^{+} concentration. This “replenishment” effect [32, 33] of the $(Ga^{2+})^{I}$ centres starts to appear after annealing the sample to about 200 K and reaches its maximum after annealing to RT (figure 4.11). For a tentative explanation of this observation it is suggested [80] that the Ga^{+} concentration does not suffice to capture all holes from the

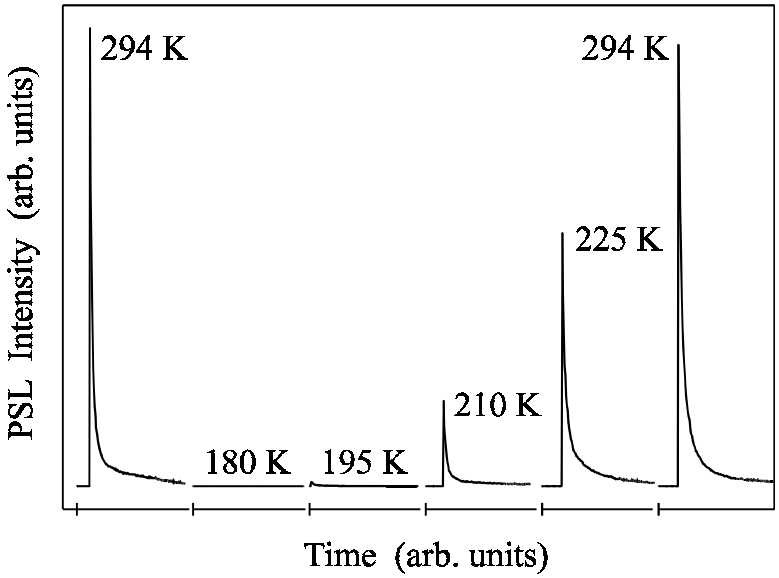

Figure 4.11 Temperature dependence of the replenishment effect in RbBr:Ga^+ (200 ppm, sample L). The PSL decay curves were detected at 2.21 eV (560 nm) under continuous excitation with 1.85 eV (670 nm) light. The sample was X-irradiated at RT, read out at 80 K, annealed up to the respective temperature and afterwards again read out at 80 K [92].

generated V_K centres. Some holes are trapped elsewhere. Above 200 K they become mobile and can be trapped by Ga^+ centres having become available again after the read-out process, i.e. after $(Ga^{2+})^I$ centres have recombined with the photostimulated electrons of the F centres. When the dose is lower, the replenishment effect decreases, since relative to the number of V_K centres there are more Ga^+ centres available to form $(Ga^{2+})^I$ centres. In RbBr with high Ga^+ concentration practically all V_K hole trap centres are trapped at Ga^+ and no replenishment effect could be observed.

In CsBr:Ga the PSL active $(Ga^{2+})^I$ centres clearly dominate over the PSL inactive $(Ga^{2+})^{II}$ species for all investigated Ga^+ doping levels [81]. The structure of these two Ga^{2+} hole trap centres is assumed to be the same as in RbBr:Ga^+ [80]. However, in contrast to RbBr:Ga^+, there is no clear replenishment observable in CsBr:Ga^+. It has therefore less complications compared to RbBr:Ga^+ with the X-ray induced formation of PSL inactive $(Ga^{2+})^{II}$ centres depending on the doping level (and possibly the way of Ga^+ doping).

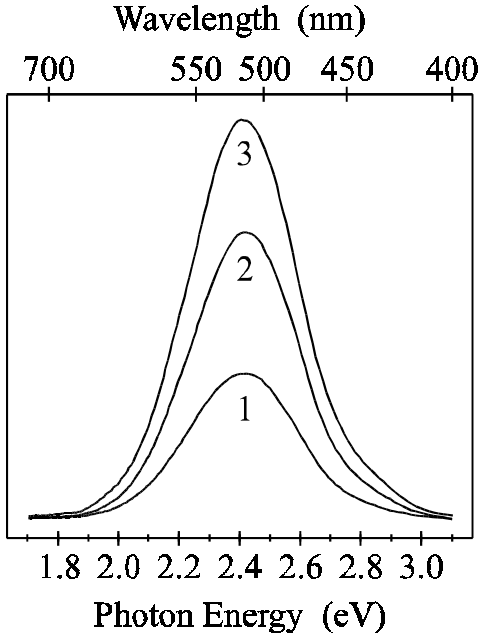

Figure 4.12 Ga^+ luminescence of CsBr:Ga^+ (3000 ppm, sample L) before (curve 1) and after an annealing/quenching procedure (curves 2 and 3). The annealing temperature was 340 °C (curve 2) and 520 °C (curve 3), respectively [81].

4.3.5 Optimal activator concentration and Ga^+ aggregation

The Ga^+ concentration plays an important role in the hole trap centre formation, particularly in RbBr, and decides whether $(Ga^{2+})^I$ alone or additionally competing $(Ga^{2+})^{II}$ centres are formed. In KCl:Ga^+ a clear tendency of Ga^+ to form aggregates has been observed [91]. Thus, for the practical use of the systems RbBr:Ga^+ and CsBr:Ga^+ it is important to know whether the doped activator forms aggregates or not. The possible aggregate formation can be detected by measuring the UV excited Ga^+ luminescence as a function of the doping level. The luminescence was detected before and after an annealing/quenching procedure in order to see whether or not aggregates may have been formed which can be destroyed by the annealing/quenching step [92].

It turned out that in RbBr:Ga^+ very high Ga^+ doping levels do not seem advantageous, since a Ga^+ aggregation occurs which could not be countered by the annealing and quenching treatment used. A somewhat surprising result came from the investigation of the PSL effect as a function of Ga^+ doping level. The highest PSL signal is obtained for a low Ga^+ concentration. This means, that apparently the formation of Ga^+ aggregates is

negative for the PSL effect, while the formation of $(Ga^{2+})^{II}$ centres seems not to affect the PSL efficiency. For practical purposes it seems that even a low concentration of $(Ga^{2+})^{I}$ centres is sufficient, while too many aggregates seem negative. It remains to be investigated how the formation of $(Ga^{2+})^{II}$ centres can be minimised compared to $(Ga^{2+})^{I}$ centres. If RbBr:Ga^{+} is to be used in practical screens, an investigation of the effect of annealing should be carried out with a variation of annealing temperatures.

In CsBr:Ga^{+} a significant tendency of Ga^{+} to aggregate was also found. Annealing (and subsequent quenching) destroys the aggregates. However, the annealing temperature has to be sufficiently high. Figure 4.12 shows that an annealing temperature of 340 °C was not high enough to break all the aggregates, whereas annealing up to 520 °C and subsequent quenching yielded an even larger increase in the Ga^{+} luminescence. Note, that the melting temperature of CsBr is at 632 °C. Re-aggregation under light takes place within about a day at RT. When the sample is kept in the dark, experiments on the re-aggregation showed no significant difference between the signal measured directly after the annealing and subsequent quenching treatment within a day. Thus the Ga^{+} re-aggregation in this case lasts at least some days or weeks.

The PSL is also influenced by the Ga^{+} aggregation, in particular for higher doping levels. If one wants to use CsBr:Ga^{+} as X-ray storage phosphor, it is certainly necessary to consider the Ga^{+} aggregation. The cooling process has to be adjusted accordingly.

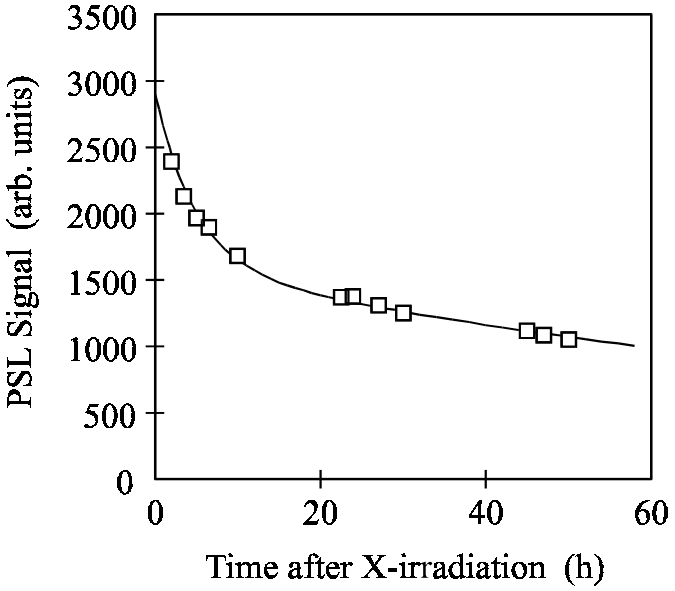

Figure 4.13 Fading of the PSL effect of RbBr:Ga^+ (200 ppm) in the dark at RT, excitation at 670 nm, detection at 550 nm [92].

4.3.6 PSL fading

The fading of the PSL, i.e. the electron and hole recombination with time in the dark and thus the partial loss of the stored information, is an important feature for the application of RbBr:Ga^+ or CsBr:Ga^+ as X-ray storage phosphors. Figure 4.13 shows the fading of the stored information as a function of time measured for RbBr:Ga^+ (200 ppm) which revealed the best PSL performance. The sample was X-irradiated for 15 min (60 kV, 15 mA). The decay of the PSL with time was followed by stimulating the sample with F light (670 nm) and detecting the Ga^+ emission at 550 nm several times from directly after the X-ray exposure up to two days. The stimulating 670 nm light was very weak, such that the PSL signal measured twice within a few seconds showed no change in its magnitude. The measured PSL fading with time could be fitted by two exponential functions with $\tau_1 = 5$ h and $\tau_2 = 125$ h. The initial PSL intensity is halved after approximately 14 h [92].

For RbBr:Ga^+ the fading of the PSL was followed in the dark detecting the PSL intensity with weak stimulation light. In case of CsBr:Ga^+ the investigation of the F centre fading by detecting its MCDA showed that after 20 hours one third of the initial F centre concentration is lost.

4.3.7 Red-shift of the PSL excitation

It is known from previous work on alkali halides that doping with lighter alkali cations leads to the formation of perturbed F centres, so-called F_A centres [62]. In these centres one of the nearest neighbour cations of the F centre is replaced by an alkali ion of smaller size, so that an F centre with reduced local symmetry is formed. Figure 4.14 shows the F_A centre in RbBr (fcc lattice structure) doped with lithium and the corresponding absorption bands. In this configuration the F_A centre absorption band splits into two bands one of which is red-shifted (F_{A1}), the other one only slightly different from the normal F band (F_{A2}). If the incident light is polarised along the F-Li^+ direction, the so-called F_{A1} absorption band is measured which represents the more red-shifted one. Choosing the polarisation perpendicular to the F-Li^+ direction the F_{A2} band is observed. In table 4.2 the literature data of F_A centres in RbBr and CsBr for several co-dopings are summarised. The F_{A1} absorption band is further red-shifted the lighter the doped alkali cation (note, that this simple rule generally applies to the alkali halides with fcc structure, not to those with bcc structure).

crystal	dopant	F_{A2}	F_{A1}
RbBr		1.86 eV (670 nm)	
	Li	1.78 eV (697 nm)	1.57 eV (790 nm)
	Na	–	–
	K	1.85 eV (671 nm)	1.67 eV (742 nm)
CsBr		1.81 eV / 685 nm	
	Li	1.78 eV (697 nm)	1.60 eV (775 nm)
	Na	1.83 eV (678 nm)	1.65 eV (751 nm)
	K	1.77 eV (701 nm)	1.58 eV (785 nm)
	Rb	1.75 eV (709 nm)	1.66 eV (747 nm)

Table 4.2 Optical absorption bands of several F_A centres in RbBr and CsBr [62, 93].

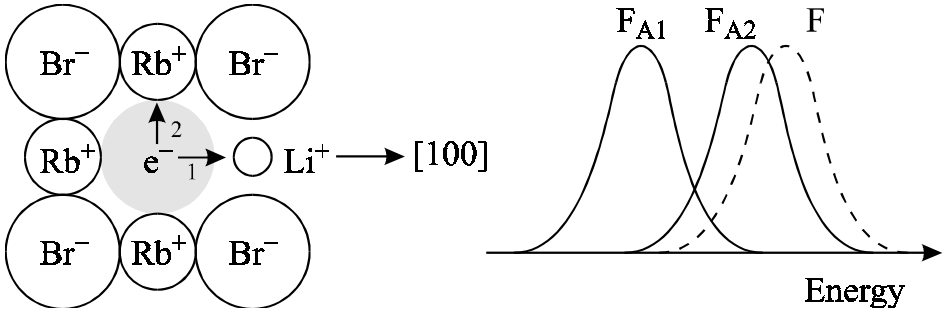

Figure 4.14 Schematic representation of the F_A centres in RbBr (fcc structure) doped with Li^+ and the corresponding absorption spectra in comparison with the unperturbed F centre band [62].

What is known from the literature is the formation of F_A centres using doping levels of the order of a few percent and additive coloration. Only a statistically small fraction of F centres is formed as the F_A species. Upon bleaching into the F band at RT, a larger fraction (usually about 50% of F centres) is transformed into F_A centres.

It is not clear a priori whether F_A centres in alkali halide compounds are formed upon X-irradiation at all, whether they are possibly preferentially formed compared to normal F centres and whether they contribute to the read-out process. Upon X-irradiation of BaFBr:Eu co-doped with Ca^{2+} or Sr^{2+}, respectively, $F_A(Ca^{2+})$ or $F_A(Sr^{2+})$ centres were formed which generated the desired red-shift of the PSL excitation spectrum [51, 61].

According to table 4.2 RbBr doped with Li^+ should yield the largest red-shift of the F_A centre absorption bands. Figure 4.15 shows the MCDA spectrum of RbBr:(0.1% Ga^+, 1% Li^+) after X-irradiation at RT. Besides the strong F centre band an additional band with its maximum peaking at 1.57 eV (790 nm) appears. Corresponding to the data of table 4.2 this band is assigned to the F_{A1} transition of perturbed F centres due to the Li^+-doping. After bleaching into the F band at RT using a HeNe laser, a fraction of the F centres could be converted into F_A centres. PSL excitation spectra of RbBr:(Ga^+, Li^+) proved that the F_A centres are photostimulable in all their absorption bands and, therefore, permit read-out of stored X-ray information in the near infrared region [92].

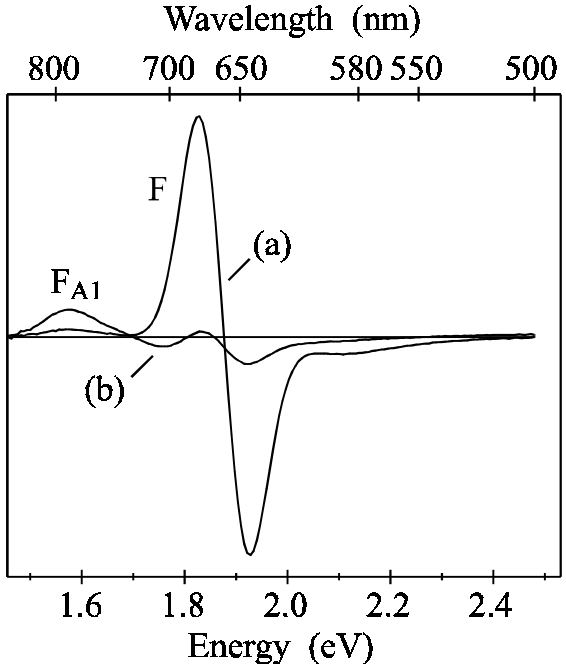

Figure 4.15 MCDA spectra of RbBr:(0.1% Ga^+, 1% Li^+), recorded at 1.5 K (a) immediately after X-irradiation at RT and (b) after 60 sec bleaching (HeNe laser) at RT [92].

The dose dependence of the amount of the X-ray induced F and F_A centres was analysed by measuring the MCDA of both centres for X-ray doses from 40 mR to 1400 mR at 1.5 K in 1% Li^+-doped RbBr:Ga^+. The results are presented in figure 4.16: The magnitudes of the MCDA maxima of the F and F_A centres (for the latter the F_{A1} maximum) are determined for each dose and plotted versus the X-ray dose. In the high dose regime the F and F_A bands increase approximately to the same degree, whereas in the low dose regime the F band increases faster than the F_{A1} band with increasing dose. For doses lower than 40 mR the signal to noise ratio was too poor to clearly separate the F_{A1} MCDA band from the background.

Figure 4.17 presents the percentage of F_{A1}/F versus the applied X-ray dose, calculated from the data of figure 4.16. It is seen more clearly in this diagram that the F_A formation is preferred when X-irradiating with low doses, comparable to doses applied in medical diagnostics. The relative fraction of F_{A1}/F increases to about 10% at 40 mR for the investigated sample which exceeds the 6% statistical chance (6 next nearest neighbours) that an F centre is formed adjacent to a Li^+ cation. A disadvantage is that the $F_A(Li^+)$ centres have a faster fading component compared to the F centres in RbBr:Ga^+. Espe-

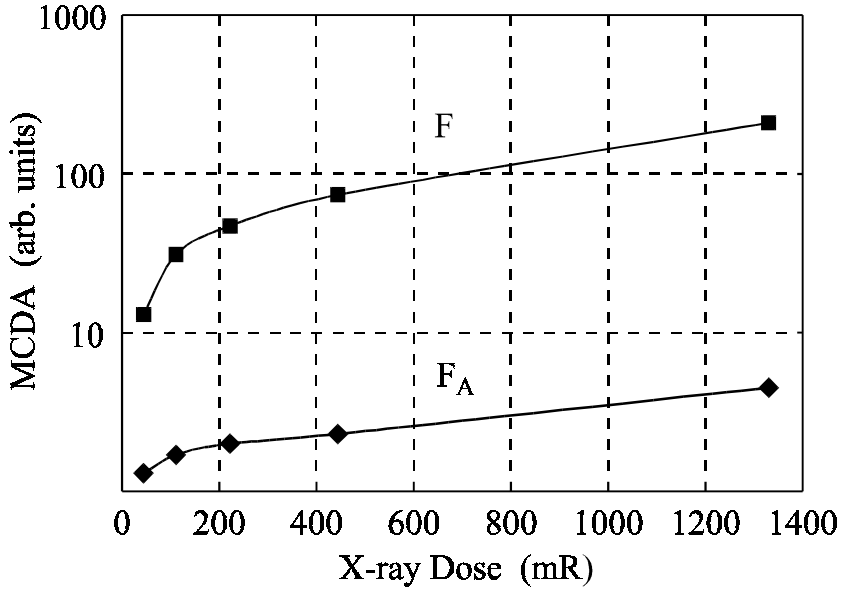

Figure 4.16 X-ray dose dependence of the intensity of the F and F_{A1} MCDA bands in 1% Li^+-doped RbBr:Ga^+. The spectra were recorded at 1.5 K after X-irradiation at RT [92].

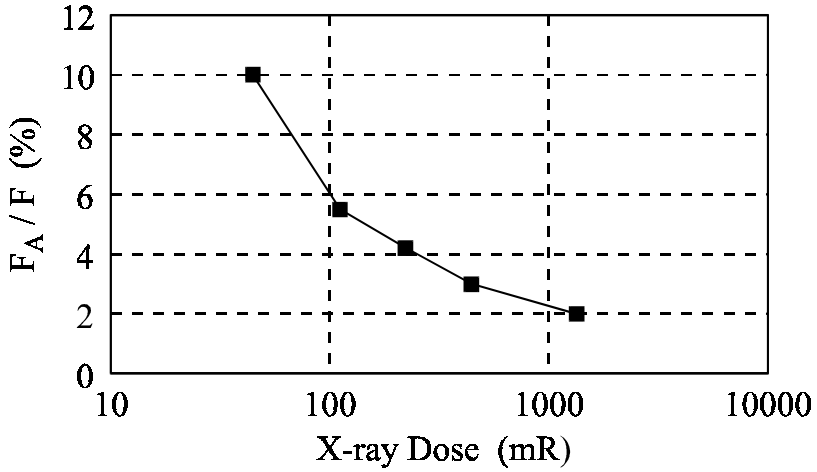

Figure 4.17 Relative amount of F_A over F as a function of the X-ray dose for 1% Li^+-doped RbBr:Ga^+ [92].

cially a high Li^+ doping level of 10% seems disadvantageous, since the half time of the F_A centres is only 2 hours compared to the 14 hours of the F centres [92].

It was not possible to produce $F_A(K^+)$ centres in RbBr:Ga^+ by X-irradiation. However, Na^+-doping leads to an $F_{A1}(Na^+)$ band peaking at about 750 nm, less red-shifted than that of $F_A(Li^+)$. $F_A(Na^+)$ has not been followed further, since it seems less attractive.

Co-doping CsBr:Ga^+ with lighter alkali ions to achieve a red-shift of the PSL excitation seems less attractive. However, a red-shift of the PSL excitation is feasible even though it is not as much pronounced as in RbBr:(Ga^+, Li^+). Unfortunately, the F_{A1} band responsible for the red-shift could not be enhanced by a bleaching technique. Moreover, the creation of a red-shift of the PSL excitation in CsBr:Ga^+ by co-doping with light alkali ions is disadvantageous regarding the PSL performance. Only a Rb^+ co-doping seems promising [92].

4.4 RbBr:Eu^{2+} and CsBr:Eu^{2+}

CsBr doped with Eu^{2+} has a figure of merit as high as BaFBr:Eu^{2+} [22]. Although no UV excited photoluminescence of Eu^{2+} could be observed, there was a significant PSL effect after X-irradiation of CsBr:Eu^{2+} at RT. It is known that Eu^{2+} doped into CsBr forms dipoles of Eu^{2+} and charge compensating cation vacancies (v_c) which agglomerate very quickly to different types of aggregates [94]. The investigated CsBr:Eu^{2+} samples did not show any photoluminescence, but an intense X-ray luminescence (XL). The XL spectra comprised several luminescence bands which are probably due to different kinds of Eu^{2+} aggregates. After X-irradiation at RT the PSL spectra stimulated in the F centre absorption band reproduce the XL spectra quite well. It seems that all Eu^{2+} aggregates observed in XL participate in the PSL process. The radiative life time of these Eu^{2+} aggregates is about 1 ms [22] and thus much longer to the one of isolated Eu^{2+} ($\approx 1\,\mu s$).

After X-irradiation at RT there was also a PSL effect in RbBr:Eu^{2+}. Here, it was even possible to observe UV excited photoluminescence due to isolated Eu^{2+}-v_c dipoles and different Eu^{2+} aggregates [95]. MCDA investigations yielded several intense bands in the spectral range between 220 and 420 nm. MCDA-detected EPR showed not only EPR lines from the [110] oriented Eu^{2+}-v_c dipole [96], but also from further Eu^{2+} aggregates.

4.5 The elpasolites $Cs_2NaYF_6:Ce^{3+}$ and $Cs_2NaYF_6:Pr^{3+}$

Elpasolites of type Cs_2NaYF_6 have a cubic crystal structure [97] (figure 4.18). The Na^+ and Y^{3+} ions build a sublattice with NaCl structure. The Cs^+ ions occupy the centre of the unit cell of the Na^+-Y^{3+} sublattice whereas the F^- ions reside on the axis connecting Na^+ and Y^{3+}. A trivalent activator, such as Ce^{3+} or Pr^{3+}, substitutes for Y^{3+} in sites with octahedral symmetry.

Under X-ray or UV excitation Ce-doped Cs_2NaYF_6 shows a strong emission band at 3.44 eV (360 nm) arising from the allowed 5*d*-4*f* transition of Ce^{3+}. Cs is a heavy ion, so the expectation is that if electron and hole trap centres can be formed, storage and PSL properties will be found. Indeed, it has been found that upon X-irradiation the luminescence of the activator Ce^{3+} at 3.44 eV (360 nm) can be photostimulated by excitation at about 2.25 eV (550 nm) at 300 K [2, 9, 98]. The PSL decay time of Ce^{3+} is fast, namely 42 ns at RT, and is, within experimental error, identical with the Ce^{3+} radiative life time upon direct UV excitation. Thus, the bottleneck for the PSL decay time is the

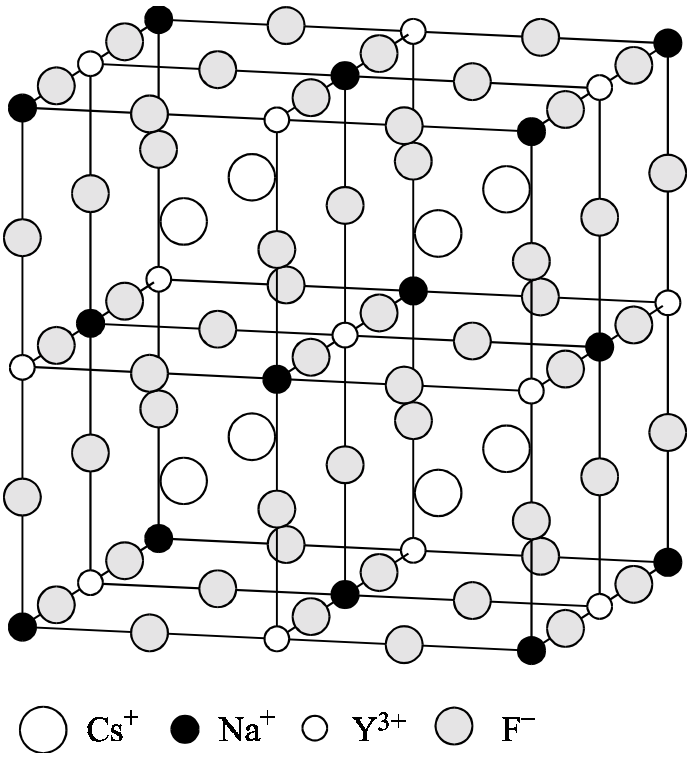

Figure 4.18 Crystal structure of the cubic elpasolite Cs NaYF .

radiative life time of the activator Ce^{3+}. One can assume that the electron-hole recombination process occurs via tunnelling and not via the conduction band. PSL has also been observed for Pr^{3+} as activator [2, 9, 98]. However, the radiative life time of the PSL is much longer, i.e. 4 ms at RT.

The maximum of the PSL stimulation of $Cs_2NaYF_6:Ce^{3+}$ is at about 530 nm, i.e. a frequency-doubled Nd-YAG (533 nm) would be ideal for photostimulation. For a stimulation at 633 nm (HeNe laser) the PSL efficiency is already reduced to 40%. In comparison to $BaFBr:Eu^{2+}$ the PSL stimulation is shifted to shorter wavelength which makes the use of cheap semiconductor light emitting diodes (LED) as light sources for photostimulation impossible. Investigations on the stability of the photostimulable centres showed that the PSL efficiency is reduced to half its value after storing X-irradiated $Cs_2NaYF_6:Ce^{3+}$ in the dark at RT for 80 min. This value is still acceptable for an X-ray storage phosphor. After 30 h the PSL efficiency decreases to a constant value of 15%. The conversion efficiency (CE) of $Cs_2NaYF_6:Ce^{3+}$ was determined to 15 $pJ/mm^2/mR$, i.e. comparable to $BaFBr:Eu^{2+}$, whereas the stimulation energy was 90 $\mu J/mm^2$, i.e. somewhat higher, but still in the same order of magnitude as $BaFBr:Eu^{2+}$ [99].

MCDA and MCDA-EPR spectroscopy showed that the photostimulable electron trap centres are F centres. ENDOR measurements have shown that the F centres in this crystal are of lower symmetry than, for example, in the alkali halides or in BaFBr [100, 101]. The hole trap centre is the activator, i.e. Ce^{3+} or Pr^{3+}. The proof for this was established when examining diamagnetic Pr^{3+} as an activator, since after X-irradiation this turned into paramagnetic Pr^{4+}, which could be detected by EPR. Ce^{3+} ($[Xe]\,4f^1$) is paramagnetic due to its unpaired *f*-electron, whereas Pr^{3+} ($[Xe]\ 4f^2$) has no unpaired electron and is thus diamagnetic. After X-irradiation Ce^{3+} captures a hole and is converted to diamagnetic Ce^{4+} ([Xe]), but Pr^{3+} to paramagnetic Pr^{4+} ($[Xe]\ 4f^1$). To check whether Ce^{4+} or Pr^{4+} is really the corresponding hole trap centre in the PSL process, it was easier to observe a rise of the Pr^{4+} EPR than a decrease of the very intense Ce^{3+} signal intensity.

X-irradiation of undoped Cs_2NaYF_6 below 100 K creates mainly F and V_K centres which are present in a comparable number. The *g* tensor and the hyperfine tensor of the V_K centre are very similar to those of the V_K centre found in NaF [77]. The V_K centre has two optical absorption bands, at 1.43 eV and at 3.69 eV, which correspond to the Σ_u-Π_g and the Σ_u-Σ_g transition of the X_2^- molecule, respectively [77]. This assignment was confirmed by MCDA-EPR. The V_K centre decays thermally at temperatures above

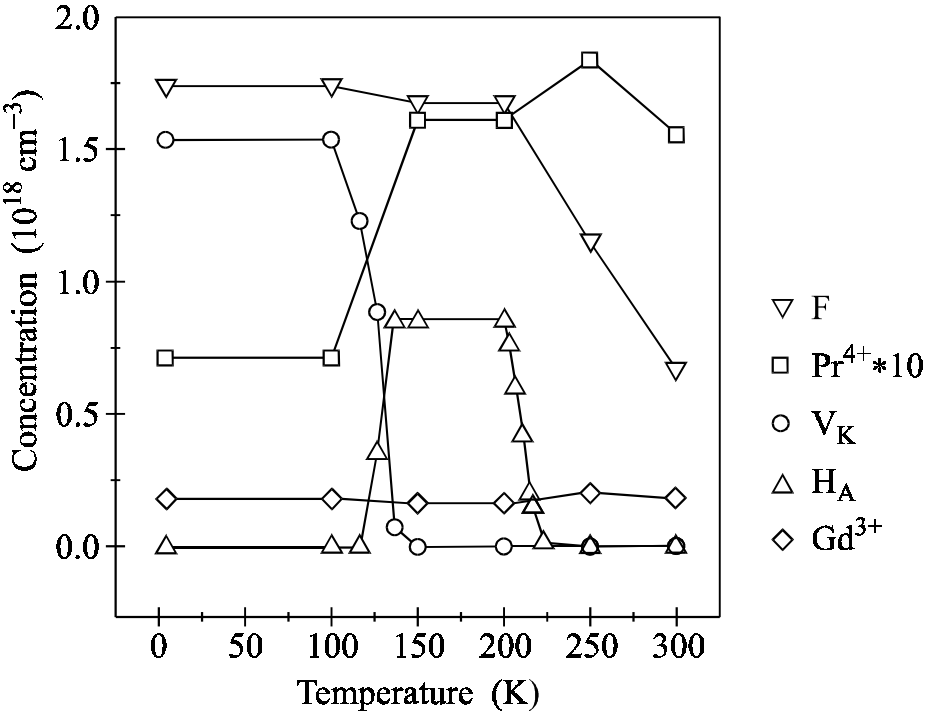

Figure 4.19 F and hole trap centre concentration in $Cs_2NaYF_6:Pr^{3+}$ after X-irradiation at 10 K and subsequent annealing steps up to RT. Gd^{3+} was present as an unintended impurity [100].

150 K whereby new hole trap centres of X_2^- type appear which are not exactly aligned along [110] what is expected for an unperturbed alignment of these centres. It is assumed that they are K^+- or Rb^+-perturbed H centres (H_A centres) [100, 101]. The optical absorption bands of the H_A centre are shifted to higher energies compared to the V_K centre, i.e. to 1.66 eV and 3.86 eV, respectively. The F centre concentration is almost unaffected by this annealing step to 150 K. The decay of the H_A centre at about 230 K is accompanied by a significant decrease in the F centre concentration.

The F and hole trap centre concentration of $Cs_2NaYF_6:Pr^{3+}$ after X-irradiation at 10 K and subsequent stepwise annealing to RT is shown in figure 4.19. X-irradiation at 10 K generates not only F and V_K centres, but also a small number of Pr^{4+} centres. Note, that in figure 4.19 the Pr^{4+} concentration is scaled up by a factor of 10. The holes are liberated by the V_K centre decay at 150 K and captured by interstitial fluorines forming H_A centres. Some of the holes are captured by Pr^{3+} causing an increase of the Pr^{4+} concentration by a factor of 2 whereby the PSL efficiency is increased by the same amount. Annealing to 230 K leads to the H_A centre decay and simultaneously to a partial decay

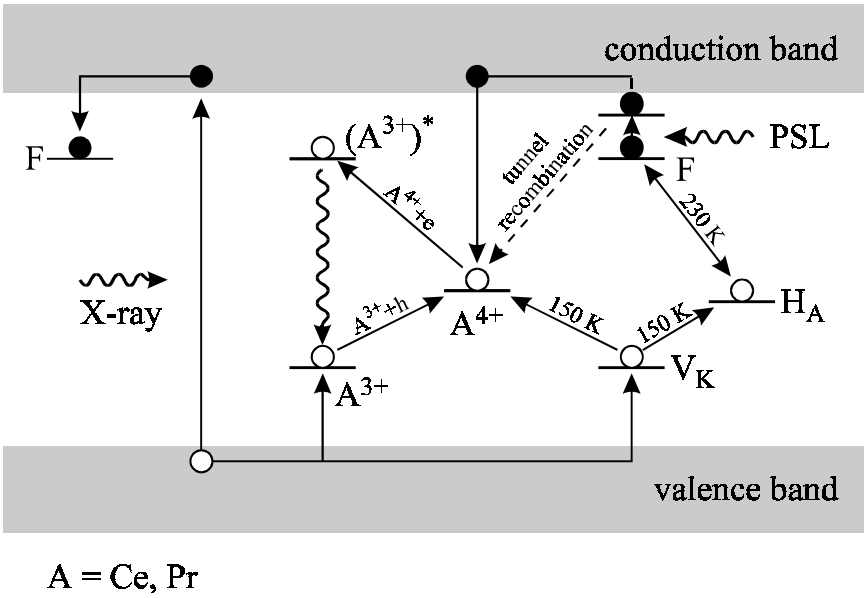

Figure 4.20 Scheme of the PSL mechanism and the thermal conversion of the generated hole trap centres in X-irradiated Cs NaYF :Ce^{3+}, Pr^{3+} [98].

of the F centres. The F centre concentration is reduced further by annealing to RT, which is probably due to a recombination with unidentified hole trap centres, whereas the Pr^{4+} concentration and the PSL efficiency remains unchanged.

Stimulation experiments have shown that about 50% of the PSL active F and Pr^{4+} centres are spatially correlated. This result was obtained by detecting the EPR signal of the paramagnetic Pr^{4+} after X-irradiation at RT. Stimulating at 10 K into the F centre absorption band reduces the Pr^{4+} concentration considerably in the first minutes, but reaches a constant value of about 50% upon continued stimulation. The initial exponential decrease indicates a tunnelling recombination of pairs of electron (F centre) and hole trap centres (Pr^{4+}) which are separated by definite distances having only a small variation. In BaFBr doped with the activator Eu^{2+} the PSL process occurs also via a tunnelling recombination between the created electron and hole trap centres [23]. A subsequent stimulation at RT destroys all the remaining Pr^{4+} centres. This observation can be explained by the assumption that 50% of the PSL-active F and Pr^{4+} centres, generated by X-irradiation at RT, are spatially correlated. It is possible to read them out even at 10 K by inducing a tunnelling recombination. The non-correlated centres are not PSL-active at low temperatures. Their recombination requires thermal activation. The optically excited electron of the F centre may then escape thermally from its relaxed excited state into the conduction band. Figure 4.20 shows the two proposed recombina-

tion paths and the thermal conversion of the created defects. In $Cs_2NaYF_6:Ce^{3+}$ the mechanism is considered to be analogue to the one in the Pr^{3+}-doped elpasolite, i.e. Ce^{4+} plays here the role of the PSL-active hole trap centre [98].

Chapter 5

Glasses and glass ceramics

A continuing difficulty in the dimensional X-ray imaging is that in X-ray storage phosphor screens considerable scattering of the read-out light occurs, limiting the resolution to around 5 line pairs / mm. One possible improvement to this scattering problem would be a phosphor based on a cubic system as discussed in section 5 or a phosphor based on a glass. There have been reports of the observation of a weak PSL in Eu-doped fluoroaluminate glass [102], and in Ce- or Eu-doped borate based glasses [103, 104]. Unfortunately, the magnitude of the weak PSL effect was not stated. A glass phosphor would have the additional advantages of arbitrary shapes useful for applications in medicine and non-destructive testing.

In contrast to the literature it was reported [105] that in Eu- or Ce-doped fluoroaluminate glass, or in a Eu-doped borate glass no PSL was observed at RT. However, a significant PSL was seen in a modified Eu^{2+} doped fluorozirconate glass, where a substantial fraction (5%) of the fluoride ions were replaced by bromide ions in the melt resulting in a glass ceramic containing small crystallites of a high-pressure phase of $BaBr_2$.

5.1 Production of fluorozirconate glasses and glass ceramics

The well-known ZBLAN20 composition for fluorozirconate glasses was modified by replacing most of the NaF with NaBr so that the total number of Br^- ions was 5% of the total number of anions, and by substituting some of the LaF_3 with YF_3 to improve the glass quality. The composition of the modified glass was then 53% ZrF_4, 20% BaF_2, 6% NaF, 14% NaBr, 1.5% LaF_3, 3% AlF_3, 1% EuF_2 or CeF_3 and 1.5% YF_3. The glass raw materials were first mixed and then melted in a glassy carbon crucible at about 750 °C,

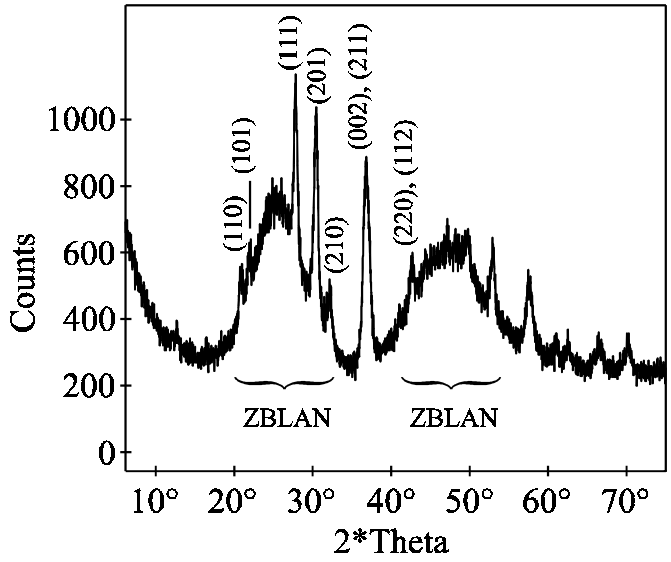

Figure 5.1 X-ray diffraction spectrum for Cu Kα radiation of bromine-doped fluorozirconate glass, recorded at RT [106].

before being poured out into a brass mould at 220 °C and cooled to RT over 12 hours. The whole glass manufacture was done in an inert nitrogen atmosphere. There was evidence of crystallisation in all of the doped glasses, ranging from a near-transparent glass which was yellow in transmitted light but blue in scattered light, to one which was opaque and milky-white. These differences presumably reflect variations in crystallite size and concentration [105].

5.2 X-ray diffraction of fluorozirconate glasses and glass ceramics

X-ray diffraction of the base glass with no bromine doping showed no sharp peaks, just broad maxima at 26 and 47 degrees (for Cu Kα radiation) typical for glasses close to the ZBLAN formulation. However, the bromine-doped glass (milky-white) showed a pattern of relatively sharp diffraction lines from an included crystalline phase superimposed on the broad glass background (figure 5.1). Almost all of the lines in the pattern could be attributed to the so-called high pressure form of $BaBr_2$ which has the anti-Fe_2P structure [107, 108].

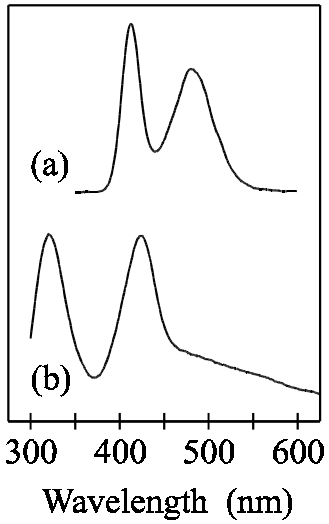

Figure 5.2 Photoluminescence spectra recorded at RT for (a) the Eu^{2+} doped glass ceramic and (b) the Ce^{3+} doped glass ceramic, excited at 270 nm [105].

5.3 Photoluminescence and PSL of fluorozirconate glasses and glass ceramics

The photoluminescence spectrum of the base glass, without bromine doping, showed no fluorescence from Eu^{2+} or Ce^{3+} ions, although it was clear from EPR and Mössbauer studies that Eu^{2+} was certainly present in the Eu^{2+} doped glass [109]. This quenching of the fluorescence has been tentatively ascribed to competing charge transfer processes involving the Zr^{4+} ions [109]. In contrast, the glass with bromine doping and either Eu^{2+} or Ce^{3+} co-doping each show two PL bands, at 413 nm and a broader band centred at 485 nm for Eu^{2+}, and one band at 320 nm and a broader band at 425 nm for Ce^{3+}, as shown in figure 5.2. Since Eu^{2+} and Ce^{3+} ions in the glass itself do not fluoresce, the observed emissions probably come from Eu^{2+} or Ce^{3+} in the crystallites. The bands were tentatively assigned to 5*d*-4*f* transitions of Eu^{2+} or Ce^{3+} ions at the two Ba^{2+} sites in the $BaBr_2$ crystallites [105]. The PL spectrum which was observed in the Eu^{2+} glass ceramic is quite different from the single band observed in the low pressure form of $BaBr_2$ doped with Eu^{2+} [110]. However, the emissions could also come from Eu^{2+} or Ce^{3+} containing Br^- aggregates in the glass. At present this is an open question.

Of the two luminescent peaks for Eu^{2+} only that at 413 nm shows a measurable PSL effect. For the Ce^{3+}-doped glass ceramic, only the peak at 425 nm showed PSL. The

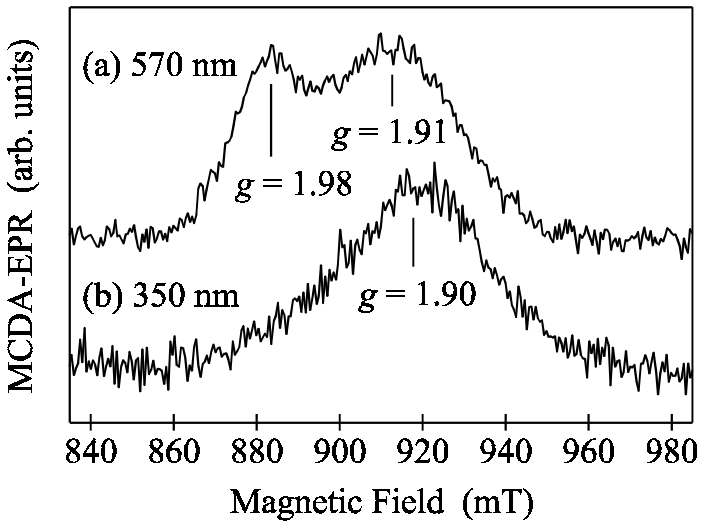

Figure 5.3 MCDA-detected EPR of Ce-doped fluorozirconate glass, detected at (a) 570 nm and (b) 350 nm, recorded at 1.5 K after X-irradiation at RT applying 24 GHz microwave frequency [114].

relative magnitudes of the effects were determined by performing identical spectroscopic measurements on a piece of crystalline BaFBr:Eu^{2+} (1000 ppm europium) and the glass ceramic (milky-white), except for a longer exposure time in the latter case. This comparison showed that the PSL effect in the glass ceramic was approximately 4000 times weaker in the case of Eu^{2+} and 2000 times weaker in the case of Ce^{3+} compared to BaFBr:Eu^{2+}, after the longer exposure time was compensated for. The excitation spectrum for the PSL, being the luminescence intensity at 413 nm for Eu^{2+} and at 425 nm for Ce^{3+} as a function of the photostimulation wavelength, comprises a broad peak centred at about 570 nm, with a similar spectral shape in both cases.

5.4 Electron and hole trap centres

It is known from other X-ray storage phosphors such as elpasolites (e.g. [9]) that Ce^{3+} acts as a very efficient hole trap centre being converted to Ce^{4+}. Assuming that the diamagnetic Ce^{4+} is the hole trap centre, magnetic resonance methods allow the investigation of the complementary electron trap centres.

The MCDA of a Ce^{3+}-doped fluorozirconate glass showed an intense paramagnetic band peaking at 285 nm, which can be assigned to the Ce^{3+} absorption [111], and a second one between 300 and 550 nm with its maximum at 310 nm having opposite sign.

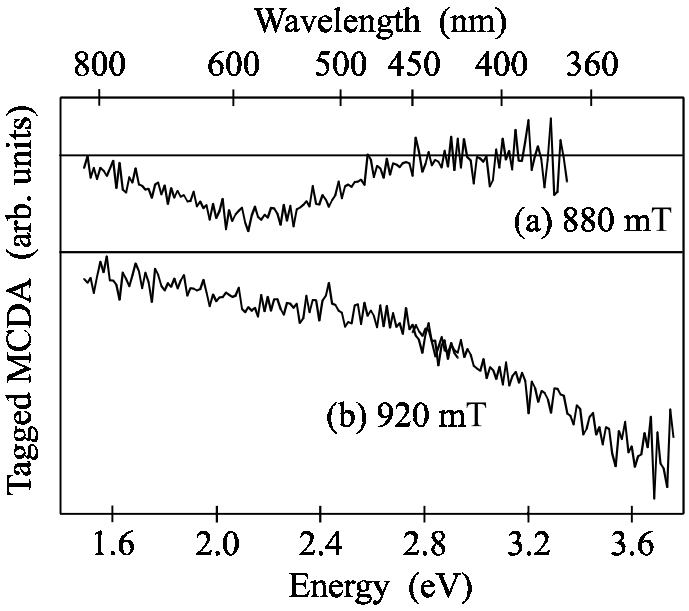

Figure 5.4 "Tagged" MCDA spectra of Ce-doped fluorozirconate glass, detected at (a) 880 mT and (b) 920 mT, recorded after X-irradiation at 1.5 K applying 24 GHz microwave frequency. For the sake of clarity the spectra are vertically displaced [114].

MCDA-detected EPR on the band peaking at 285 nm yielded a single line which can be simulated using the theoretical g tensor $g_{\perp} = 18/7$ and $g_{||} = 6/7$ for the $J = 5/2$ ground state of the $4f^1$ electron of Ce^{3+} [112]. Note, that in a powder or glass sample all angular orientations are represented with equal probability. The effect of this angular averaging can be mathematically simulated, leading to the calculation of "powder pattern". In general, paramagnetic centres in a glass will be characterised by a statistical distribution in the spin Hamiltonian parameters as a consequence of vitreous disorder. This contrasts with powdered crystalline materials where discrete sets of parameters pertain [113].

After X-irradiation at RT the MCDA spectrum showed a new band at approximately 570 nm in addition to an increased paramagnetic signal in the range from 300 to 700 nm which corresponds to the maximum of the stimulation of the PSL [105]. EPR detected in the MCDA at 570 nm (figure 5.3a) yielded a double-structured line with peaks at $g = 1.98 \pm 0.01$ and at $g = 1.91 \pm 0.01$, whereas MCDA-detected EPR at 350 nm (figure 5.3b) showed only a single line at $g = 1.90 \pm 0.01$. The g values of these resonances, being smaller than g_e for the free electron, indicate that electron trap centres have been formed (see e.g., [10]). These lines did not appear before X-irradiation. "Tagged"

MCDA measurements showed that the low field line at $g = 1.98$ (detected at 880 mT) belongs to the new paramagnetic band at 570 nm (figure 5.4a) whereas the high field lines having $g = 1.90$-1.91 (detected at 920 mT) belong to the band between 300 and 700 nm (figure 5.4b). Probably X-irradiation creates two defect centres having different MCDA bands. One centre has a g value of $g = 1.98$ whereas the second one has $g = 1.90$. The double-structured line measured in the MCDA band at 550 nm is thus a superposition of two EPR lines since both show MCDA there.

Summary

The investigation of the information storage and read-out processes in the X-ray storage phosphor BaFBr:Eu^{2+} showed that it is necessary to distinguish between stoichiometric and non-stoichiometric BaFBr. It turned out that the stoichiometric material is always contaminated with oxygen whereas no oxygen contamination was found in the non-stoichiometric one.

For stoichiometric as well as for non-stoichiometric BaFBr, the PSL active electron trap centres are F(Br^-) and F(F^-) centres. In stoichiometric BaFBr, "impurity" sites (e.g. oxygen or the activator) are preferred sites for the radiation-induced electron-hole centre generation. The F centre (electron trap) generation is significantly influenced by the incorporated oxygen impurities which provide the necessary anion vacancies for the F centres. The electron-hole pairs are obviously not created via a F-H process. In spite of thorough research by optically-detected magnetic resonance techniques no H centres ((halogen)$_2^-$ molecules occupying single halide sites) have been observed. The F centre generation seems thus to be impurity-limited. The hole centre taking part in the photostimulated luminescence process is still unknown.

It was shown by magic angle spinning nuclear magnetic resonance that in non-stoichiometric BaFBr, 10% fluorine "antisites" (fluorines on bromine sites) are present. The F centre generation occurs via a F-H process between the F^- and Br^- sublattices whereas no F-H process within one sublattice was observed. This is in agreement with the observations in stoichiometric BaFBr where no H centres have been found either. The existence of fluorine antisites enables the F centre generation. In non-stoichiometric BaFBr it is thus not impurity limited as in stoichiometric BaFBr. This feature is very promising for the use of non-stoichiometric BaFBr as X-ray storage phosphors for very high doses.

The spatial resolution of X-ray storage phosphor screens based on the optically anisotropic BaFBr is limited by the scattering of the read-out light. The scattering can proba-

bly be reduced by using optically isotropic crystal systems instead. The search for such X-ray storage phosphors, which have also comparable figures of merit as Eu^{2+}-doped BaFBr, yielded the alkali halides RbBr:Ga^{+} and CsBr:Ga^{+} as best candidates, as well as CsBr:Eu^{2+}. The elpasolite Cs_2NaYF_6:Ce^{3+} is also very promising whereas KBr:In^{+} and RbI:Tl^{+} are not so interesting for the practical applications.

The information storage and read-out process in RbBr:Ga^{+} and CsBr:Ga^{+} can be explained by a simple pair mechanism: Upon X-irradiation F centres are generated as electron trap centres and Ga^{2+} centres as complementary hole trap centres. Two different types of Ga^{2+} hole trap centres were observed: $(Ga^{2+})^{I}$ and $(Ga^{2+})^{II}$ centres. Type I is an isolated Ga^{2+} on a Rb^{+} or Cs^{+} site, whereas type II is a complex between Ga^{2+} on Rb^{+} or Cs^{+} site and a nearest neighbouring cation vacancy. Only the type I Ga^{2+} centres are taking part in the PSL process. In RbBr:Ga^{+} a sufficient high Ga^{+} concentration suppresses the $(Ga^{2+})^{II}$ generation. In CsBr:Ga^{+} the $(Ga^{2+})^{I}$ centres clearly dominate over the PSL-inactive $(Ga^{2+})^{II}$ centres for all Ga^{+} doping levels.

For practical use, it is advantageous to red-shift the PSL-excitation to the near-infrared in order to use low cost, but high intensity laser diodes as stimulation light sources in the read-out process. BaFBr:Eu^{2+} as well as the two alkali halides RbBr:Ga^{+} and CsBr:Ga^{+} can be co-doped with smaller cations, leading to the formation of perturbed electron trap centres (F_A centres) the absorption bands of which are clearly red-shifted. It turned out that these sites are preferred sites for the electron-hole centre generation. Especially for low X-ray doses the ratio between the perturbed F_A and unperturbed F centres is clearly in favour of the perturbed one. This is in analogy to the red-shift of the PSL excitation in BaFBr:Eu^{2+}: The PSL excitation can be made sensitive to stimulation further into the infrared by additional Ca^{2+} or Sr^{2+} doping. Upon X-irradiation $F_A(Br^{-}$, Ca^{2+} or $Sr^{2+})$ centres are formed preferentially as photostimulable centres electron traps.

The energy storage and read-out processes in the alkali halides KBr:In^{+} and RbI:Tl^{+} and in the elpasolites Cs_2NaYF_6:Ce^{3+} and Cs_2NaYF_6:Pr^{3+} are completely understood assuming a simple pair model of an F centre as electron trap centre and the activator itself as complementary hole trap centre.

The observation that upon X-irradiation the electron and hole trap centres are always created with a spatial correlation to the activator is of particular interest for the functioning of the corresponding materials as storage phosphors. The reason for this spatial correlation is still an open question. A possible explanation for this phenomenon could be a lattice distortion around the activator due to an ionic radius misfit. However, an

electron nuclear double resonance investigation of Eu^{2+} in BaFBr yielded that such a lattice distortion would only be very small (below 2%).

Another approach to reduce the scattering of the read-out would be a phosphor based on a glass. It was shown that a fluorozirconate glass ceramic doped with Eu^{2+} or Ce^{3+} shows a significant PSL effect after X-irradiation at RT. The application of such glass ceramics as X-ray storage phosphors will depend upon optimising the crystallite size and dopant concentration so as to maximise efficiency and minimise scattering. The development of such systems is still at its beginning.

References

[1] M. Sonoda, M. Takano, J. Miyahara, and H. Kato, *Radiology* **148**, 833 (1983)

[2] J.-M. Spaeth, Th. Hangleiter, F.-K. Koschnick, and Th. Pawlik, *Radiat. Eff. Defects Solids* **135**, 499 (1995)

[3] A. R. Lakshmanan, *phys. stat. sol. (a)* **153**, 3 (1996)

[4] H. von Seggern, *Brazilian Journal of Physics* **29**, 254 (1999)

[5] J.-M. Spaeth, *Proceedings ICDIM2000* (Johannesburg-Midrand, South Africa, 2000), to be published in *Radiation Effects and Defects in Solids*

[6] A. Kalnins, I. Plavina, L. Trinkler, and M. Trinkler, *Proceedings LUMDETR'91* (University of Latvia, Riga, 1991), p. E18

[7] M. Thoms, H. von Seggern, A. Winnacker, *J. Appl. Phys.* **76** (3), 1800 (1994)

[8] Th. Hangleiter, U. Rogulis, C. Dietze, J.-M. Spaeth, P. Willems, L. Struye, P. J. R. Leblans, *Proceedings SCINT'95* (Delft University Press, The Netherlands)

[9] Th. Pawlik and J.-M. Spaeth, *Proceedings SCINT'95* (Delft University Press, The Netherlands, 1995), p. 392

[10] J.-M. Spaeth, J. R. Niklas, and B. H. Bartram, *Structural Analysis of Point Defects in Solids*, Springer Series in Solid State Sciences **43** (Springer, Berlin, 1992)

[11] L. F. Mollenauer and S. Pan, *Phys. Rev. B* **6** (3), 772 (1972)

[12] F. Lüty and J. Mort, *Phys. Rev. Letters* **12**, 45 (1964)

[13] C. P. Slichter, *Principles of Magnetic Resonance*, Springer Series in Solid State Sciences **1**, 3rd Edition (Springer, Berlin, 1989)

[14] N. Bloembergen, S. Shapiro, P. S. Pershan, and J. O. Artman, *Phys. Rev.* **114**, 445 (1959)

[15] F.-K. Koschnick, Doctoral Thesis, Paderborn (1991)

[16] H. Seidel, *Z. Phys.* **165**, 239 (1961)

[17] K. W. H. Stevens, *Proc. Phys. Soc.* **65**, 209 (1952)

[18] S. Schweizer and J.-M. Spaeth, *J. Phys. Chem. Solids* **58** (6), 859 (1997)

[19] A. Meijerink, G. Blasse, and L. Struye, *Mater. Chem. Phys.* **21**, 261 (1989)

[20] R. C. Gonzalez and P. Wintz, *Digital Image Processing* (Addison Wesley, Massachusetts, 1977)

[21] P. P. Dendy and B. Heaton, *Physics for Radiologists* (Blackwell Scientific Publications, Oxford, 1987)

[22] P. Willems, *Private Communication* (Agfa-Gevaert, Mortsel, Belgium)

[23] H. von Seggern, T. Voigt, W. Knüpfer, and G. Lange, *J. Appl. Phys.* **64**, 1405 (1988)

[24] M. Thoms, H. von Seggern, A. Winnacker, *Phys. Rev. B* **44**, 9240 (1991)

[25] G. Blasse, *Journal of Alloys and Compounds* **192**, 17-21 (1993)

[26] B. W. Liebich and D. Nicollin, *Acta Cryst.* B**33**, 2790 (1977)

[27] H. P. Beck, *Z. anorg. allg. Chem.* **451**, 73 (1979)

[28] K. Takahashi, J. Miyahara and Y. Shibahara, *J. Electrochem. Soc*. **132**, 1492 (1985)

[29] H. H. Rüter, H. von Seggern, R. Reiniger and V. Saile, *Phys. Rev. Letters* **65**, 2438 (1990)

[30] K. S. Song and R. T. Williams, *Self-trapped Excitons*, Springer Series in Solid State Sciences **105**, 2nd Edition (Springer, Berlin, 1993)

[31] J.-M. Spaeth, W. Meise, and K. S. Song, *J. Phys.: Condens. Matter* **6**, 1801-1814 (1994)

[32] Th. Hangleiter, F.-K. Koschnick, J.-M. Spaeth, R. H. D. Nuttall, and R. S. Eachus, *J. Phys.: Condens. Matter* **2**, 6837 (1990)

[33] Th. Hangleiter, F.-K. Koschnick, J.-M. Spaeth, and R. S. Eachus, *Radiation Effects and Defects in Solids* **119-121**, 615 (1991)

[34] F.-K. Koschnick, Th. Hangleiter, J.-M. Spaeth, and R. S. Eachus, *J. Phys.: Condens. Matter* **4**, 3001 (1992)

[35] R. S. Eachus, F.-K. Koschnick, J.-M. Spaeth, R. H. D. Nuttall and W. G. McDugle, *Proceedings Intern. Conf. on Defects in Insulating Materials*, Nordkirchen, Germany, ed. O. Kanert and J.-M. Spaeth, World Scientific (Singapore) p. 267

[36] R. S. Eachus, R. H. D. Nuttall, W. G. McDugle, F.-K. Koschnick and J.-M. Spaeth, *Proceedings Intern. Conf. on Defects in Insulating Materials*, Nordkirchen, Germany, ed. O. Kanert and J.-M. Spaeth, World Scientific (Singapore) p. 1172

[37] R. S. Eachus, W. G. McDugle, R. H. D. Nuttall, M. T. Olm, F.-K. Koschnick, Th. Hangleiter, and J.-M. Spaeth, *J. Phys.: Condens. Matter* **3**, 9327 and 9339 (1991)

[38] R. S. Eachus, R. H. D. Nuttall, M. T. Olm, W. G. McDugle, F.-K. Koschnick, Th. Hangleiter, and J.-M. Spaeth, *Phys. Rev. B* 52, 3941 (1995)

[39] S. Schweizer and J.-M. Spaeth, *J. Phys.: Condens. Matter* **11**, 1723 (1999)

[40] F.-K. Koschnick, J.-M. Spaeth, R. S. Eachus, W. G. McDugle and R. H. D. Nuttall, *Phys. Rev. Letters* **67**, 3571 (1991)

[41] R. U. Bauer, J. R. Niklas and J.-M. Spaeth, *phys. stat. sol. (b)* **118**, 557 (1983)

[42] K. Takahashi, K. Kohda, J. Miyahara, Y. Kanemitsu, K. Amitani, S. Shionoya, *J. Luminescence* **31 & 32**, 266 (1984)

[43] Y. Iwabuchi, C. Umemoto, K. Takahashi, and S. Shionoya, *Journal of Luminescence* **48 & 49**, 481 (1991)

[44] A. Meijerink and G. Blasse, *J. Phys. D* **24**, 626 (1991)

[45] D. M. De Leeuw, T. Kovats and S. P. Herko, *J. Electrochem. Soc*. **134**, 491 (1987)

[46] F.-K. Koschnick, J.-M. Spaeth, and R. S. Eachus, *J. Phys.: Condens. Matter* **4**, 8919 (1992)

[47] Y. Kondo, T. Tezuka, and Y. Iwabuchi, *Proceedings ICDIM2000* (Johannesburg-Midrand, South Africa, 2000), to be published in *Radiation Effects and Defects in Solids*

[48] R. J. Klee, *J. Phys. D: Appl. Phys*. **28**, 2529 (1995)

[49] F. K. Koschnick, T. Hangleiter, K. S. Song, and J.-M. Spaeth, *J. Phys.: Condens. Matter* **7**, 6925 (1995)

[50] E. Radzhabov and V. Otroshok, *J. Phys. Chem. Solids* **56**, 1 (1995)

[51] C. Dietze, Th. Hangleiter, P. Willems, R. J. R. Leblans, L. Struye, and J.-M. Spaeth, *J. Appl. Phys.* **80**, 1074 (1996)

[52] S. Schweizer, J.-M. Spaeth and T. J. Bastow, *J. Phys.: Condens. Matter* **10**, 9111 (1998)

[53] M. H. Cohen and F. Reif*, Solid State Physics* **5**, 321 (1957)

[54] N. Boden, P. K. Kahal, A. Mee, M. Mortimer, and G. N. Peterson, *Journal of Magnetic Resonance* **54**, 419 (1983)

[55] R. W. Vaughan, D. D. Elleman, W.-K. Rhim, and L. M. Stacey, *Journal of Chem. Phys.* **57**, 5383 (1972)

[56] F.-K. Koschnick, J.-M. Spaeth, and R. S. Eachus, *J. Phys.: Condens. Matter* **4**, 3015 (1992)

[57] W. Hayes, *Crystals with the fluoride structure* (Clarendon, Oxford, 1974)

[58] R. C. Baetzold, *J. Chem. Phys. Solids* **50**, 915 (1989)

[59] R. C. Baetzold, *Phys. Rev. B* **36**, 9182 (1987)

[60] W. Meise, U. Rogulis, F.-K. Koschnick, K. S. Song, and J.-M. Spaeth, *J. Phys.: Condens. Matter* **6**, 1815 (1994)

[61] S. Schweizer, P. Willems, P. J. R. Leblans, L. Struye, J.-M. Spaeth, *J. Appl. Phys.* **79**, 4157 (1996)

[62] *Physics of Color Centres*, edited by W. B. Fowler (Academic Press, New York and London, 1968)

[63] D. Nicollin and H. Bill, *J. Phys. C* **11**, 4803 (1978)

[64] S. Assmann, S. Schweizer, and J.-M. Spaeth, *phys. stat. sol. (b)* **212**, 325 (1999)

[65] H. von Seggern, A. Meijerink, T. Voigt, and A. Winnacker, *J. Appl. Phys.* **66**, 4418 (1989)

[66] P. F. Braslavets, A. Kalnins, I. Plavina, A. I. Popov, B. I. Rapoport, A. Tale, *phys. stat. sol. (b)* **170**, 395 (1992)

[67] F. J. Ahlers, F. Lohse, Th. Hangleiter, J.-M. Spaeth, and R. H. Bartram, *J. Phys. C: Solid State Phys.* **17**, 4877 (1984)

[68] U. Rogulis, I. Tale, Th. Hangleiter, and J.-M. Spaeth, *J. Phys.: Condens. Matter* **7**, 3129 (1995)

[69] A. Fukuda, *Phys. Rev. B* **1**, 4161 (1970)

[70] I. Plavina, I. Tale, and A. Tale, *Proceedings LUMDETR'91* (University of Latvia, Riga, 1991), p. D4

[71] L. E. Trinkler, M. F. Trinkler and A. I. Popov, *phys. stat. sol. (b)* **180**, K31 (1993)

[72] A. Kalnins, I. Plavina, and A. Tale, *Nuclear Instruments and Methods in Physics Research B* **84**, 95-101 (1994)

[73] C. J. Delbecq, W. Hayes, and P. H. Yuster, *Phys. Rev. B* **121**, 1043 (1961)

[74] U. Rogulis, K. S. Song, and J.-M. Spaeth, *J. Phys.: Condens. Matter* **7**, 7699 (1995)

[75] B. J. Faraday and W. D. Compton, *Phys. Rev. A* **138**, 893 (1965)

[76] U. Rogulis, C. Dietze, Th. Pawlik, Th. Hangleiter, and J.-M. Spaeth, *J. Appl. Phys.* **80**, 2430 (1996)

[77] D. Schoemaker, *Phys. Rev. B* **7**, 786 (1973)

[78] U. Rogulis, J.-M. Spaeth, I. Cabria, M. Moreno, I. A. Aramburu, and M. T. Barriuso, *J. Phys.: Conden. Matter* **10**, 6473 (1998)

[79] I. Cabria, M. Moreno, I. A. Aramburu, M. T. Barriuso, U. Rogulis, and J.-M. Spaeth, *J. Phys.: Conden. Matter* **10**, 6481 (1998)

[80] U. Rogulis, S. Schweizer, S. Assmann, and J.-M. Spaeth, *J. Appl. Phys.* **84**, 4537 (1998)

[81] U. Rogulis, S. Schweizer, S. Assmann, and J.-M. Spaeth, *J. Appl. Phys.* **87**, 207 (2000)

[82] C. Dietze, Diploma Thesis, Paderborn (1995)

[83] Yu. V. Kolk and A. Ch. Lushchik, *Sov. Phys. Solid State* **28**, 805 (1986)

[84] J. J. Pilloud and C. Jaccard, *phys. stat. sol. (b)* **92**, 233 (1979)

[85] F.-K. Koschnick, K.-H. Wietzke, and J.-M. Spaeth, *Phys. Rev. B* **58** (12), 7707 (1998)

[86] P. G. Baranov and V. A. Khramtsov, *Sov. Phys. Solid State* **20**, 1080 (1978)

[87] C. J. Delbecq, R. Hartford, D. Schoemaker, and P. H. Yuster, *Phys. Rev. B* **31**, 3631 (1976)

[88] F. van Steen and D. Schoemaker, *Phys. Rev. B* **19**, 55 (1979)

[89] E. Goovaerts, J. Andriessen, S. V. Nistor, and D. Schoemaker, *Phys. Rev. B* **24**, 29 (1981)

[90] D. K. Rowell and M. J. L. Sangster, *J. Phys. C: Solid State Phys.* **14**, 2909-2921 (1981)

[91] F. J. Ahlers, Doctoral Thesis, Paderborn (1985)

[92] S. Assmann, Doctoral Thesis, Paderborn (2000)

[93] S. Radhakrishna, N. N. Nigam and V. S. Sivasankar, *Phys. Rev. B* **15**, 1187 (1977)

[94] V. P. Savelev, V. P. Avdonin, L. D. Dugarova, A. P. Nadashkovskii, and B. T. Plachenov, *Soviet Physics Solid State* **16**, 700 (1974)

[95] C. P. Medrano, H. S. Murrieta, and J. O. Rubio, *Journal of Luminescence* **29**, 223 (1984)

[96] E. P. Munoz, J. O. Rubio, H. S. Murrieta, G. S. Aguilar, and J. O. Boldu, *J. Chem. Phys.* **62**, 3416 (1975)

[97] D. Babel, *Mater. Res. Bull.* **8**, 1371 (1973)

[98] Th. Pawlik and J.-M. Spaeth, *J. Appl. Phys.* **82** (9), 4236 (1997)

[99] Th. Pawlik, Doctoral Thesis, Paderborn (1996)

[100] Th. Pawlik and J.-M. Spaeth, *Material Science Forum* **239-241**, 287 (1997)

[101] Th. Pawlik and J.-M. Spaeth, *phys. stat. sol. (b)* **203**, 43 (1997)

[102] J. Qiu, Y. Shimizugawa, Y. Iwabuchi, and K. Hirao, *Appl. Phys. Lett.* **71,** 759 (1997)

[103] J. Qiu, Y. Shimizugawa, Y. Iwabuchi, and K. Hirao, *Appl. Phys.* **71**, 43 (1997)

[104] J. Qiu, Y. Shimizugawa, N Sugimoto, and K. Hirao, *J. Non-Cryst. Solids* **222**, 290-295 (1997)

[105] A. Edgar, J.-M. Spaeth, S. Schweizer, S. Assmann, P. J. Newman, and D. R. MacFarlane, *Appl. Phys. Lett.* **75**, 2386 (1999)

[106] S. Schweizer, S. Assmann, A. Edgar, and J.-M. Spaeth, *Nuclear Instruments and Methods in Physics Research B* **166-167**, 508-510 (2000)

[107] Joint Committee on Powder Diffraction Standards, (Swarthmore, USA, 1996), Powder Diffraction File entry #45-1314

[108] G. Liu and H. A. Eick, *Journal of Less Common Metals* **149**, 47 (1989)

[109] D. R. MacFarlane, P. J. Newman, J. D. Cashion, and A. Edgar, *J. Non-Cryst. Solids* **257**, 53-58 (1999)

[110] N. Iwase, S. Tadaki, S. Hidaka and N. Koshino, *Journal of Luminescence* **60 & 61**, 618 (1994)

[111] G. M. Williams, T.-E. Tsai, C. I. Merzbacher, and E. J. Friebele, *Journal of Lightwave Technology* **15**, 1357 (1997)

[112] A. Abragam and B. Bleaney, *Electron Paramagnetic Resonance of Transition Ions* (Dover Publications, New York, 1986)

[113] D. L. Griscom, *J. Non-Cryst. Solids* **40**, 211-272 (1980)

[114] S. Schweizer, S. Assmann, A. Edgar, and J.-M. Spaeth, *Nuclear Instruments and Methods in Physics Research B* **166-167**, 505-507 (2000)

Mein Dank geht an erster Stelle an Herrn Prof. Dr. J.-M. Spaeth, der mich in allen Phasen meiner wissenschaftlichen Laufbahn stets unterstützt und gefördert hat. Er hat mir mit zahlreichen Diskussionen und persönlichen Gesprächen ganz wesentlich bei der Anfertigung dieser Arbeit geholfen.

Im weiteren möchte ich mich bei Herrn Dr. S. Assmann und Herrn Dr. U. Rogulis für die ausgezeichnete Zusammenarbeit bedanken.

Für die problemlose Versorgung mit flüssigem Helium danke ich Herrn Dr. F. Lohse und Herrn J. Pauli. Weiterhin möchte ich mich bei den Kollegen des Kristallzuchtlabors Herrn Dr. Th. Hangleiter, Herrn D. Niggemeier und Herrn R. Winterberg bedanken.

Allen namentlich nicht erwähnten Mitgliedern der Arbeitsgruppe danke ich für die angenehme Arbeitsatmosphäre.